An equation-free approach for heterogeneous networks

Sidra Zafar

School of Mathematical and Computational Sciences
Massey University

This dissertation is submitted for the degree of
Doctor of Philosophy

September 2023

I would like to dedicate this thesis to my sweet little girl, Bareerah Fatima.

Acknowledgements

First and foremost, I want to thank Almighty Allah for providing me with the strength and determination to accomplish my research.

A very special thanks to my co-supervisor, Dr. Alona Ben Tal, for her selfless and consistent dedication to my intellectual and professional development, for her suggestions and the constant encouragement she gave me during my time at Massey University, and for believing in me even (and especially) when I didn't seem to believe in myself.

I would also like to thank my main supervisor Distinguished Professor Robert Mclachlan and my other co-supervisor, Dr. David Simpson for their continuous support, expert feedback on this thesis and for giving me the flexibility to work on my own way.

I am grateful to the School of Mathematical and Computational Sciences, Massey University, New Zealand for providing me with a scholarship during my PhD. The generous support has greatly helped me to advance my work.

I appreciate Dr. Carlo Laing's support during the first two years of my PhD.

I would also like to thank my parents, especially my mother, who taught me the importance of education and encouraged me every step of the way to pursue my dream of getting higher education from overseas.

I am very thankful to my my mother-in-law and father-in-law, for taking care of my daughter while I was away from her during my PhD.

Last, but not least, I would like to thanks my children, Bareerah Fatima and Muhammad Affan Raees, for their endless love and joy, as well as my husband, Muhammad Saad, whose dedication, affection and confidence in me, has lifted a burden off my shoulder. Together, we have accomplished it!

Abstract

Oscillators exist in many biological, chemical and physical systems. Often when oscillators with different periods of oscillations are coupled, they synchronize and oscillate with the same period. Examples include groups of synchronously flashing fire-flies or chirping crickets. There are two questions of interest in this work. (1) Under what conditions will a system of coupled oscillators synchronize? and (2) Can a large system of synchronized oscillators be represented by a smaller number of variables? We study these questions for Kuramoto like models which are coupled in different ways. Examples include spatially extended and all-all coupling. We study conditions under which synchronization occurs in small and large networks by varying the coupling strength, calculating stabilities of synchronized solutions and creating bifurcation diagrams of the steady state solution as a function of coupling strength in one and two-dimensions. We use an equation free approach to approximate the coarse scale behaviour of a large coupled network, for which the equations are known, by a low dimensional description of variables, for which no governing equations are available in closed form. Our results show that a small number of variables can reproduce the behaviour of the stable solutions in the full systems. However, the equation-free approach did not work as well for the unstable solutions. Possible reasons for this are explored in the thesis.

Contents

List of Figures

List of Tables

Chapter 1

Introduction

Synchronization is a natural phenomenon that can be observed widely in nature. Examples include the rhythmic clapping of human audiences, the flashing of fireflies, the chirping of crickets, and the coordinated movements of motor neurons in the human body [7, 49, 1]. Mathematical models that capture synchronization can be traced back to 1967, when Winfree proposed a mathematical model for a network of globally coupled oscillators [62]. Inspired by Winfree's model, a much simpler and solvable model was introduced by Kuramoto [31, 30]. Kuramoto's remarkable model has inspired a wide spectrum of research, and various modifications have been developed and applied to a variety of fields such as neuro-science [13], power systems [14, 21], chemical engineering [30, 29], geophysics [58], and physics [56, 2, 16, 15]. This thesis contributes to the study of Kuramoto-based networks with a focus on simplifying them using the equation-free approach. We first review briefly the Kuramoto model and some of the research that grew out of it. We then review the relevant literature on the equation-free approach and its previous application to Kuramoto-based networks.

1.1 Kuramoto model

Consider a population of N oscillators, each having a phase θ_i and an angular frequency ω_i. Thus, for uncoupled oscillators, the rate of change of the phase is defined as $\dot{\theta}_i = \omega_i,\ (i = 1,\ldots,N)$. The interaction between the oscillators was included by Kuramoto as a sinusoidal function of the phase differences with a coupling strength, K, leading to the following equations:

$$\dot{\theta}_i = \omega_i + \frac{K}{N}\sum_{j=1}^{N}\sin(\theta_j - \theta_i), \qquad i = 1,\ldots,N \tag{1.1}$$

This model demonstrates that coupled oscillators can synchronize when the coupling strength is larger than a critical value. The original Kuramoto model was studied for the globally coupled, equally weighted oscillators. Since the development of the first globally connected Kuramoto model, numerous studies have been conducted. Several methodologies for addressing phase/frequency synchronization, partial synchronization, phase balancing, as well as the inclusion of noise and inertia in the Kuramoto model have all been addressed using a variety of analytical and numerical techniques. [1, 15, 45, 10, 11, 25, 18, 48].

In parallel with the studies on the traditional Kuramoto model, one has witnessed the emergence of an overwhelming number of works focused on effects caused by the introduction of heterogeneous connection patterns, letting the interactions to be no longer only restricted to global coupling. This generalization of the Kuramoto model in complex networks is obtained by including the connectivity in the coupling term as [2, 4].

$$\dot{\theta}_i = \omega_i + K \sum_{j=1}^{N} A_{ij} \sin(\theta_j - \theta_i) \quad i = 1, \ldots, N \tag{1.2}$$

where A_{ij} is the adjacency matrix with its elements distributed such as $A_{ij} = 1$ if there is a connection between nodes i and j otherwise $A_{ij} = 0$.

After that, most of the attention has been aimed at determining how network structure influences the onset of synchronization. Initial studies combined the small world networks with the Kuramoto model [60, 24, 42, 37]. The synchronization phenomenon for a Kuramoto model has been observed on the finite-size scaling network [12, 23] and on scale-free networks, highlighting the role played by highly connected nodes (hubs) in the synchronization phenomenon [36].

1.2 Spatially extended Kuramoto network

Studying the Kuramoto model with various complex networks that have different network architectures demonstrates the importance of coupling topologies in studying the synchronization of coupled oscillators. Hence, coupling range becomes one of the main characteristics in analyzing different kinds of complex Kuramoto networks. The cases in which oscillators interact only with their close neighbors are known as local coupling [28], whereas the case in which each oscillator interacts with all the others is known as all-all coupling or global coupling. It should be noted that in the case of an all-all network, the coupling topology loses its meaning as all the oscillators are driven by the same mean field from all the oscillators. This fact makes it simpler, and thus many analytical methods have been proposed for studying its collective properties [46, 59, 49, 3]. However, in the case of non-locally coupled oscillators, many numerical techniques can be applied, and one kind of solution that has been observed is the so-called chimera state in which some oscillators synchronize while others do not [33, 47]. Another type of solution in nonlocally coupled oscillators are traveling waves. These are defined by a fixed profile and move with a constant speed. These traveling waves are studied for many neural systems [17, 27, 50, 51]. One specific type of traveling wave is the uniformly twisted wave for which the state of the oscillators changes linearly with the spatial position. One type of non-locally coupled Kuramoto model for which uniformly twisted states (details are discussed in section 2.5) appear is referred to as the spatially extended Kuramoto model.

Consider oscillators θ_i, moving with their individual angular frequencies ω_i and coupled to their M nearest neighbors on both sides [34]:

$$\dot{\theta}_i = \omega_i + \frac{K}{2M+1} \sum_{j=-M}^{M} \sin(\theta_{i+j} - \theta_i), \quad i = 1, \ldots, N \tag{1.3}$$

Here, N is the number of oscillators, K is the coupling strength, and periodic boundary conditions for index i are taken. Periodic boundary conditions in the given model of oscillators mean that the system forms a ring where each oscillator is coupled to its M nearest neighbors on both sides, treating the first and last oscillators as neighbors. This circular arrangement enables the emergence of stable synchronous states and uniformly twisted traveling waves, known as q-twisted states, characterized by constant phase shifts between neighboring oscillators, resulting in spatially linear patterns. The dynamics of such a model depend on the number of oscillators N and the coupling range M. The given system Eq. (1.3) always has a stable synchronous state, $\theta_i = \omega_i t + C$. However, as the coupling range varies, new states emerge in the form of uniformly twisted traveling waves $\theta_i = \omega_i t + \frac{2\pi q i}{N} + C, i = 1, ..., N$, where $\frac{2\pi q}{N}$ is the phase difference between the oscillators. These so-called q-twisted states (characterized by an integer q) are simple traveling waves with constant phase shifts between neighboring oscillators, resulting in spatially linear patterns.

Such models have been studied previously, and analysis of the twisted states has been performed. For example, in the case of identical oscillators, [61] discovered that many twisted states exist for such types of networks, and the basins of attraction follow a Gaussian distribution in relation to a winding number q. Later, this idea has been extended to a heterogeneous unimodal frequency distribution network, and partially coherent twisted states have been observed [44]. Thus, these partially coherent twisted states are defined by the expression of a spatially dependent, complex order parameter whose argument differs from $2\pi q$ across the ring. The research conducted by [44] considered the Lorentzian frequency distribution for non-local coupling phase oscillators, and the stability of the resulting partially coherent twisted states was theoretically studied using the Ott-Antonsen or (OA) approach [46]. The Ott-Antonsen ansatz provides a powerful method to simplify the analysis by projecting the dynamics of the coupled oscillator system onto a lower-dimensional manifold. Laing (2016) also discussed the same model for heterogeneous networks but included different forms of delays in their coupling. Again, the OA approach is used to derive evolution equations for a spatially-dependent order parameter. More recent work is carried out by [63] where two different frequency distributions are considered, and the stability analysis of two different types of twisted waves is done by reducing the model to a continuum limit using the OA approach.

1.3 Equation-free approach and its application to the Kuramoto model

For decades, reducing high-dimensional models to lower dimensions has been a prominent research direction for understanding and analyzing the complicated dynamics of larger and complex networks. Many strategies for reducing different models have been used in the past, such as the perturbation technique [43], and, more recently, the data-driven reduction technique [54]. A recently developed technique, known as an equation-free approach [26, 19], was used to approximate the macroscopic behavior of a detailed system for which the equations are known, by a low-dimensional description of variables for which no governing equations are available in closed form. This can be accomplished by performing short bursts of appropriately designed computational experiments with the detailed, "fine-scale" network dynamic evolution model to obtain the numerical information of the appropriate coarse observables. Since the macroscopic variables change across a much longer time scale compared to the fine-scale variables, the separation of time scales should be considered when choosing coarse variables. The transitions between the microscopic and the macroscopic scales depend on two operators: the restriction and lifting operators. The restriction operator (many-one relation), in general, maps the detailed description of the system to the coarse-grained level, whereas the lifting operator (one-many relation) maps from the coarse-grained to the detailed system. Equation-free methods have been successfully implemented on various problems, including molecular dynamics [9], collective animal behavior dynamics [41], cell population [8], dynamical models on static networks [52], as well as several specific network models [57, 20]. However, this technique mainly depends on (a) identifying and defining a suitable set of coarse variables for which a closed, reduced description of network evolution can theoretically be obtained, and (b) the ability to switch back and forth between the two levels of system description—the "fine" and the "coarse-grained" levels. Thus, one of the important tasks in coarse-graining with this approach is selecting appropriate coarse observables. Diffusion maps [55] and the polynomial chaos expansion [35] have been used for finding these coarse observables.

The equation-free approach with polynomial expansion has also been used to reduce the Kuramoto model to lower dimensions [40, 41]. Moon et al. investigated an original Kuramoto model (all-all coupling) consisting of a finite population of nonidentical coupled oscillators. The coarse-grained variables were defined by realizing the correlation between the phase angle and natural frequencies, where both are considered as random variables. The phase angle is then expanded in terms of the Hermite polynomials of the heterogeneous frequencies with the expansion coefficients selected as coarse variables. Later, this work was extended where the coarse-graining approach was implemented on the Kuramoto model with some network structure (spectral graphs) [52]. More recently, Bertlan (2017) used the polynomial expansion method for coarse-graining the Kuramoto model and described the state of oscillators as a function of both heterogeneous parameters (frequencies and connectivity).

1.4 Discussion and Conclusions

Synchronization has been studied in a wide range of Kuramoto-based networks. In this thesis, we investigate two types of networks, namely the all-all and the spatially-extended network, and observe the transition between them. Unlike many previous studies, our focus is on the simplification of the networks using the equation-free approach. Although some studies have used the equation-free approach, our study is unique in the sense that the equation-free approach has not been used for this specific Kuramoto model (spatially extended network) previously, which we considered.

As mentioned in section 1.2, the spatially extended Kuramoto model has been studied in the past, but to represent the system in lower dimensions, the Ott ansatz [46] was used. The technique of using polynomial expansion for an equation-free approach on the all-all Kuramoto model has also been studied in [40, 41], where the state of the oscillators is expressed as a function of only one of its heterogeneous parameters, i.e., frequencies. In one study, Bertalan (2017) expressed the state of the oscillator in terms of two heterogeneous parameters: intrinsic frequencies and the degree of connectivity. However, our idea is to express the state of oscillators as a function of two of its heterogeneous parameters: frequency and position. For the quickest convergence of the expansion, although we initially used shifted Legendre polynomials, later we use different types of expansions in our study (Details are discussed in Chapter 3 and Chapter 4).

The outline of this thesis is as follows: In Chapter 2, we provide a preliminary analysis of the Kuramoto model, which we will use as a benchmark in the later chapters. In Chapter 3, we formally introduce the equation-free framework and demonstrate it with coarse-projective integration. In Chapter 4, we use the equation-free approach in one dimension (when θ is a function of i and ω only) to generate bifurcation diagrams. Finally, in Chapter 5, we improve the results calculated in Chapter 4 by using the equation-free approach in two dimensions (when θ is a function of both ω and i), and in Chapter 6, we present the conclusions.

Chapter 2

Preliminary Analysis of the Kuramoto Model

In this chapter, we analyze the all-all Kuramoto model in which each oscillator is connected with every other oscillator and the spatially extended Kuramoto model in which each oscillator is connected to its neighbouring oscillators. We first show that when the coupling range, M, is large enough, the spatially extended network is the same as the all-all network. We then discuss two different methods to calculate the stationary states. Lastly, we use the numerical continuation technique to create bifurcation diagrams when the coupling strength, K, varies.

2.1 From spatially extended network to all-all Kuramoto model

Our model of **all-all Kuramoto model** is defined as

$$\dot{\theta}_i = \omega_i + \frac{K}{N-1}\sum_{j=1}^{N}\sin(\theta_j - \theta_i), \qquad i = 1,\dots,N \tag{2.1}$$

Here, θ_i and ω_i are the phase and natural angular velocity of oscillator i respectively, N is the number of oscillators, and $K \geq 0$ is the coupling strength. We divide K by $(N-1)$, rather than by N, as has been done, for example, in [1, 56]. This is because when $i = j$, $\sin(\theta_j - \theta_i) = 0$, hence, we divide the coupling strength by the number of actual connections. As we will illustrate later in the section, this small modification enables us to show that the all-all network is a special case of the spatially extended network.

We define the **spatially-extended Kuramoto model** as:

$$\dot{\theta}_i = \omega_i + \frac{K}{2M} \sum_{j=-M}^{j=M} \sin(\theta_{i+j} - \theta_i), \qquad i = 1, \ldots, N \tag{2.2}$$

Here again, N represents the number of oscillators, θ_i is the phase of oscillator i, $K \geq 0$ is the coupling strength, M is the coupling range and ω_i is the natural frequency drawn from a uniform distribution. In contrast to the previous system (all-all Kuramoto model) where each oscillator was connected to every other oscillator, here, each oscillators is connected to $2M$ other oscillators. When M is large enough the spatially extended network becomes an all-all.

As an example, consider a spatially extended network of $N = 6$ oscillators. When $M = 1$ each oscillator is connected to its very next neighbour on each side, see Figure 2.1(a). When $M = 2$ each oscillator is connected to its two closest neighbours, see Figure 2.1(b). However, once the value of the coupling range M gets higher than half of the total number of oscillators, (in this case, it is $M = 3$), the model becomes all-all Kuramoto model, as shown in Figure 2.1(c). Therefore, for a spatially extended network, if $M > \left(\frac{N}{2} - 1\right)$, then we consider it as all-all Kuramoto model with the edges counted not more than once.

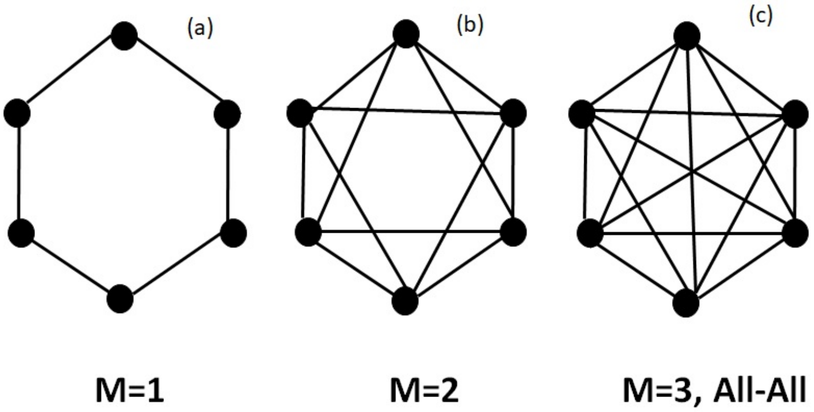

Figure 2.1 From spatially extended to all-all network (a) Each oscillator is connected to its closest neighbour. (b) Each oscillator is connected to its two closest neighbours. (c) Each oscillator is connected to all other oscillators. This example shows $N = 6$ oscillators.

2.2 Calculating the stationary solutions

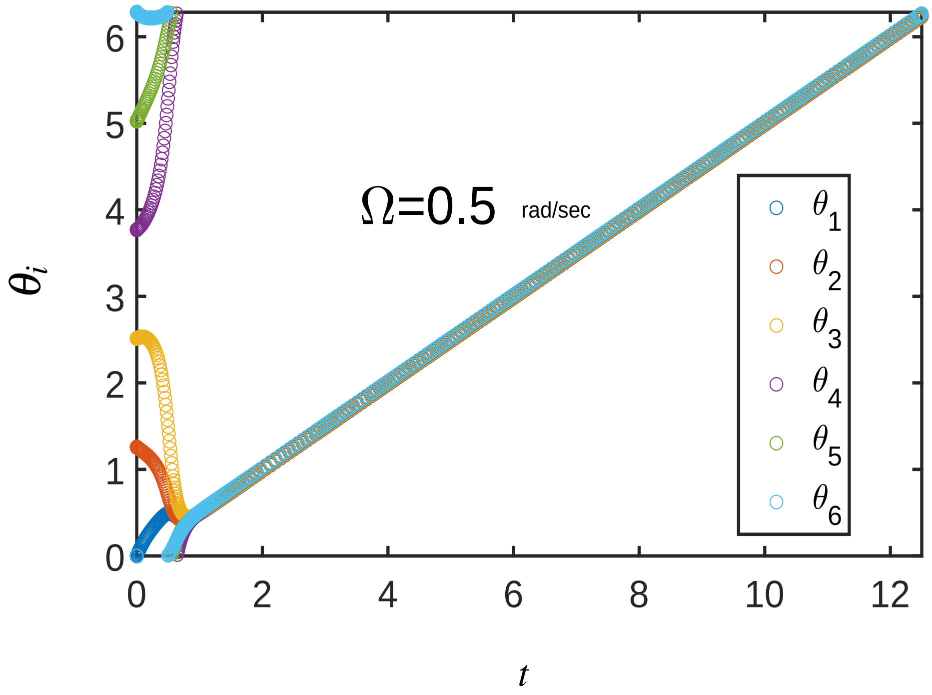

Figure 2.2 State of oscillators for a spatially extended Kuramoto network in a stationary frame for $N = 6$ oscillators with coupling range $M = 2$.

Figure 2.2 shows a solution of a spatially extended Kuramoto network with $N = 6$ and $M = 2$. As can be seen, the oscillators θ_i change with time. In order to calculate the periodic steady state, we use two methods to make our system stationary. In the first method, we make our system stationary by replacing the stationary frame with a rotating frame. In the second method, we consider the relative positions between the oscillators. The two methods are implemented with our own software and the results are then verified with CLMATCONT-L (an advanced Matlab package used for studying the dynamical systems and their bifurcation of large-scale problems).

Method-1 (Analyzing spatially extended network in a rotating frame.)

We demonstrate this method on a network of six oscillators. We solve Eq. (2.2) with $M = 2$ and natural angular velocity uniform randomly distributed in the interval $[0, 1]$. We initially placed all of the oscillators within an interval $[0, 2\pi]$ distributed randomly. Then, using the ode45 subroutine in MATLAB, we solve the system of equations, as shown in Figure 2.2.

Figure 2.2 shows the state of each oscillator as it changes with respect to time. We can see that after a short transition time, all the oscillators start moving with the same angular speed Ω. To make our system stationary, we subtract Ω from our system of equations, $(\dot{\Theta}_i = \dot{\theta}_i - \Omega)$. This creates a new set of phases, Θ_i on the rotating frame. Our modified model of a spatially extended network then becomes

$$\dot{\Theta}_i = \omega_i + \frac{K}{2M} \sum_{j=-M}^{j=M} \sin(\theta_{i+j} - \theta_i) - \Omega, \qquad i = 1, \ldots N \tag{2.3}$$

Because we have a degree of freedom, we may choose where to attach the rotating frame. Here, "degree of freedom" refers to the flexibility to choose the reference frame for the system. In the modified model (Eq. (2.3)), a rotating frame is introduced by subtracting the common angular speed Ω from each oscillator's phase, and the choice to attach this frame at $\Theta_1 = 0$ establishes a consistent phase reference for the oscillators. The simulations of Eq. (2.3) is shown below in Figure 2.3.

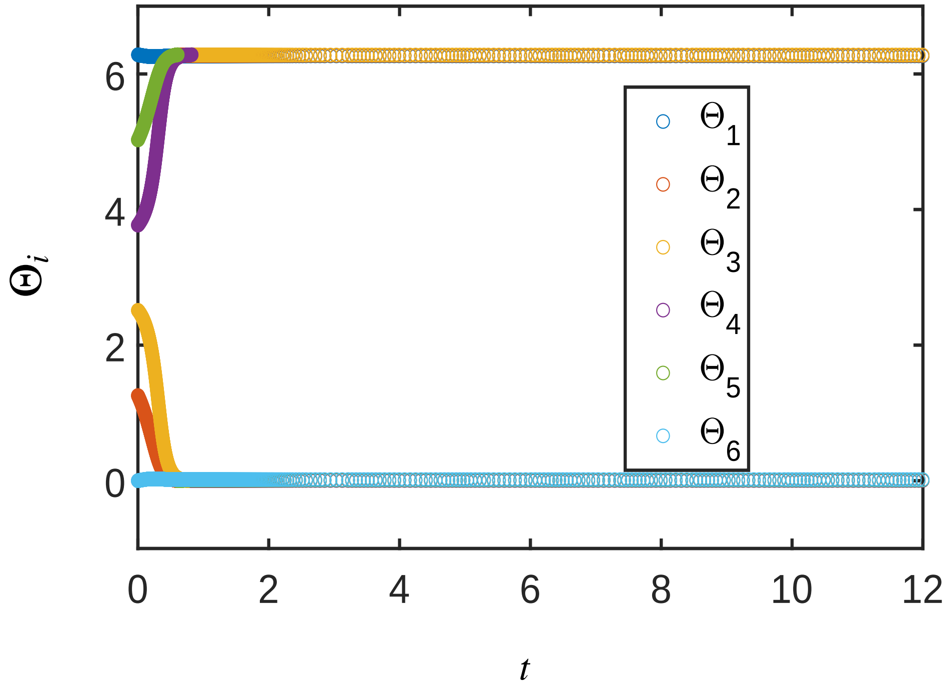

Figure 2.3 State of oscillators with respect to time for spatially extended Kuramoto network in a rotating frame for $N = 6$ and $M = 2$.

Each coloured symbol in Figure 2.3 indicates the state of one of the oscillators in the rotating frame. As oscillators are arranged in a ring, the two lines generated at 0 and 2π are considered to be one. We can observe in Figure 2.3 that in a rotating frame, all the oscillators reached a steady state.

One of the interesting results of our computation is the rate at which the pattern drifts. For both our networks, we can show that the speed of the oscillators Ω is identical to the average frequency of the oscillators. This is proved here for any generalized case.

2.2.1 *Theorem :* "*"Synchronization in spatially extended and all-all Kuramoto networks: The equalization of angular velocities"*

For the spatially extended and all-all Kuramoto networks, the synchronized angular velocity of the oscillators is equal to the average frequency of the oscillators.

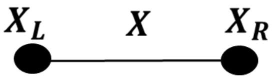

Figure 2.4 A general description of a connection within a network. Connection X is shown between two nodes X_L and X_R.

Proof. X represents the connection that links the two nodes, which we have identified as the left node, X_L, and the right node, X_R, shown in Figure 2.4. Each of the nodes X_L and X_R will have a differential equation associated with it in the form of Eq. (2.1) and Eq. (2.2) that includes the terms

$$Node\ X_L : \sin(X_L - X_R) \tag{2.4}$$

$$Node\ X_R : \sin(X_R - X_L) \tag{2.5}$$

Since $\sin(-\theta) = -\sin(\theta)$, Eq. (2.5) can be written as:

$$\sin(X_R - X_L) = -\sin(X_L - X_R) \tag{2.6}$$

This will be true for all the connections in the network. Hence, after summing up, all the differential equations involving all the sine terms cancel each other, resulting in:

$$\dot{\Theta}_1 + \dot{\Theta}_2 + \dot{\Theta}_3 + \ldots + \dot{\Theta}_N = (\omega_1 + \omega_2 + \omega_3 + \ldots + \omega_N) - N\Omega \tag{2.7}$$

In a steady state,

$$\dot{\Theta}_i = 0 \quad i = 1, \ldots N \tag{2.8}$$

which implies,

$$\Omega = \frac{\sum_{i=1}^{N} \omega_i}{N}. \tag{2.9}$$

Thus, in a steady state of spatially extended and all-all Kuramoto networks, the synchronized speed with which all the oscillators rotate is the same as the average natural velocities of all the oscillators. □

Method-2 (relative distances in the spatially extended network.)

For our rotating pattern shown in Figure 2.2, we can observe that the distance between the oscillators remains constant because they move at the same speed. Therefore, in this method, instead of looking at the rotating frame, we look at the relative distances between two oscillators.

Let x_i denote the relative distance between each oscillator and θ_1

$$x_i = \theta_{i+1} - \theta_1 \qquad i = 1, ..., N-1 \tag{2.10}$$

The differential equations then become:

$$\dot{x}_i = \dot{\theta}_{i+1} - \dot{\theta}_1 \qquad i = 1, \dots, N-1 \tag{2.11}$$

Solving Eq. (2.11), we obtain Figure 2.5, which illustrates the stationary state of the Kuramoto Model spatially extended network. In this case, $M = 2$, $N = 6$, and the angular velocities are uniformly distributed between $[0, 1]$.

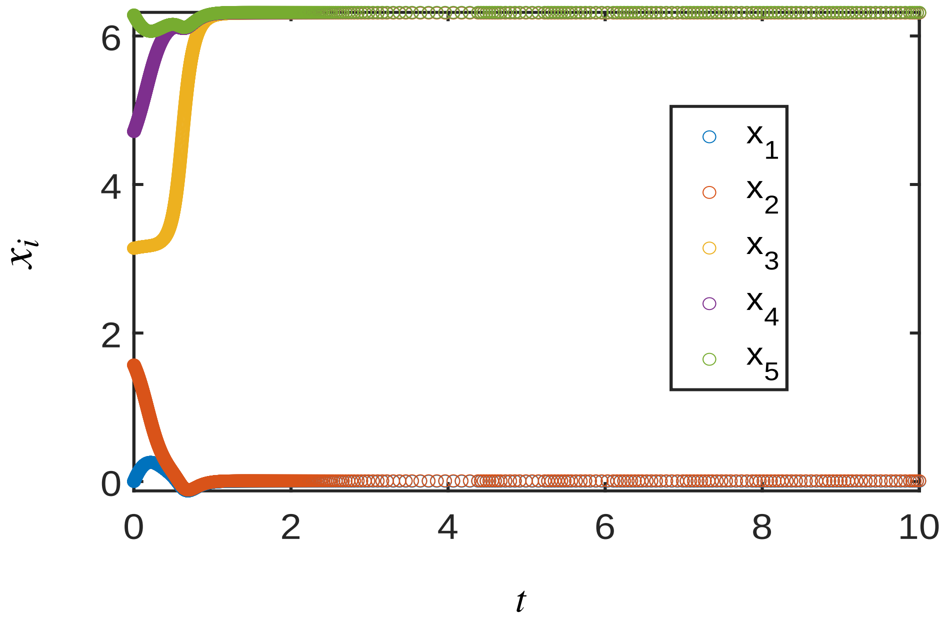

Figure 2.5 Stationary state of the spatially extended Kuramoto model using method-2 with $N = 6$ and $M = 2$.

In the case of all-all Kuramoto model, we can easily find the generalized form of the differential equations:

$$\begin{cases} \dot{x_1} = (\omega_2 - \omega_1) + \frac{K}{(N-1)}[-2\sin(x_1) + \sin(x_2 - x_1) + \sin(x_3 - x_1) + \ldots + \sin(x_{N-1} - x_1) \\ \qquad - \sin(x_2) - \sin(x_3) - \ldots - \sin(x_{N-1})] \\ \dot{x_2} = (\omega_3 - \omega_1) + \frac{K}{(N-1)}[-2\sin(x_2) + \sin(x_1 - x_2) + \sin(x_3 - x_2) + \ldots + \sin(x_{N-1} - x_2) \\ \qquad - \sin(x_1) - \sin(x_3) - \ldots - \sin(x_{N-1})] \\ \dot{x_3} = (\omega_4 - \omega_1) + \frac{K}{(N-1)}[-2\sin(x_3) + \sin(x_1 - x_3) + \sin(x_2 - x_3) + \ldots + \sin(x_{N-1} - x_3) \\ \qquad - \sin(x_1) - \sin(x_2) - \sin(x_4) - \ldots - \sin(x_{N-1})] \\ \vdots \\ \dot{x_i} = (\omega_{i+1} - \omega_1) + \frac{K}{(N-1)}\left[\sin(-x_i) + \sum_{\substack{j=1 \\ j\neq i}}^{N-1} \sin(x_j - x_i) - \sum_{j=1}^{N-1} \sin(x_j)\right], \; i = 1, \ldots, N-1 \end{cases} \tag{2.12}$$

In the spatially extended case, we solve the differential equations numerically as illustrated in Figure 2.6. We start the process by initializing the values of x_i. With the help of Eq. (2.10), we calculate θ_i, next we evaluate $\dot{\theta}_i$ from Eq. (2.2). Once, we calculate $\dot{\theta}_i$, then the last step is to switch from $\dot{\theta}_i$'s to $\dot{x}_i$'s by using Eq. (2.11).

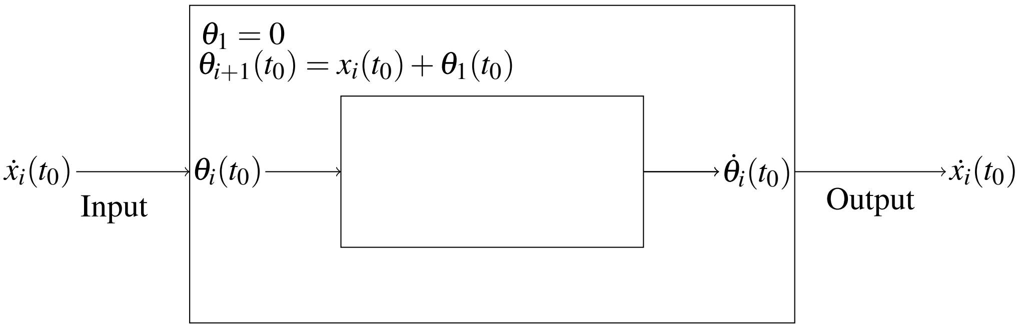

Figure 2.6 Wrapping process for finding the differential equations numerically in spatially extended networks.

2.2.2 Computing the fixed points and their stabilities

Stable fixed points in both methods 1 and 2 indicate a synchronized solution. We now describe how we calculate fixed points and their stability in both methods.

Fixed points for stationary pattern in a rotating frame (method-1)

To find the fixed points for our system Eq. (2.3), we put

$$\dot{\Theta}_i = 0, \qquad i = 1, ..., N \tag{2.13}$$

Or,

$$\dot{\Theta}_i = f_i(\boldsymbol{\theta}) - \Omega = 0, \qquad i = 1, ..., N \tag{2.14}$$

where $f_i(\boldsymbol{\theta})$ is given in Eq. (2.2). By using the Newton-Raphson method, we solve the system of equations for a stationary pattern.

$$\begin{bmatrix} \theta_1 \\ \theta_2 \\ \theta_3 \\ \theta_4 \\ \vdots \\ \theta_N \end{bmatrix}^{(n+1)} = \begin{bmatrix} \theta_1 \\ \theta_2 \\ \theta_3 \\ \theta_4 \\ \vdots \\ \theta_N \end{bmatrix}^{(n)} - \boldsymbol{J}^{(-1)} \begin{bmatrix} f_1(\theta_1, \theta_2, \theta_3, ..., \theta_{N-1}, \theta_N) - \Omega \\ f_2(\theta_1, \theta_2, \theta_3, ..., \theta_{N-1}, \theta_N) - \Omega \\ f_3(\theta_1, \theta_2, \theta_3, ..., \theta_{N-1}, \theta_N) - \Omega \\ f_4(\theta_1, \theta_2, \theta_3, ..., \theta_{N-1}, \theta_N) - \Omega \\ \vdots \\ f_N(\theta_1, \theta_2, \theta_3, ..., \theta_{N-1}, \theta_N) - \Omega \end{bmatrix}^{(n)} \tag{2.15}$$

Or,

$$\boldsymbol{\theta}^{(n+1)} = \quad \boldsymbol{\theta}^{(n)} - (\boldsymbol{J}^{-1})(\boldsymbol{f}(\boldsymbol{\theta}^{(n)}) - \boldsymbol{\Omega}) \tag{2.16}$$

In Eq. (2.16), n indicates the iteration number, $\boldsymbol{J}$ is the Jacobian of $f_i(\boldsymbol{\theta})$ and a superscript -1 indicates the inverse of the Jacobian. We can calculate the Jacobian as:

$$J_{ik} = \frac{\partial f_i(\boldsymbol{\theta})}{\partial \ \theta_k} \qquad i = 1, ..., N \qquad k = 1, ..., N \tag{2.17}$$

Thus, we can find the fixed point of our stationary pattern. The stability of our system is calculated by examining the eigenvalues of the Jacobian. If all the eigenvalues have negative real parts, then the fixed point is asymptotically stable.

Fixed point for relative positions (method-2)

The fixed point for Eq. (2.11) can be found using the Newton-Raphson method. In case of all-all Kuramoto model, we used the generalized form defined in Eq. (2.12) to find the Jacobian of the steady state. For all x_i defined in Eq. (2.12), let g function be defined as

$$\dot{x_i} = g_i(\boldsymbol{x}), \qquad i = 1, ..., N-1 \tag{2.18}$$

Then the Jacobian is defined as:

$$J_{ik} = \frac{\partial g_i}{\partial x_k}, \qquad i = 1, ..., N-1 \qquad k = 1, ..., N-1 \tag{2.19}$$

In a summation form, the Jacobian can be written as:
For the diagonal values:

$$J_{ii} = \frac{K}{(N-1)}\left[-2\cos(x_i) - \sum_{\substack{p=k \\ p\neq i}}^{N-1} \cos(x_p - x_i)\right], \qquad i = 1, ..., N-1 \tag{2.20}$$

For the off-diagonal values:

$$J_{ik} = \frac{K}{(N-1)}\left[(\cos(x_k - x_i) - \cos(x_k))\right], \qquad i = 1, ..., N-1 \quad k = 1, ..., N-1 \tag{2.21}$$

In the case of spatially extended network, we apply the same wrapping approach as illustrated in Figure 2.6 to compute the Jacobian.Let $\hat{\boldsymbol{J}}$ be the Jacobian with respect to the state variables θ_i and $\boldsymbol{J}$ be the Jacobian with respect to x_i. We expand the trigonometric term involved in Eq. (2.2) in terms of sine and cosine and use the connectivity matrix A_{ij} (already defined in Eq. (1.2)) to calculate the $\hat{\boldsymbol{J}}$.

For the off-diagonal values:

$$\hat{J}_{ik} = (-\sin\theta_i)\left(A_{ik}\frac{d}{d\theta_i}\cos\theta_i\right) + (\cos\theta_i)\left(A_{ik}\frac{d}{d\theta_i}\sin\theta_i\right),\ \ i = 1,\ldots N,\ \ k = 1,\ldots N \quad (2.22)$$

For the diagonal values:

$$\hat{J}_{ii} = \frac{d}{d\theta_i}(-\sin\theta_i)\left(A_{ik}\cos\theta_i\right) + \frac{d}{d\theta_i}(\cos\theta_i)\left(A_{ik}\sin\theta_i\right),\ \ i = 1,\ldots N \quad (2.23)$$

Using Eq. (2.11), Eq. (2.18) can be expressed as

$$\dot{x}_i = g_i(\boldsymbol{\theta}(\boldsymbol{x})), \qquad i = 1,...,N-1 \quad (2.24)$$

With $\dot{x}_i = g_i(\boldsymbol{x})$, $\dot{\theta}_i = f_i(\boldsymbol{\theta})$, $i = 1,...,N-1$, we can express Eq. (2.19) as

$$J_{ik} = \frac{\partial g_i}{\partial x_k} = \frac{\partial g_i}{\partial \theta_{k+1}} = \left[\frac{\partial f_{i+1}}{\partial x_{k+1}} - \frac{\partial f_1}{\partial x_{k+1}}\right], \qquad i = 1,...,N-1,\ k = 1,...,N-1 \quad (2.25)$$

Or, equivalently,

$$J_{ik} = \hat{J}_{(i+1,k+1)} - \hat{J}_{(1,k+1)}, \qquad i = 1,...,N-1,\ k = 1,...,N-1 \quad (2.26)$$

Hence, by using the relationship between J and $\hat{J}$ as defined in Eq. (2.26), we effectively switch from θ_i to x_i.

2.3 Numerical continuation of the Kuramoto models

The coupling strength, K, plays a crucial role in the existence and stability of fixed points in both of our Kuramoto networks. Previous work on the Kuramoto model (covered in Chapter 1) shows that by decreasing the value of one of the system's parameters, there exists a point where the solution is no longer stable and the system's state changes from coherent to incoherent. Everything could be synchronized and the solution converges, but altering just one parameter, K in our example, causes the entire network to become unstable. Thus, in order to fully understand the dynamics of our models, we investigate their stability by incorporating variations in the coupling strength K. This can be accomplished in two different ways.

One method involves integrating forward with some initial condition in time until it reaches a steady state. Then we slightly change the K value and repeat the process. Although the process is simple, there are many drawbacks. First, it takes a lot longer to reach a steady state. Secondly, this approach can only identify stable fixed points. Last but not least, for certain fixed K values, several stable fixed points could co-exist, and which one is reached depends entirely on the initial conditions we introduced.

The second method, which is more efficient, is the technique of numerical continuation. Details about the numerical continuation method we use in this thesis is discussed in appendix A.1. Here we briefly review the numerical continuation technique when it applies to Eq. (2.14) and follow its solutions as the parameter K varies.

2.3.1 Methodology

By using the numerical continuation technique, we follow the solutions of our spatially extended and all-all Kuramoto models as the parameter K varies. The system of equations defined in Eq. (2.2) and Eq. (2.1) can be written at steady state in a vector form as

$$F(\boldsymbol{\theta},K)=0 \tag{2.27}$$

As discussed in the previous section, we find the fixed point with the help of the Newton-Raphson method. Let $(\boldsymbol{\theta_0},K_0)$ be one of these solutions, we would like to find another nearby solution $(\boldsymbol{\theta_1},K_1)$, that satisfies Eq. (2.27). Following ideas discussed in appendix A.1 and Eq. (A.2), we get

$$(\boldsymbol{\theta_1}-\boldsymbol{\theta_0})^T\dot{\boldsymbol{\theta}}+(K_1-K_0)\dot{K}-\Delta s=0 \tag{2.28}$$

Here, superscript T is the transpose. Eq. (2.28) states the condition that the new point $(\boldsymbol{\theta_1},K_1)$ lies on the hyper-plane perpendicular to the tangent vector $(\dot{\boldsymbol{\theta_0}},\dot{K_0})$ and simultaneously at a distance Δs away from its closest point $(\boldsymbol{\theta_0},K_0)$. We also assume that the $(N+1)$ dimensional column vector, i.e.

$$\begin{pmatrix}\dot{\boldsymbol{\theta_0}}\\ \dot{K_0}\end{pmatrix} \tag{2.29}$$

is the null vector of the $N\times(N+1)$ matrix $(F_{\boldsymbol{\theta}}|\ F_K)$ where subscripts indicate partial derivatives. Hence, $F_{\boldsymbol{\theta}}$ is the $N\times N$ Jacobian of F with respect to $\boldsymbol{\theta}$ and F_K is the column vector of derivatives with respect to K that are evaluated at $(\boldsymbol{\theta_0},K_0)$. Once the vector Eq. (2.29) has been identified and normalized, it can be used in Eq.(2.28).

Thus, solving Eq. (2.27) and Eq. (2.28) simultaneously,

$$\begin{pmatrix} \boldsymbol{\theta}_{\mathbf{1}}^{(i)} \\ K_1^{(i)} \end{pmatrix} = \begin{pmatrix} \boldsymbol{\theta}_{\mathbf{1}}^{(i-1)} \\ K_1^{(i-1)} \end{pmatrix} - \boldsymbol{J}_{(i-1)}^{-1} \begin{pmatrix} F(\boldsymbol{\theta}_{\mathbf{1}}^{(i-1)}, K_1^{(i-1)}) \\ (\boldsymbol{\theta}_{\mathbf{1}}^{(i-1)} - \boldsymbol{\theta}_{\mathbf{0}})^T \dot{\boldsymbol{\theta}}_{\mathbf{0}} + (K_1^{(i-1)} - K_0)\dot{K}_0 - \Delta s \end{pmatrix} \tag{2.30}$$

for $i = 1, 2, \ldots N_e$, where N_e is defined as the number of iterations performed for convergence. Here,

$$\boldsymbol{J}_{(i)} = \begin{pmatrix} F_{\boldsymbol{\theta}} & F_K \\ \dot{\boldsymbol{\theta}}_{\mathbf{0}} & \dot{K}_0 \end{pmatrix} \tag{2.31}$$

is the $(N+1) \times (N+1)$ Jacobian of the augmented system, and the partial derivatives are evaluated at $(\boldsymbol{\theta}_{\mathbf{1}}{}^{(i)}, K_1^{(i)})$. As above, we take N_e Newtonian iterations (i.e. we assume that Eq. (2.30) has converged in such a way that $\boldsymbol{\theta}_{\mathbf{1}} = \boldsymbol{\theta}_{\mathbf{1}}^{(N_e)}$, $K_1 = K_1^{(N_e)}$ for an initial condition $\boldsymbol{\theta}_{\mathbf{1}}^{(0)} = \boldsymbol{\theta}_{\mathbf{0}} + \dot{\boldsymbol{\theta}}_{\mathbf{0}} \Delta s$, $K_1^{(0)} = K_0 + \dot{K}_0 \Delta s$. The stability of the fixed point $(\boldsymbol{\theta}_{\mathbf{1}}, K_1)$ depends on the eigenvalues of $F_{\boldsymbol{\theta}}$ evaluated at this point, whereas this matrix $F_{\boldsymbol{\theta}}$ has already been calculated as the top left $N \times N$ block in the Jacobian $\boldsymbol{J}$, see Eq. (2.31). We find the next solution $(\boldsymbol{\theta}_{\mathbf{2}}, K_2)$ in exactly the same way.

2.4 Variation of the coupling strength in the spatially extended network

In this section, we consider the spatially extended Kuramoto model with different numbers of oscillators and vary the coupling strength, K, using the numerical continuation technique. The results are computed in MATLAB using software we wrote (provided in the appendix A.3). We start the computation by considering the number of oscillators as $N = 6$ with a coupling range $M = 2$. The random natural angular velocities are uniformly distributed in an interval $[0, 1]$. Initially, all the oscillators are placed at $[0, 2\pi]$ interval. First, we calculate the average angular velocity of all the oscillators and subtract it from the system, Eq. (2.3). We then solve this system using the subroutine ode45 for some time t as shown previously in Figure 2.3. It should be noted that the same set of random angular velocities is reused for each K value, and the initial guess for the steady-state numerical integration is computed only once. The obtained steady-state solution from the direct integration serves as the initial guess for the numerical continuation technique. Subsequently, the numerical continuation technique is employed to generate a bifurcation diagram, depicting the stability and characteristics of all the stationary solutions, as the coupling strength K varies.

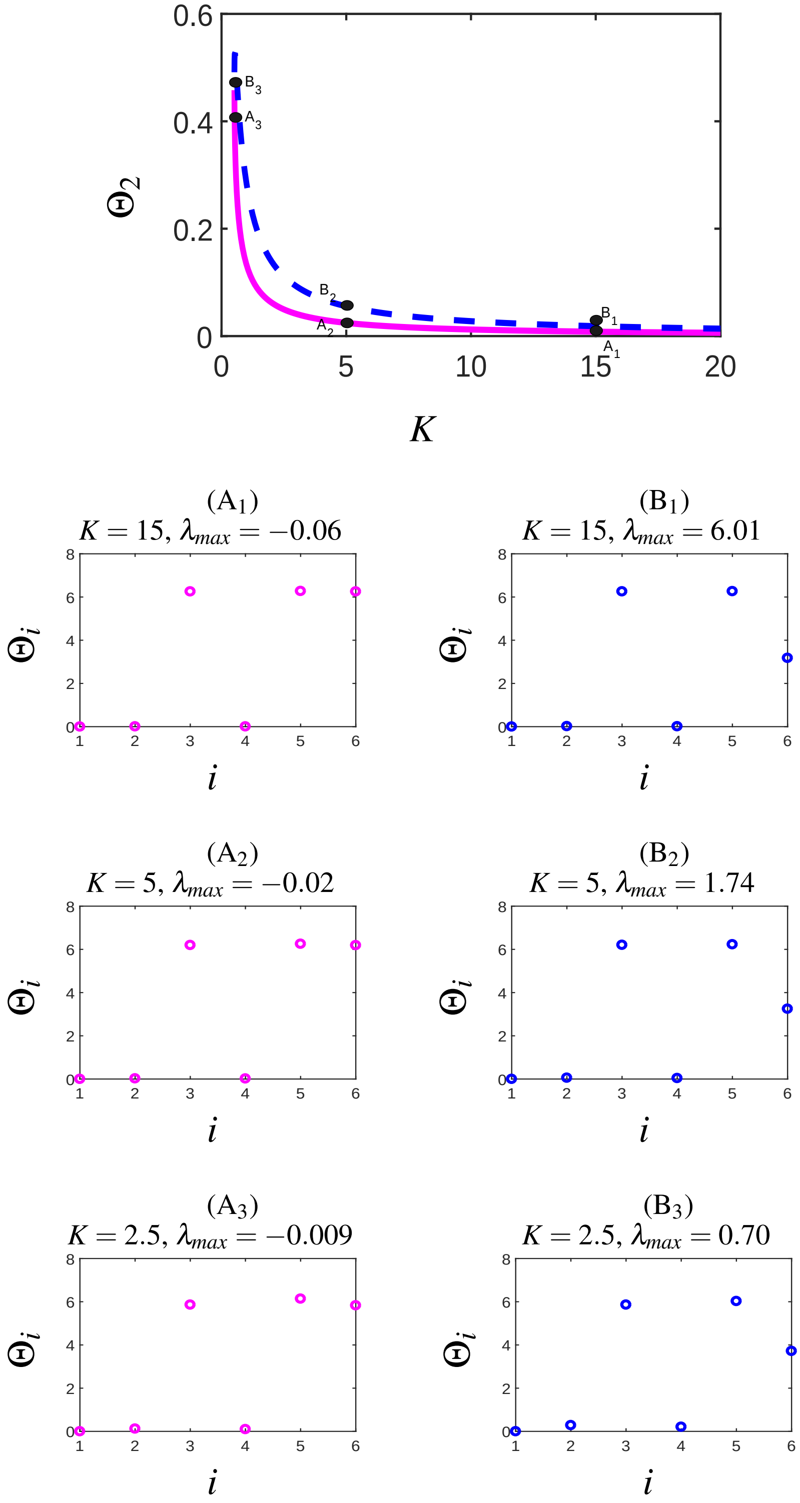

Figure 2.7 Solutions of spatially extended Kuramoto model with $N = 6$ and $M = 2$ using numerical continuation scheme as discussed in section 2.3.1. The figure at the top shows a bifurcation diagram of oscillator 2 as a function of the coupling strength K. Solid magenta line shows the stable solution, blue dashed line is the unstable solution. Sample steady state solutions for all the oscillators along the bifurcation curve are also shown.

In Figure 2.7, the results of spatially extended Kuramoto model as K varies with a numerical continuation scheme is presented. Here, the magenta solid line shows the stable solution for one of the individual oscillator Θ_2 in a steady state whereas the unstable solution for the same value of K are represented by blue dashed line. We investigate the overall behaviour of the state of oscillators for several values of K i.e. $K = 15$, $K = 5$, $K = 1$ (highlighted by A_1, A_2, A_3 on the stable branch and B_1, B_2, B_3 on the unstable branch) and calculate the maximum eigenvalue at the same values. It can be seen that the system's solution is stable as eigenvalues are negative until $K = 0.5159$, but as soon as we cross this point, one of the eigen value becomes positive and the solution becomes unstable. This is known as the point of saddle-node bifurcation.

2.4.1 Variation of coupling strength in the spatially extended Kuramoto model with $N = 100$ and $M = 5$.

In order to see how far the state of oscillators disperse for a stable and unstable branch, we increase the total number of oscillators to $N = 100$, for a spatially extended Kuramoto model with randomly uniformed distributed natural angular velocities, drawn from the interval $[0,1]$ and a coupling range $M = 5$. We place the oscillators with the initial conditions such that they all lie within an interval $[0,2\pi]$ and then evolve $\theta_i(t)$ for some time. We then apply the same approach as we did before, i.e. calculating a rotating pattern in a stationary state by subtracting the average frequency from the original system, then finding the fixed points of the stationary pattern with the Newton-Raphson method, and then varying the coupling strength K using numerical continuation technique. The results are shown in Figure 2.8.

The top figure in the middle of Figure 2.8 shows the state of one of the oscillators. The green line represents the stable branch whereas the blue line represents the unstable branch. The system is stable until $K = 1.313$ so this is the point of bifurcation. Again, we consider several values of K at different distances from the point of bifurcation. For $K = 15$ (A_1), at the stable branch, all the oscillators appear to be within the interval $[0,2\pi]$, however for the unstable branch, at the same value of K,(B_1) they appear to lie approximately between $[0,\pi]$. This is also true for $K = 5$ and $K = 2.5$.

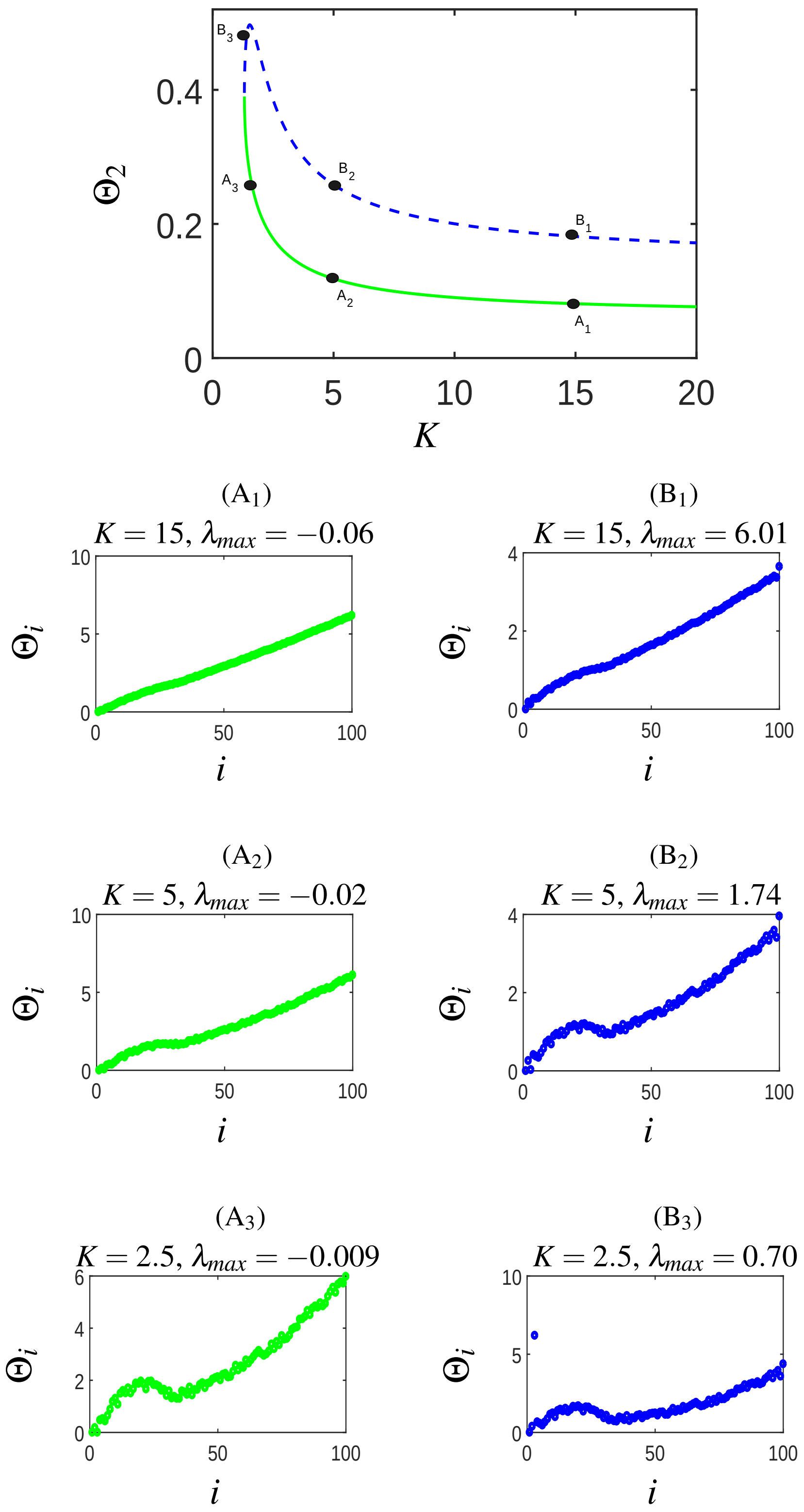

Figure 2.8 Solutions of spatially extended Kuramoto model with $N = 100$ and $M = 5$ using numerical continuation scheme as discussed in section 2.3.1. The figure at the top shows a bifurcation diagram of oscillator 2 as a function of the coupling strength K. Solid green line shows the stable solution, blue dashed line is the unstable solution. Sample steady state solutions for all the oscillators along the bifurcation curve are also shown.

2.5 Varying twisted states

In the previous section, we made an intriguing observation regarding the behavior of states in a spatially extended Kuramoto model when we increased the value of a coupling strength. Specifically, we discovered that the patterns generated by the oscillator's phases were distributed within the range of $[0, 2\pi]$ on a stable branch, but shifted to the range of $[0, \pi]$ on an unstable branch. This motivates us to consider setting up various initial conditions and analyse the behaviour of these states for stable and unstable branches. Thus, in the following section, we will analyse our spatially extended network by providing different initial conditions and observe the states of the oscillators.

Twisted states in spatially extended Kuramoto model

For the spatially extended Kuramoto model, we consider the same number of oscillators, i.e. $N = 100$ but vary the number of twists using different values of q. We call twist-0 to solutions in which the initial condition for the state of the oscillators remain the same, i.e. $\theta_i = 0$ for all i, twist-1 to solutions in which the state of oscillator phases grow for $[0, 2\pi]$. Similarly, twist-2 lies on $[0, 4\pi]$, twist-3 lies on $[0, 6\pi]$ and lastly twist-4 lies on the interval $[0, 8\pi]$. Hence, the general form for varying twisted states would then become $2\pi q$ where q is an integer or winding number used for varying the twists.

In Figure 2.9, we present all the twisted states we calculated (twist-0, twist-1, twist-2, twist-3, twist-4) as a function of the coupling strength K for one of the oscillator states Θ_2. Although their bifurcation point is different, their shape is the same, i.e. they all undergo saddle-node bifurcations. Moreover, the dashed line represents the unstable branch whereas the solid line is for the stable branch. We can also observe that the bifurcation point of twist-1 is lower than any other twists. In addition, the bifurcation point continues to increase for twist-2 and other higher twists. We can also observe that the higher twisted states exist for larger values of K.

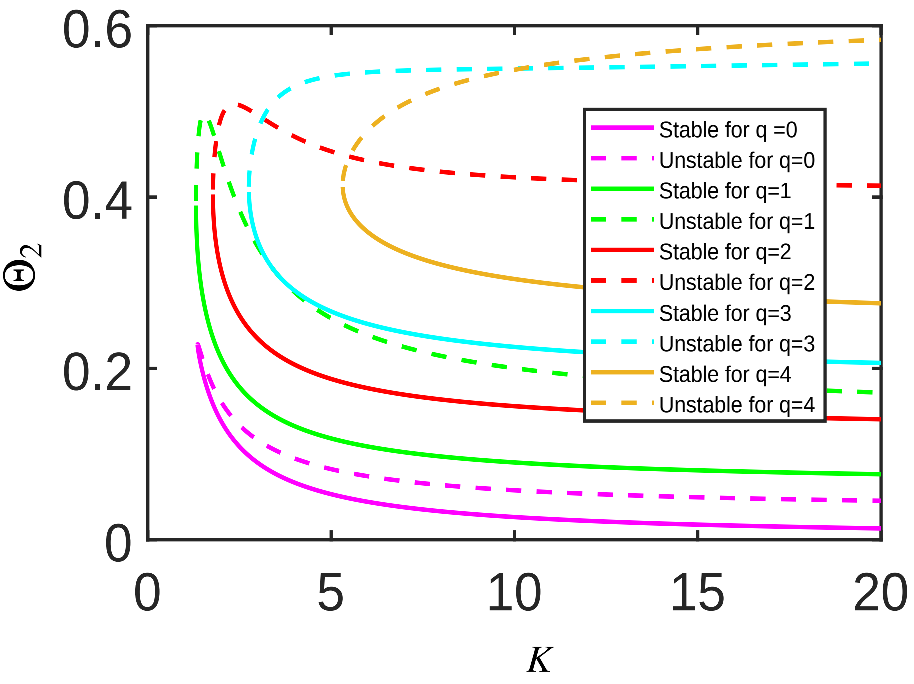

Figure 2.9 The bifurcation diagram illustrates the behavior of twist-0, twist-1, twist-2, twist-3, and twist-4 (q =0, 1, 2, 3, 4) as a function of the coupling strength K. The system parameters are set to $N = 100$ and $M = 5$, and the natural angular velocities are uniformly distributed (randomly).

To compare our results numerically for all the twisted states, we present the corresponding point of bifurcation for each twisted states in Table 2.1 below.

Number of Twists	Bifurcation Point
q=0	1.3571
q=1	1.3131
q=2	1.7762
q=3	2.7542
q=4	5.3154

Table 2.1 Bifurcation points for various twisted states with $N = 100$ and $M = 5$ and the natural angular velocities are uniformly distributed (randomly).

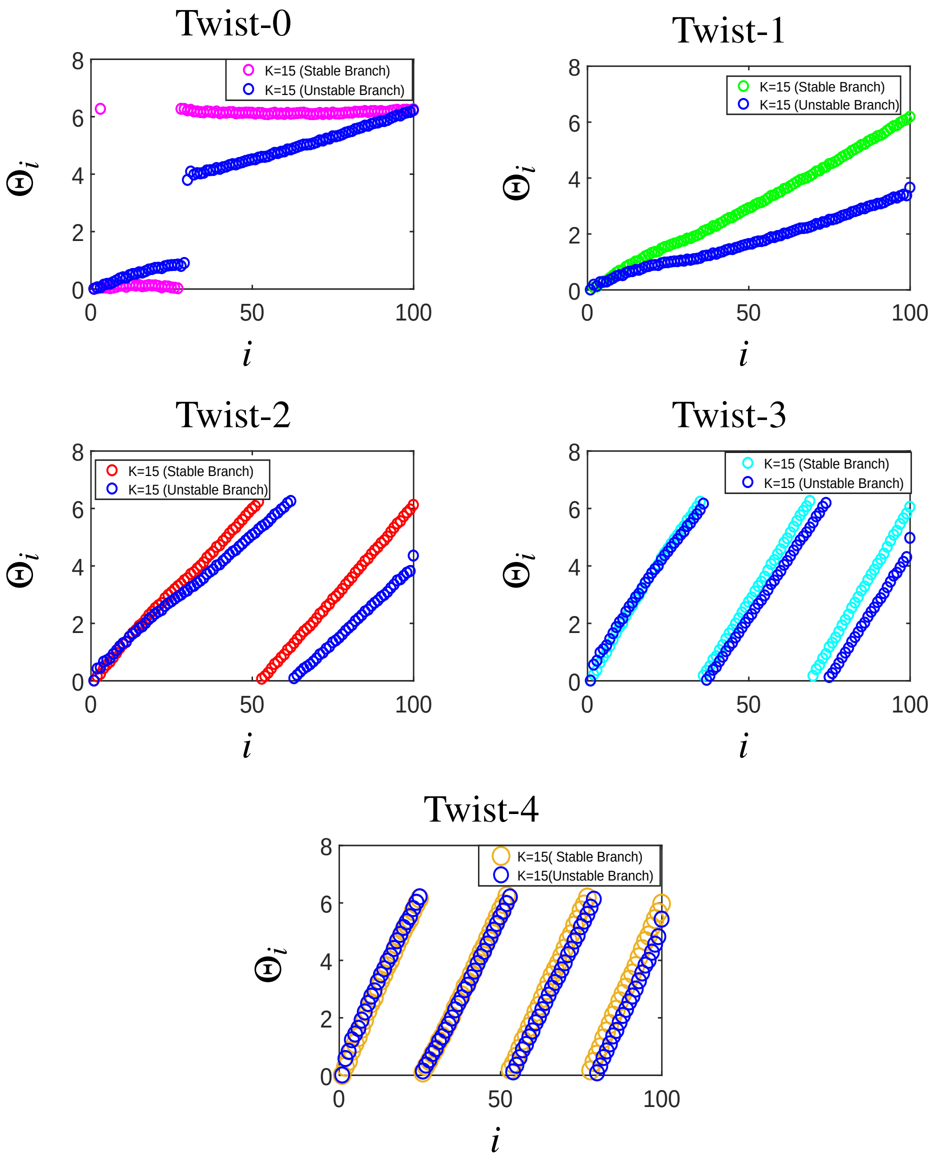

Figure 2.10 The states of 100 oscillators with different twisted states from both stable and unstable branches are observed. The system parameters are set to $N = 100$ and $M = 5$, and the coupling strength is fixed at $K = 15$. The natural angular velocities are uniformly distributed (randomly).

Figure 2.10 shows the state of the oscillators for various twisted states at $K = 15$. We consider the same condition, i.e. $N = 100$ oscillators and $M = 5$ for each of the twisted states. For all the twisted states, the blue pattern shows the results of the unstable branch. The stable branch of twist-0 is shown in magenta color. There exists a discontinuity for the unstable branch of twist-0. Although it appears from the unstable branch of twist-0 that the state of oscillators varies from 0 to 2π, if we place all these oscillators in a ring, it shows that there is a discontinuity of approximately 0.9852π in the middle. This suggests that all the oscillators will cover less than half of the circle and eventually become closer to 0 or equivalently to 2π. Therefore, we call it the twist-0 unstable branch.

For twist-1, Θ_i varies from 0 to 2π for the stable branch (in green color) and the oscillators cover more than half of the circle in the unstable branch, ranging from 0 to 3.365 radians.

For twist-2, with all the same conditions as above, the phases of the oscillators range from 0 to 4π for the stable branch (shown in red color), and for the unstable branch, the number of full circles covered is $\frac{(10.09 \text{ radians} - 0.416 \text{ radians})}{2\pi} \approx 1.5364$. So, the oscillators cover approximately 1.5364 full circles when arranged in a ring between 0.416 and 10.09 radians. To be even more precise, the oscillators complete one full revolution (2π radians) and then cover an additional $0.5364 \times 2\pi$ radians, which is approximately 3.365 radians beyond the one full revolution. This means they cover one complete revolution and a little over half of another revolution.

For twist-3, the oscillators cover approximately 2.6783 full circles. In the stable branch, the phases of the oscillators range from 0 to 6π radians (shown in cyan color). For the unstable branch, the number of full circles covered is $\frac{(16.86 \text{ radians} - 0.5529 \text{ radians})}{2\pi} \approx 2.6783$. So, the oscillators cover approximately 2.6783 full circles when arranged in a ring between 0.5529 and 16.86 radians. To be even more precise, the oscillators complete two full revolutions (2π radians each) and then cover an additional $0.6783 \times 2\pi$ radians, which is approximately 4.259 radians beyond the two full revolutions. This means they cover two complete revolutions and a little over half of another revolution.

For twist-4, the oscillators cover approximately 3.7355 full circles. In the stable branch, the phases range from 0 to 8π radians (shown in brown color). For the unstable branch, when the oscillators are arranged in a ring and cover the region from 0.5728 to 23.67 radians, they cover approximately 3.7355 full circles, which is almost three and three-quarters of a full revolution.

2.6 Varying the coupling range

Previously, we were considering $N = 100$ and $M = 5$ for our spatially extended Kuramoto model. In this section, we gradually increase the coupling range, M for a spatially extended network and analyze the stability by evaluating the point of bifurcations using the same numerical continuation scheme as discussed in section 2.3.1. First, we consider a case for which $N = 100$ and $M = 25$. Then, we increase the coupling range further by considering $N = 100$ and $M = 50$. For both cases, we discuss the twisted states and the state of oscillators at various values of K. We can observe that as the coupling range increases to a certain limit, the only existing twisted states is twist-0. Moreover, when the value of the coupling range becomes equal to half of the number of oscillators, the system has the same bifurcation point as for the all-all Kuramoto model.

2.6.1 $N = 100, M = 25$

We consider the number of oscillators as $N = 100$ but increase the coupling range from $M = 5$ to $M = 25$. Here in Figure 2.11, the middle bigger figure presents the bifurcation diagram for which the coupling strength varies using numerical continuation scheme. The unstable branch is presented in blue color while the pink color shows the stable branch. The point of bifurcation is at $K = 2.24$. We pick three different values of K to check the state of the oscillators at these values; the stable and unstable branches are shown in pink and blue color respectively, the state of the oscillator show twist-1.

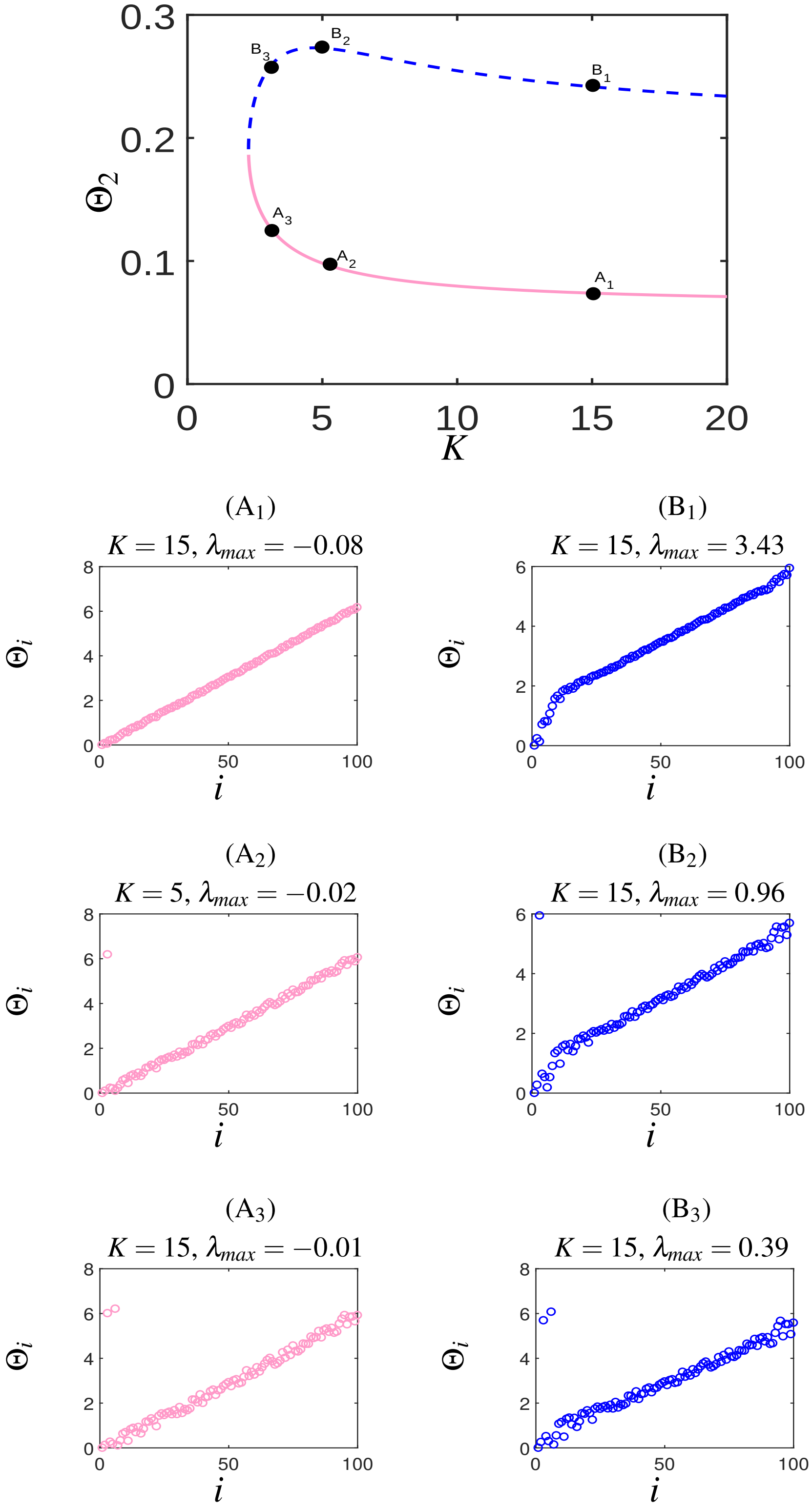

Figure 2.11 Solutions of spatially extended Kuramoto model with $N = 100$ and $M = 25$ using numerical continuation scheme as discussed in section 2.3.1. The figure at the top shows a bifurcation diagram of oscillator 2 as a function of the coupling strength K. Solid pink line shows the stable solution, blue dashed line is the unstable solution. Sample steady state solutions for all the oscillators along the bifurcation curve are also shown.

2.6.2 $N = 100$ and $M = 50$, all-all Kuramoto model

We now increase the coupling range further while keeping the other conditions the same. Figure 2.12 shows the stable branch in magenta color whereas the unstable branch is shown with the blue color. The point of bifurcation lies at $K = 0.6431$. We can observe from the state of oscillators at various K values that the phases are having twist-0.

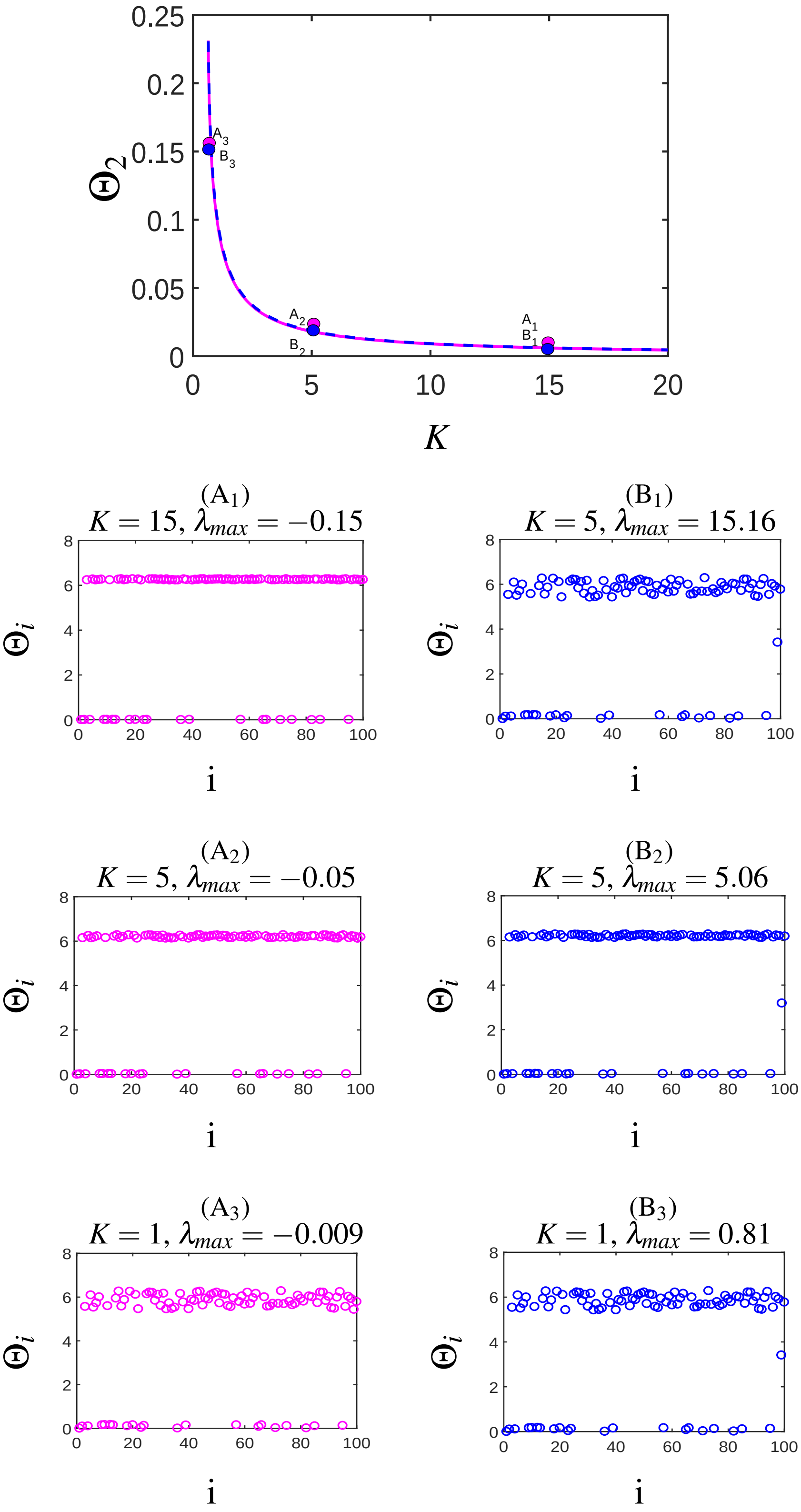

Figure 2.12 Solutions of spatially extended Kuramoto model with $N = 100$ and $M = 50$ using numerical continuation scheme as discussed in section 2.3.1. The figure at the top shows a bifurcation diagram of oscillator 2 as a function of the coupling strength K. Solid magenta line shows the stable solution, blue dashed line is the unstable solution. Sample steady state solutions for all the oscillators along the bifurcation curve are also shown.

Next, we consider the same number of oscillators, with $K = 15$ and varying the coupling range starting from $M = 2$ to $M = 50$. We are interested in finding out the relationship between the twisted states and the coupling range M. Figure 2.13, shows all the coupling range values that give twist-3 solutions. We can see that twist-3 exists for all the values from 2 to 9. However, when we slightly increase the coupling range to $M = 10$, the state of the oscillators change- we can no longer get twist-3 and instead get twist-2. This state of oscillators exists until $M = 14$. After increasing the coupling range further we get the twist-1 solutions for all the M values ranging from 15 to 32. However, as soon as the coupling range increases to $M = 33$, twist-1 state of the oscillators turned to twist-0. In general, we can conclude that the higher twisted states exists at the lower values of M.

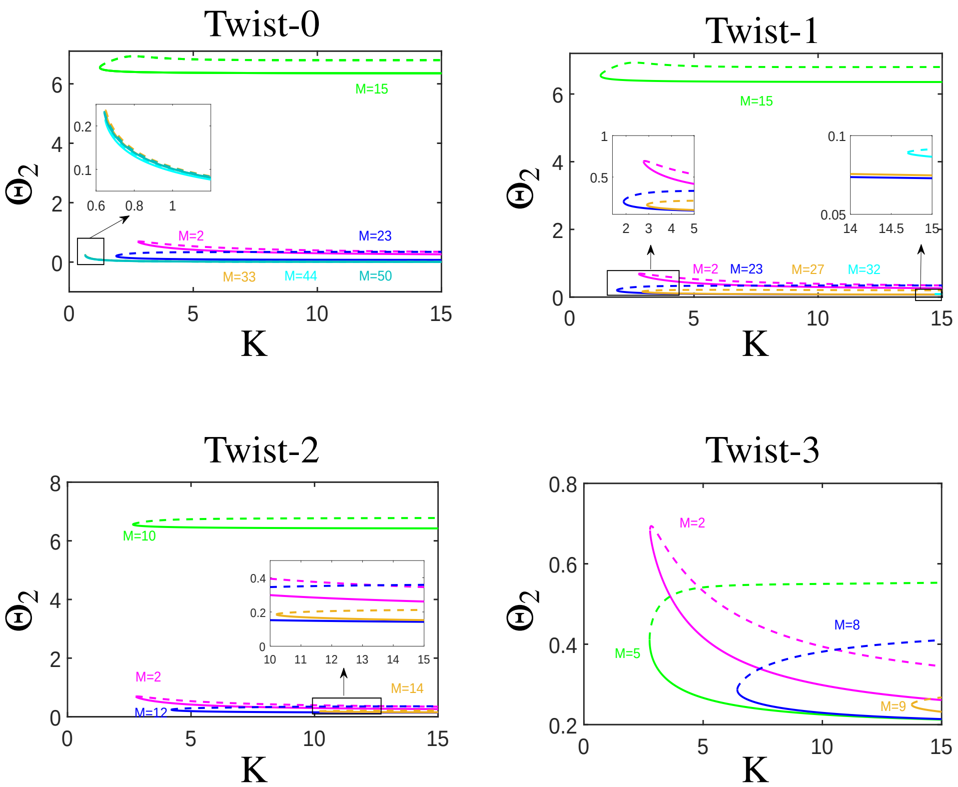

Twist-0

Twist-1

Twist-2

Twist-3

Figure 2.13 Bifurcation diagrams for various twisted states. We can see that the higher twisted states exist for lower values of M. But as we increase the coupling range and the more oscillators connect to each other, the number of possible twisted states decreases until the only possible solution is twist-0.

In order to check the numerical integrity of our results we compare the calculation we did by solving Eq. (2.3) where $N = 100$, $M = 50$ with our own software (discussed in appendix A.3) and the calculation done by CLMATCONT-L (an advanced numerical bifurcation software, built in MATLAB, for studying large scale dynamical problems, [6]) when solving the Eq. (2.11) with $N = 100$, $M = 50$ using method-2. In Figure 2.14, we present a comparison of results from CLMATCONT-L and our own software.

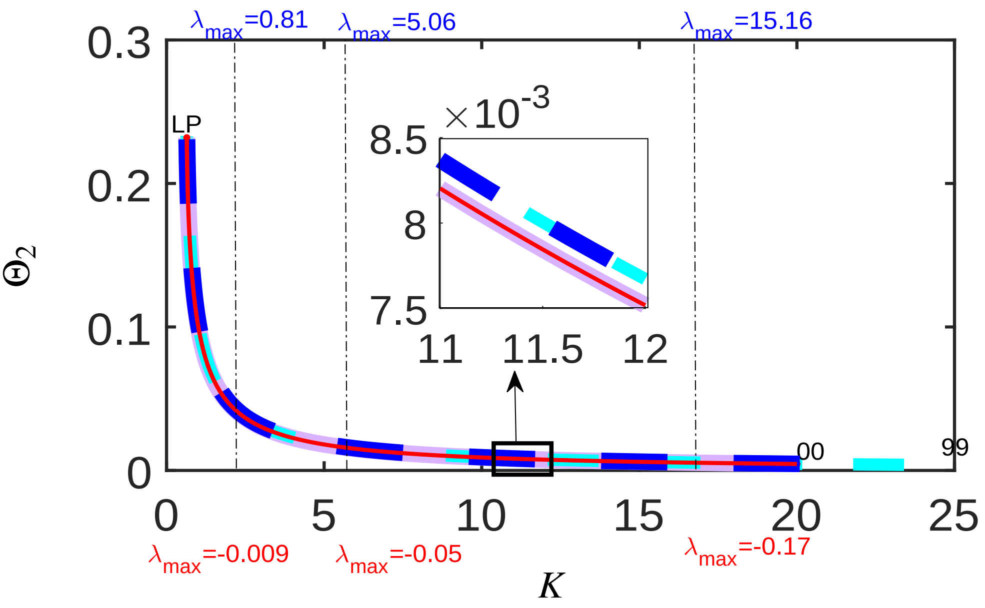

Figure 2.14 A bifurcation diagram created with our own software compared to the one created with CLMATCONT-L. Our results are shown in solid red for the stable branch and the blue dashed line for the unstable branch. The CLMATCONT-L results are shown in purple for the stable branch and the cyan dashed line for the unstable branch. Here, "00" means the K value from where the bifurcation starts, "LP" means the limit point or the bifurcation point", which in this case is $K = 0.6431$ and "99" means the last value of K where the numerical continuation ends. As can be seen, our calculation agrees well with the calculation obtained in CLMATCONT-L.

2.7 Discussion and Conclusions

In this Chapter, we numerically analyzed the transition between spatially extended Kuramoto network and all-all Kuramoto network. We discussed two methods, one in which we analyzed the system in a rotating frame and a second in which we considered the relative position of the oscillators. We used both methods to find the fixed points. We also presented a proof to show that for both networks, the synchronized angular velocity of the oscillators is equal to the average of the natural angular velocities. Finally we analyzed various twisted states in both networks and showed numerically that the twisted states exist for lower values of the coupling range, M. Thus, by gradually increasing the coupling range, more oscillators connect with each other and the only twist we get for the all-all network is twist-0. We ended the chapter by comparing our numerical results with those obtained by another software (CLMATCONT-L) and showed that we get the same results. This will become important when we use our software to implement the equation free approach as later we compare the solutions obtained from an equation-free approach with the actual detailed system.

Chapter 3

An Equation-Free Approach for the All-All Kuramoto Network

In this chapter, we discuss how a large system of synchronized oscillators, the all-all Kuramoto network, can be represented by a smaller number of variables using an "equation-free approach". We discuss the equation-free approach and implement a coarse-projective integeration to check and improve the efficiency of our calculations.

3.1 Development

We begin by making the observation (also made by [5]) that once all the oscillators synchronize, their state becomes a function of their natural frequencies ω_i, as shown in Figure 3.1. The figure shows the solution of Eq. (2.1) with $N = 100$, coupling strength $K = 0.7$ whereas the frequencies are uniformly distributed between [0,1] interval. Figure 3.1 (a) shows the state of the oscillators as a function of time t and Figures 3.1 (b-c) show the state of oscillators as a function of the natural frequencies at times $t = 0$, $t = 12$ and $t = 50$ respectively.

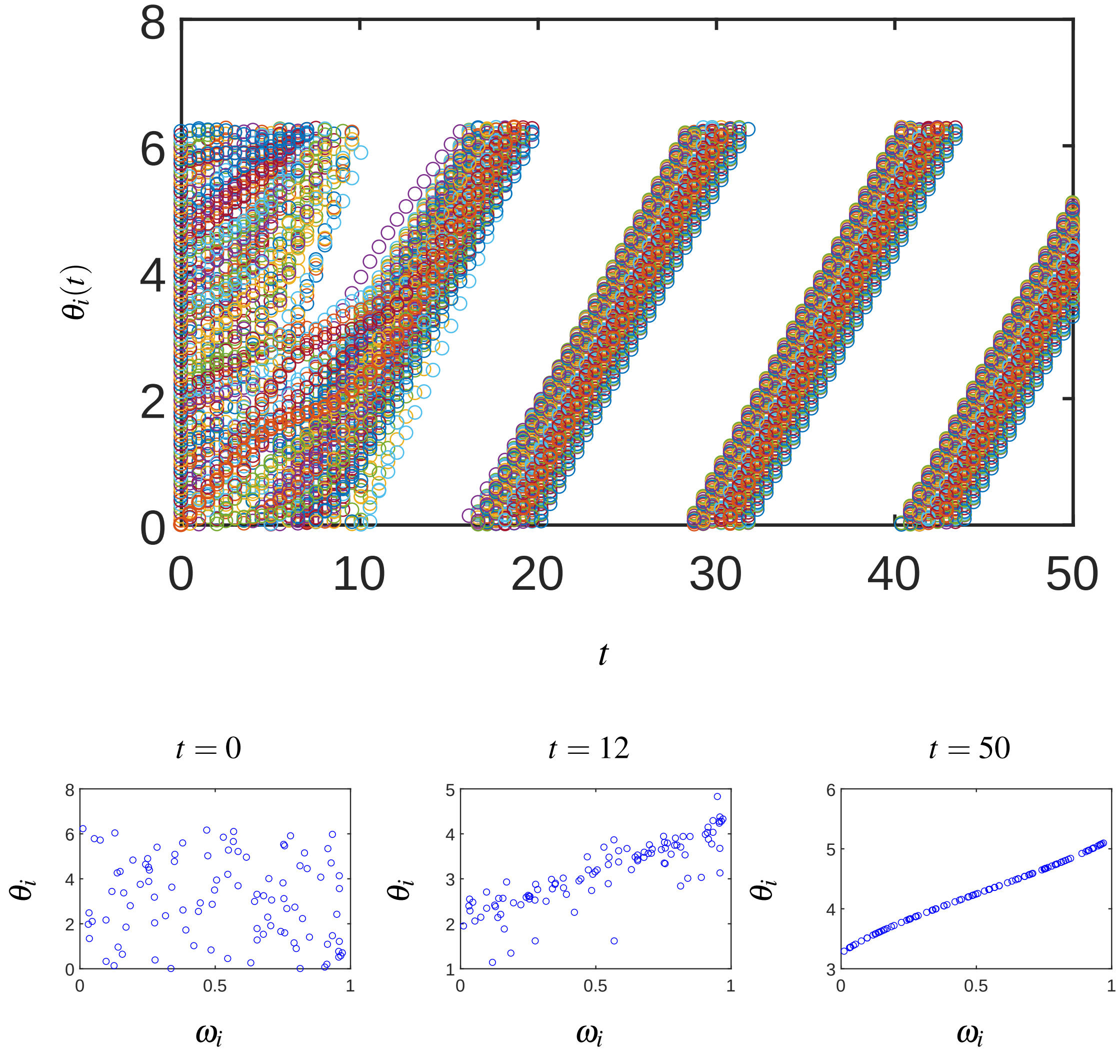

Figure 3.1 Solution of the dynamical system in Eq. (2.1) with $N = 100$, $K = 0.7$, and ω_i are the uniformly distributed random frequencies between [0,1]. (a) Evolution of θ_i as a function of time, t. (b)-(c) θ as a function of ω_i at $t = 0$, $t = 12$ and $t = 50$ respectively. It can be seen that once the oscillators synchronized, θ_i becomes a function of ω_i.

This correlations between θ_i and ω_i allows us to expand θ_i (microscopic variables) in certain polynomial classes of ω_i, known as polynomial expansion, (given in the appendix A.2). Since we have taken ω_i from a uniform distribution, we will use the shifted Legendre polynomials (set of functions similar to the Legendre polynomials, but orthogonal on the interval [0,1]) which provides the fastest convergence of the expansion [64].

Thus, we can write

$$\theta_i(t) \approx \sum_{k=1}^{n} a_k(t)\phi_k(\omega_i), \qquad i = 1 \dots N \tag{3.1}$$

where $\phi_k(\omega_i)$ are the shifted Legendre polynomials, $a_k(t)$ are n low dimensional variables and $\theta_i(t)$ are N high dimensional variables. Given a particular detailed realization of the oscillator state, these polynomial coefficients a_k's are estimated by minimizing the quantity:

$$\sum_{i=1}^{N}\left[\theta_i - \sum_{k=1}^{n} a_k(t)\phi_k(\omega_i)\right]^2 \tag{3.2}$$

This is referred to as a *Restriction operator* in an equation-free approach. It can be reformulated as an over-determined linear system whose least-squares solution can be calculated by the *backslash operator* in Matlab. We also need a *Lifting operator* to execute an equation-free approach, which involves considering a_k with a particular ω_i realization. Thus, it is defined as:

$$\theta_i(t) = \sum_{k=1}^{n} a_k(t)\phi_k(\omega_i), \qquad i = 1,\ldots,N \tag{3.3}$$

With these two operators, Eq. (3.2) and Eq. (3.3), we now implement an equation-free approach. Here, we present an overview of the method for applying an equation-free approach.

3.2 Methodology of applying an equation-free approach to the all-all Kuramoto network

In an equation-free approach, an adequately initialised short burst of detailed simulations is used to estimate the appropriate quantity for the solution of low-dimensional systems. The general steps consist of:

1. Identifying a collection of macroscopic variables that sufficiently describe the coarse-grained dynamics. We assume that the dynamical system at the level of coarse observables exists but we don't have the equations explicitly. For the all-all Kuramoto network, our macroscopic variables are a_k.
2. Drawing ω_i randomly, and saving the selection for all future calculations.
3. Constructing a lifting operator , as defined in Eq.(3.3), mapping the coarse description to (one or more) consistent fine-scale realizations.
4. Evolving the lifted, fine-scale initial conditions for a certain time horizon.

5. Restricting the resulting fine-scale description to the coarse observables, i.e finding the polynomial coefficients a_k of the final state variables $\theta_i(t)$, using the restriction operator, specified in Eq.(3.2).

6. Repeating the procedure for steps 3, 4 and 5 as needed.

We follow the above steps and compare the actual solutions (without using an equation-free approach) and the approximated solution (with an equation-free approach).

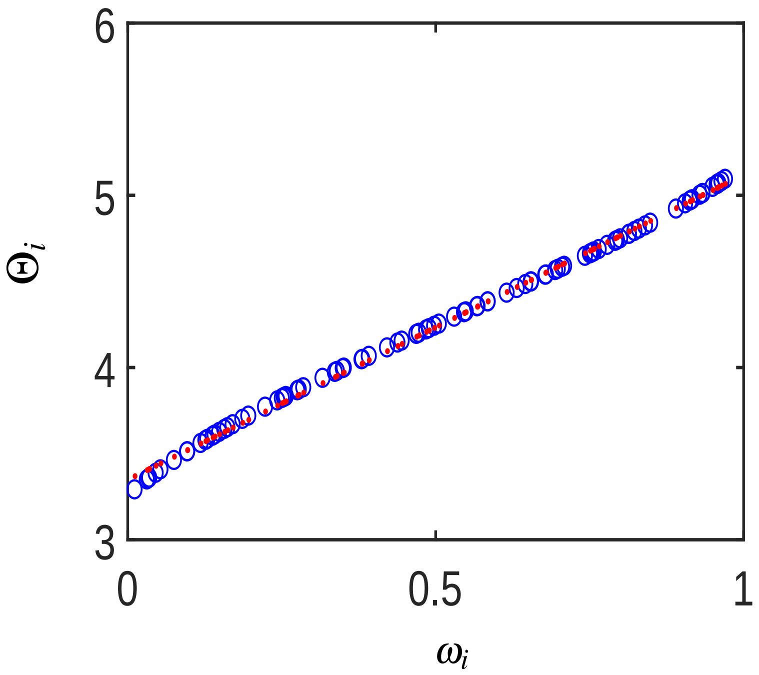

Figure 3.2 Snapshot of θ_i as a function of ω_i. Blue circles represent the actual solutions of Eq. (2.1) with $N = 100$ and $K = 0.7$ whereas the red dots represent the solution of an equation-free approach using only 2 shifted Legendre polynomials ($\phi_1 = 1, \phi_2 = 2\omega_i - 1$).

Figure 3.2 shows a comparison between the steady state solution as calculated using Runge- Kutta method with the full network of 100 oscillators (shown in blue circles) and the steady state solution as calculated using the equation-free approach with only 2 shifted Legendre polynomials (shown in red dots). These two shifted Legendre polynomials are $\phi_1 = 1, \phi_2 = 2\omega_i - 1$. In both simulations, the value of the coupling strength is $K = 0.7$. As can be seen the relationship between θ_i and ω_i is captured well with the equation-free approach.

3.3 Coarse-projective integration of all-all Kuramoto network

We now briefly demonstrate the coarse-projective integration of low-dimensional variables. The method involves short simulations of the high dimensional system to derive the time projection of the low dimensional variables.Let the high dimensional variables be presented as

$$\boldsymbol{\theta} = [\theta_1, \theta_2, ..., \theta_N] \in R^N \tag{3.4}$$

The low dimensional polynomial coefficients are then defined as

$$A = [a_1, a_2, ..., a_k] \in R^k \tag{3.5}$$

Given $\boldsymbol{\theta}(t_1)$, we integrate Eq. (2.1) with N_1 time steps. Using the restriction operator, specified in Eq. (3.2), we calculate A in the last two time steps. Next, we use the last two values from A to extrapolate the value of A at some time t_2 in the future. We then lift from $A(t_2)$ to $\boldsymbol{\theta}(t_2)$ by using the lifting operator defined in Eq. (3.3). The procedure is repeated as shown in the Figure 3.3. It should be noted that if the cost of restricting, extrapolating and lifting is small compared to the cost of integrating the network for the entire time, this procedure will be faster than directly integrating the network.

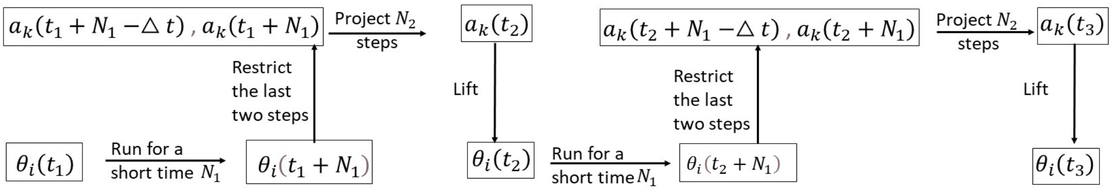

Figure 3.3 Schematic diagram of the coarse-projective integration.

3.3.1 Varying the integration time and projection times.

In this section, we explore the effect of varying N_1, (the integration time of the high dimensional system) on the coarse-projective integration when only three coarse-grained variables are used. We consider all-all Kuramoto network as discussed in section 3.1. ($N = 100$, $K = 0.7$, random uniformly distributed frequencies).

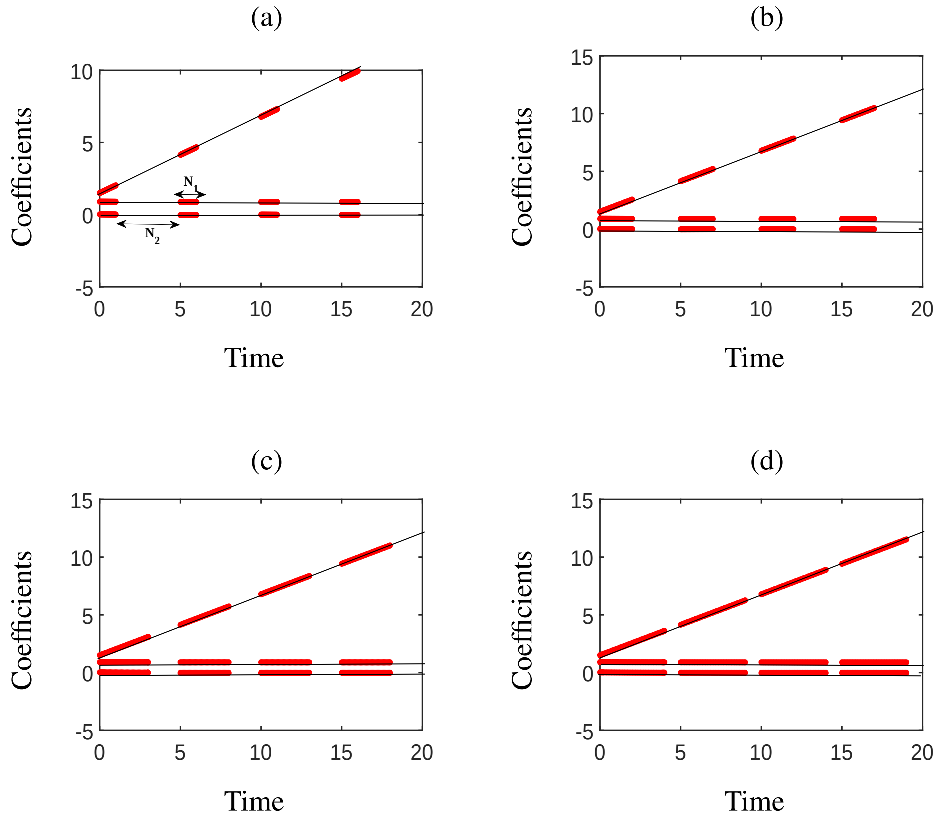

Figure 3.4 The effects of variation in N_1 and N_2 on a coarse projective integration with three coarse grained coefficients a_1, a_2 and a_3. For (a) $N_1 = 1$ and $N_2 = 4$, (b) $N_1 = 2$ and $N_2 = 3$, (c) $N_1 = 3$, $N_2 = 2$, (d) $N_1 = 4$, $N_2 = 1$. The red dots represent the results of the coarse-grained variables after applying the coarse-projective integration, while the black line shows the result of the coarse-grained variables when there is no coarse projection involved.

Following the process described in the Figure 3.3, we consider $n = 3$, so that our choice of coarse-grained variables becomes a_1, a_2, and a_3 to estimate $\theta_1, \theta_2, ..., \theta_{100}$. In order to perform the coarse-projective integration, local time derivatives of the coarse observables are estimated by using the last two values from each curve and then projecting them for some time. After the projection, we lift the coarse variables again to the consistent fine-scale realizations and use them as an initial condition for another short burst of direct detailed integration. The resulting values are then restricted and the whole process repeats again. Thus, we vary N_1 from 1 to 4 in each of the cases, given in Figure 3.4, with the projection size N_2 varies correspondingly. In Figure 3.4 (a) $N_1 = 1$ and $N_2 = 4$, Figure 3.4 (b) $N_1 = 2$ and $N_2 = 3$, Figure 3.4 (c) $N_1 = 3$, $N_2 = 2$ and Figure 3.4 (d) $N_1 = 4$, $N_2 = 1$. Figure 3.5 shows the error between the true solution (when the full integration is carried out) and the solution we evaluated with the coarse-projective integration at the value of time $t = 20$. Figure 3.5(a) indicates that coarse-projection error increases as the projection length N_2 increases.

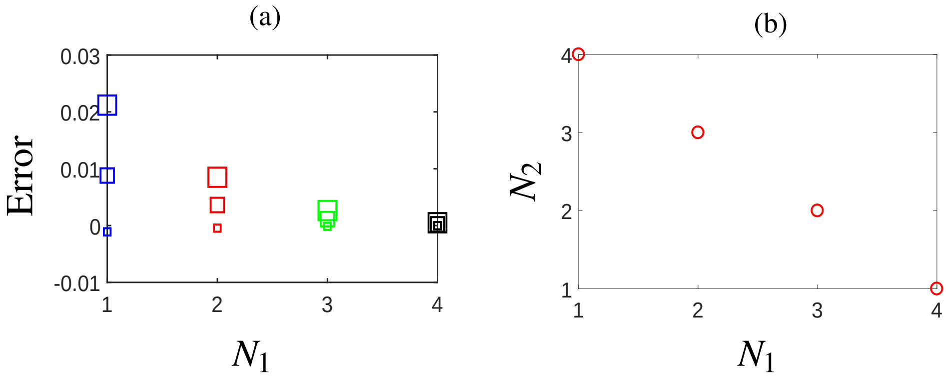

Figure 3.5 (a)-Error between the solution obtained by full integration and the solution obtained by projective integration for N_1 =1,2,3,4 with three coarse-grained coefficients. The smallest rectangle represents a_1, the medium is for a_2, while the largest rectangle is for a_3. (b)-Relationship between N_1 and N_2 shows $N_2 = 5 - N_1$.

In Figure 3.6, we take the size of the projection N_2 as 5,7,9,11 while keeping $N_1 = 3$. We follow the same procedure as discussed above. The total time to be considered is 40 units. The cyan circles represent the coarse grain coefficients with the projective integration, while a full detailed simulation is given by the blue line. It can be seen in Figure 3.6 that as the length of the projection increases, the integration loses its accuracy.

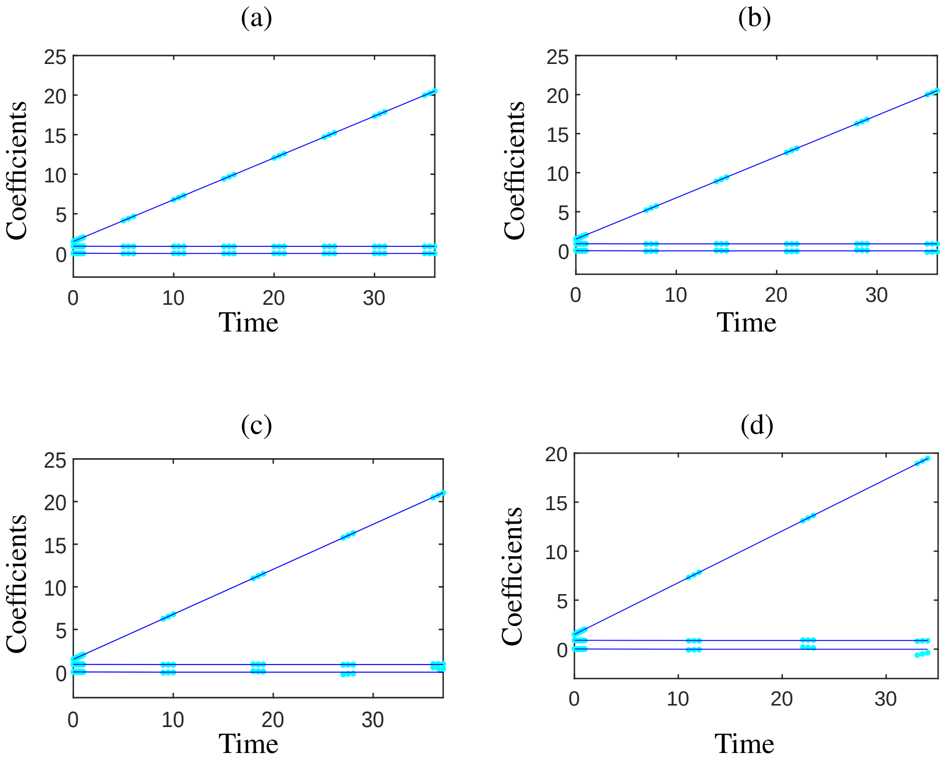

Figure 3.6 The effects of variation in N_2 on a coarse projective integration with three coarse grained coefficients a_1, a_2 and a_3, while considering $N_1 = 3$. For (a) $N_2 = 5$, (b) $N_2 = 7$, (c) $N_2 = 9$, and (d) $N_2 = 11$. The cyan circles represent the results of the coarse-grained variables after applying the coarse-projective integration, while the blue line show the results of the coarse-grained variables when there is no coarse projection.

In Figure 3.7, we calculate the error between the coarse variables of the true solutions and the one with the coarse projective integration at $t = 40$. It can be observed that the error of each coefficient a_1, a_2 and a_3 increases as the projection duration increases.

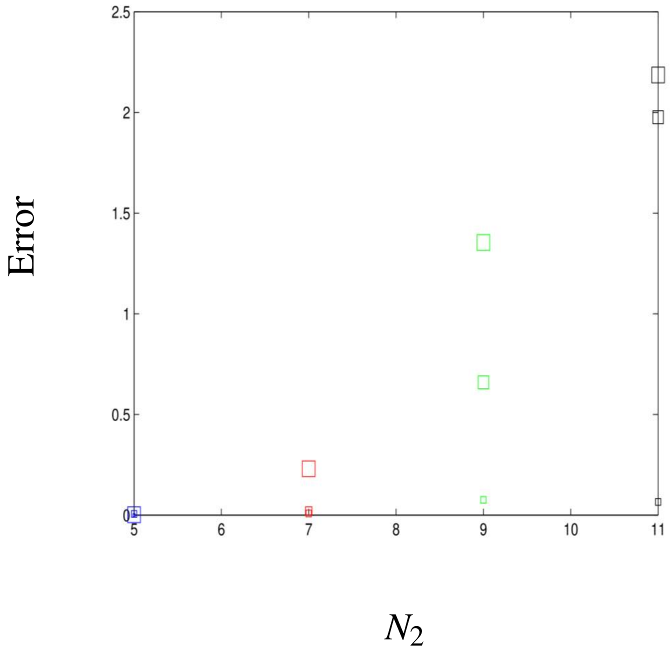

Figure 3.7 Error of the coarse-projective integration when N_2 is taken as 5, 7, 9, 11 for a_1 (smallest rectangle), a_2 (medium rectangle) and a_3 (the largest rectangle).

3.4 Discussion and Conclusions

In this chapter, we utilized polynomial expansion to reduce the dimensionality of a large network, which contains a heterogeneous population of Kuramoto oscillators with an all-all coupling structure. The idea of estimating the polynomial coefficient when there exists a rapid correlation between the state of the oscillators and the heterogeneous frequencies was taken from Bertalan et al. [5], who used an equation-free approach on a Kuramoto model. However, the authors expanded the coarse-grained coefficients using univariate polynomials. Laing and Troy [35] also used a polynomial expansion, but they solved a different set of differential equations with the frequencies taken from a Gaussian distribution and chose Hermite polynomials to achieve faster convergence of the expansion. Xiu and Karniadakis [64] showed that for a uniform distribution of frequencies, Legendre polynomials provide faster convergence, and in the case of a gamma distribution, Laguerre polynomials are best. Hence, we considered the uniform distribution of frequencies and used the shifted Legendre polynomials with an equation-free approach to demonstrate the coarse-projective integration for a detailed system.

Chapter 4

Creating Bifurcation Diagrams Using the Equation-Free Approach in One Dimension

In Chapter 2, we applied a numerical continuation technique to create bifurcation diagrams of a large system of coupled oscillators. In this chapter, we use the equation-free approach to create bifurcation diagrams for the coarse-grained system. This helps us estimate the behaviour of a high dimensional system by a smaller number of variables (the coarse-grained variables) and study the overall emergent behaviour of the detailed system. First, we briefly discuss the implementation of an equation-free approach along with the numerical continuation technique. Then, we compute the bifurcation diagrams at the coarse level and compare them with the results of the detailed system- (already computed in Chapter 2).

4.1 Finding the derivatives of coarse-grained coefficients using an equation-free approach

In Chapter 2, we observed that when M (coupling range) is small, θ_i becomes a monotonically increasing function of their positions therefore we now consider this case and express our high dimensional variables, θ_i as:

$$\theta_i(t) = \sum_{k=0}^{n} a_k(t) v_k(i), \qquad i = 1 \ldots N \tag{4.1}$$

where, a_k are the time dependent coarse grained coefficients, v_k are the spatial functions, n is the maximum number of coarse-grained variables, i is the position of the oscillators and N is the total number of oscillators. We considered v_k as $v_k = (i-1)^k$, $k = 0, ..., n$ and we choose $a_0 = 0$. This gives us $v_k = 0$ at $i = 1$ and this polynomial representation is allowed when θ_i goes beyond 2π (we do not use modulus of 2π as given in Figure 2.10).

Eq. (4.1) is our lifting operator, denoted by L, creating the fine scale initial conditions consistent with the prescribed values of the macroscopic observable,

$$L(\boldsymbol{a}) = \boldsymbol{\theta}. \tag{4.2}$$

The restriction operator is defined as

$$\Re : min\left[\sum_{i=1}^{N}\left[\theta_i(t) - \sum_{k=0}^{n} a_k(t)v_k(i)\right]^2\right] \tag{4.3}$$

Or,

$$\Re(\boldsymbol{\theta}) = \boldsymbol{a} \tag{4.4}$$

Thus, given the detailed variables, θ_i, we find the macroscopic variables such that the relationships in Eq.(4.3) are minimized. This calculation can be done in Matlab by using a backslash operator. The two operators given in Eq. (4.1) and Eq. (4.3) must satisfy the condition of consistency, i.e

$$\Re(L(\boldsymbol{a})) = \boldsymbol{a} \tag{4.5}$$

In order to find the derivatives for a given set of coarse-grained coefficients, we use the lifting operator to find the values of θ_i and insert them into Eq. (2.3) to find the derivatives of the detailed system in a rotating frame. We then note that $\dot{\theta}_i(t) = \sum_{k=0}^{n} \dot{a}_k(t)v_k(i)$ and use the restriction operator $\Re(\dot{\boldsymbol{\theta}}) = \dot{\boldsymbol{a}}$, to get the derivatives of the coarse-grained coefficients. A flow diagram is given in Figure 4.1.

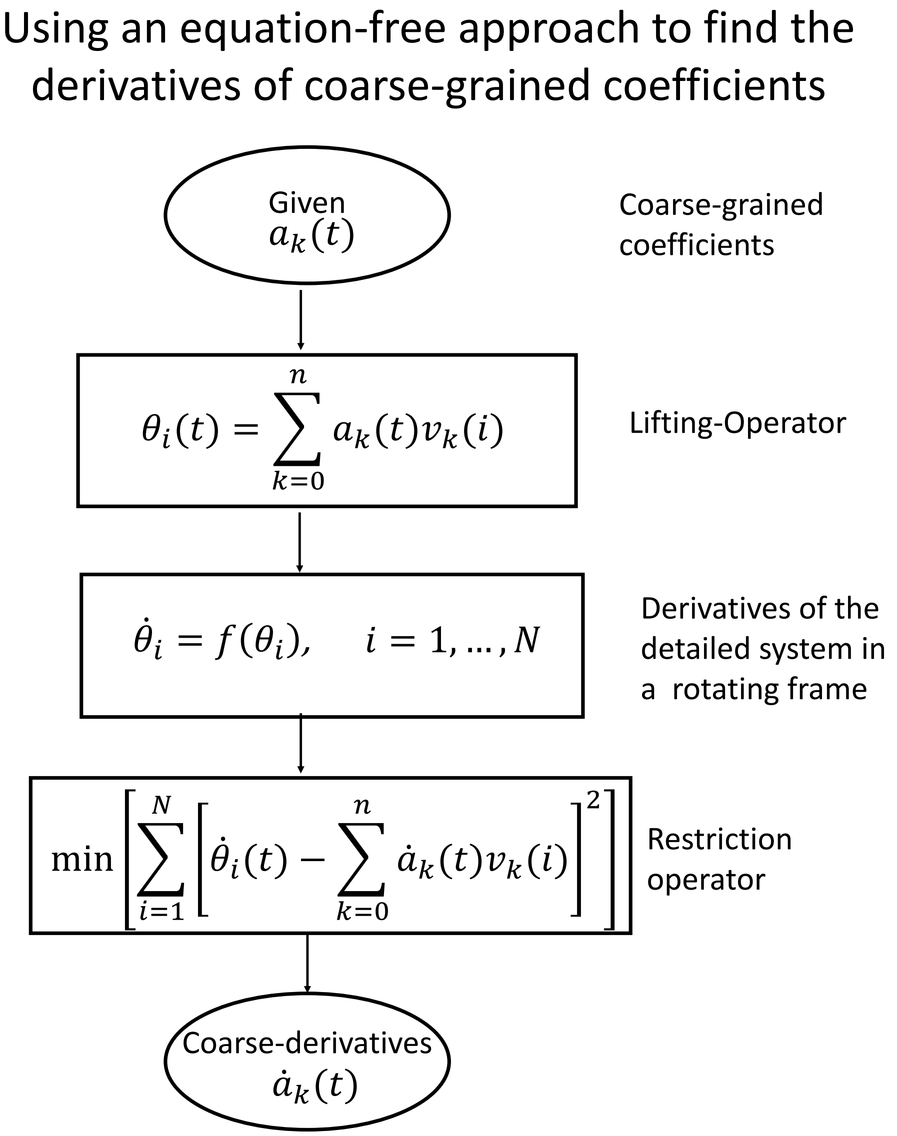

Figure 4.1 A flow diagram showing how to find the derivatives for the coarse-grained system for a given set of coarse-grained variables. Here, the spatial functions are defined as $v_k = (i-1)^k, k = 1, ..., n$.

4.2 Finding fixed points of the coarse-grained system

If the equations of the coarse-grained system were previously known, we would have been able to represent them as

$$\frac{d\boldsymbol{a}}{dt} = \boldsymbol{g}(\boldsymbol{a}, K) \tag{4.6}$$

Given the first guess $\boldsymbol{a}^{(1)}$, we can find the next guess $\boldsymbol{a}^{(j+1)}$ using the equation:

$$\boldsymbol{a}^{(j+1)} = \boldsymbol{a}^{(j)} - \boldsymbol{z} \tag{4.7}$$

$$\boldsymbol{z} = J^{-1}\boldsymbol{g}(\boldsymbol{a}^{(j)}) \tag{4.8}$$

where J is the Jacobian defined as

$$J = \begin{bmatrix} \frac{\partial g_1}{\partial a_1} & \frac{\partial g_1}{\partial a_2} & \cdots & \frac{\partial g_1}{\partial a_n} & \\ \frac{\partial g_2}{\partial a_1} & \frac{\partial g_2}{\partial a_2} & \cdots & \frac{\partial g_2}{\partial a_n} & \\ \vdots & \vdots & \vdots & \cdots & \vdots \\ \frac{\partial g_n}{\partial a_1} & \frac{\partial g_n}{\partial a_2} & \cdots & \frac{\partial g_n}{\partial a_n} & \end{bmatrix} \tag{4.9}$$

We perform the iterations until $\|\boldsymbol{g}(\boldsymbol{a},K)\| < \varepsilon$ ($\varepsilon = 10^{-10}$ in our simulations). Once we find the value of $\boldsymbol{a}$ for which $\|\boldsymbol{g}(\boldsymbol{a},K)\| < \varepsilon$ at some $K = K_0$, we apply the numerical continuation technique described in Chapter 2 (section 2.3) to create a bifurcation diagram for the coarse-grained system. This algorithm is summarized in Figure 4.2. The very first initial guess is calculated from a stable stationary solution of the detailed system. The difficulty with the algorithm described in Figure 4.2 is that the differential equations of the coarse-grained system are unknown. These can be found as described in Figure 4.1. Therefore, to approximate the Jacobian in Eq. (4.9), we use finite differences.

$$\frac{\partial g_i}{\partial a_k} = \frac{g_i(\boldsymbol{a} + \varepsilon e_k, K) - g_i(\boldsymbol{a}, K)}{\varepsilon}, \quad i = 1, ..., n \tag{4.10}$$

Here, e_k is a column unit vector having 1 at its k-th entry and 0s elsewhere. Recall that the rotating frame of the detailed system has a degree of freedom, which implies that the coarse-grained coefficients also have a degree of freedom. To remove this degree of freedom, we choose $\boldsymbol{a}$ such that $\theta_1 = 0$ (to be consistent with our choice in Chapter 2). For simplicity, we choose the spatial functions as $v_k = (i-1)^k$, $k = 1, \ldots, n$.

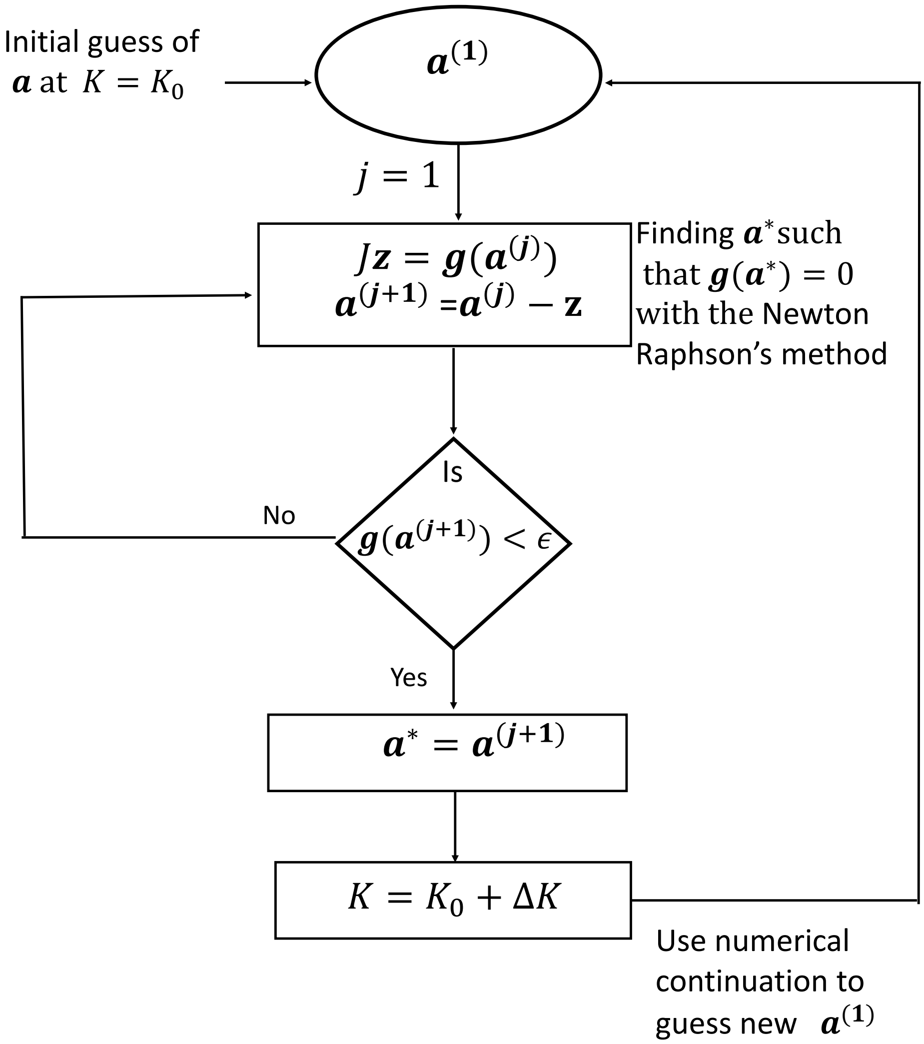

Figure 4.2 Schematic description of a numerical continuation technique for an unknown function g. Note that the function g is unknown and is estimated using the equation-free approach described in Figure 4.1.

4.3 Bifurcation Diagrams when θ_i are functions of their positions

We start with an example of twist-1 for $N = 100$ oscillators and $M = 5$ with randomly distributed frequencies, but instead of solving the full system (as we did in Chapter 2, Figure 2.8), we apply an equation-free approach as discussed in Figure 4.2 and Figure 4.1. We increase the number of coefficients from 2 to 4 in Figure 4.3. Note that we consider the spatial functions as $v_k = (i-1)^k, k = 1, ..., n$. The results of an equation-free approach are shown by dark pink color whereas the cyan color shows the results of the detailed system. We can observe that as the number of coefficients is increased, we get closer to the point of bifurcation of the detailed system, which is $K = 1.313$. Also, in the case of higher coefficients, the stable and unstable branches both converged to the detailed system's stable and unstable branches respectively.

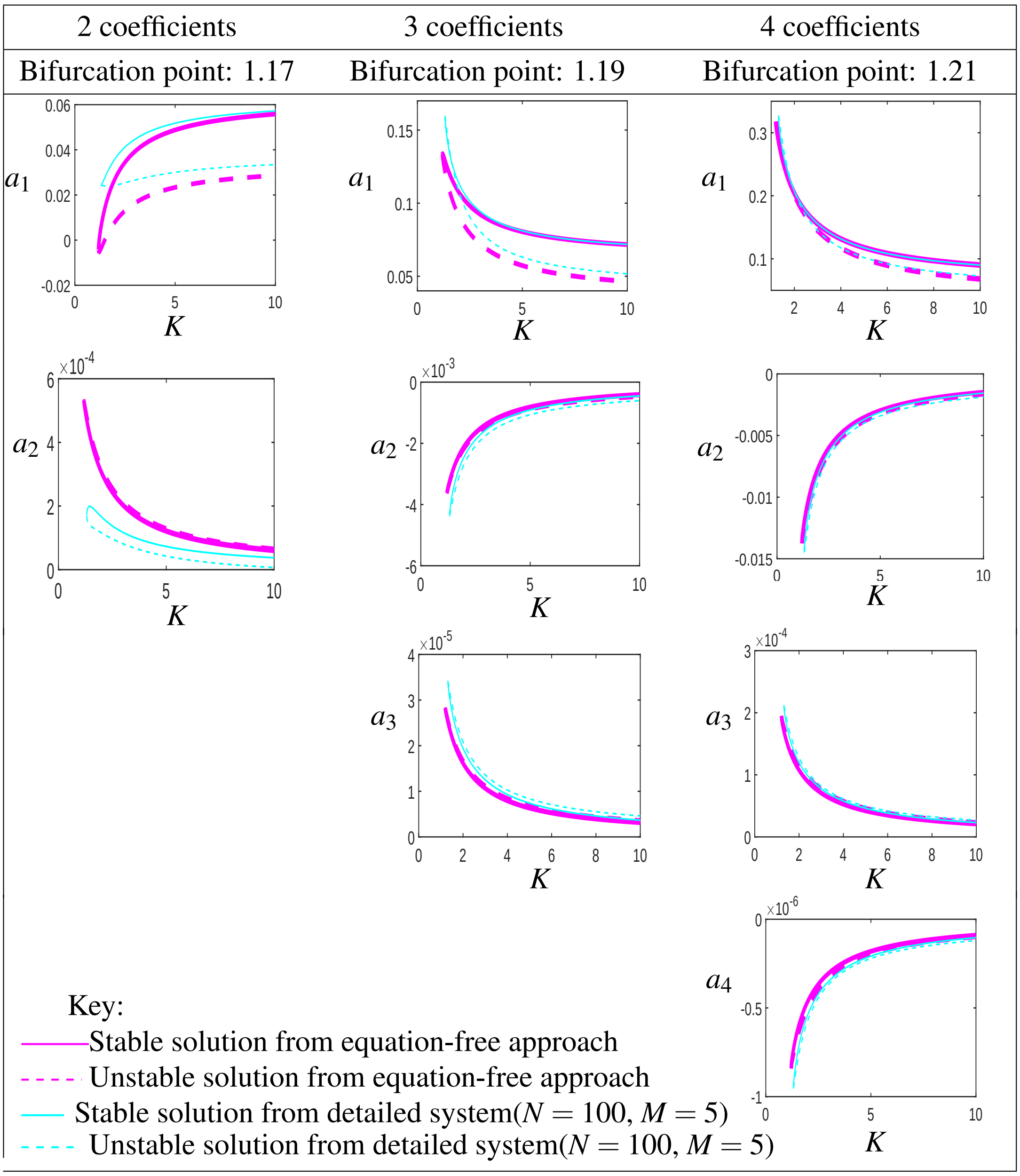

Figure 4.3 Comparison of the solutions of twist-1 equation-free approach (pink color) with the twist-1 detailed system (cyan color) for $N = 100$, $M = 5$ and randomly distributed frequencies between 0 and 1. The spatial functions are $v_1 = i - 1$, $v_2 = (i-1)^2, v_3 = (i-1)^3, v_4 = (i-1)^4$ where i is the oscillator number. The point of bifurcation for the detailed system is $K = 1.313$, whereas the point of bifurcation with an equation-free approach for 2, 3 and 4 coefficients are $K = 1.17$, $K = 1.19$ and $K = 1.21$ respectively. It can be seen that for four coefficients, the solution converges to both the stable and unstable branches.

In Figure 4.4, we show one of the solutions from Figure 4.3 along with the fitting at $K = 10$ of the stable and unstable solutions marked by $A1$ and $B1$ respectively. The blue circles represent the phase of the oscillators in a moving frame of the detailed system, and the red dots represent the estimated solution from the equation-free approach. Clearly, for both the stable and unstable branches, the fitting is good. Note that for the stable branch, the range of states of the oscillators is $[0,2\pi]$ while the range of the states of the unstable branch is $[0,\pi]$. This illustrates that the distinction between the different twists is not a clear cut.

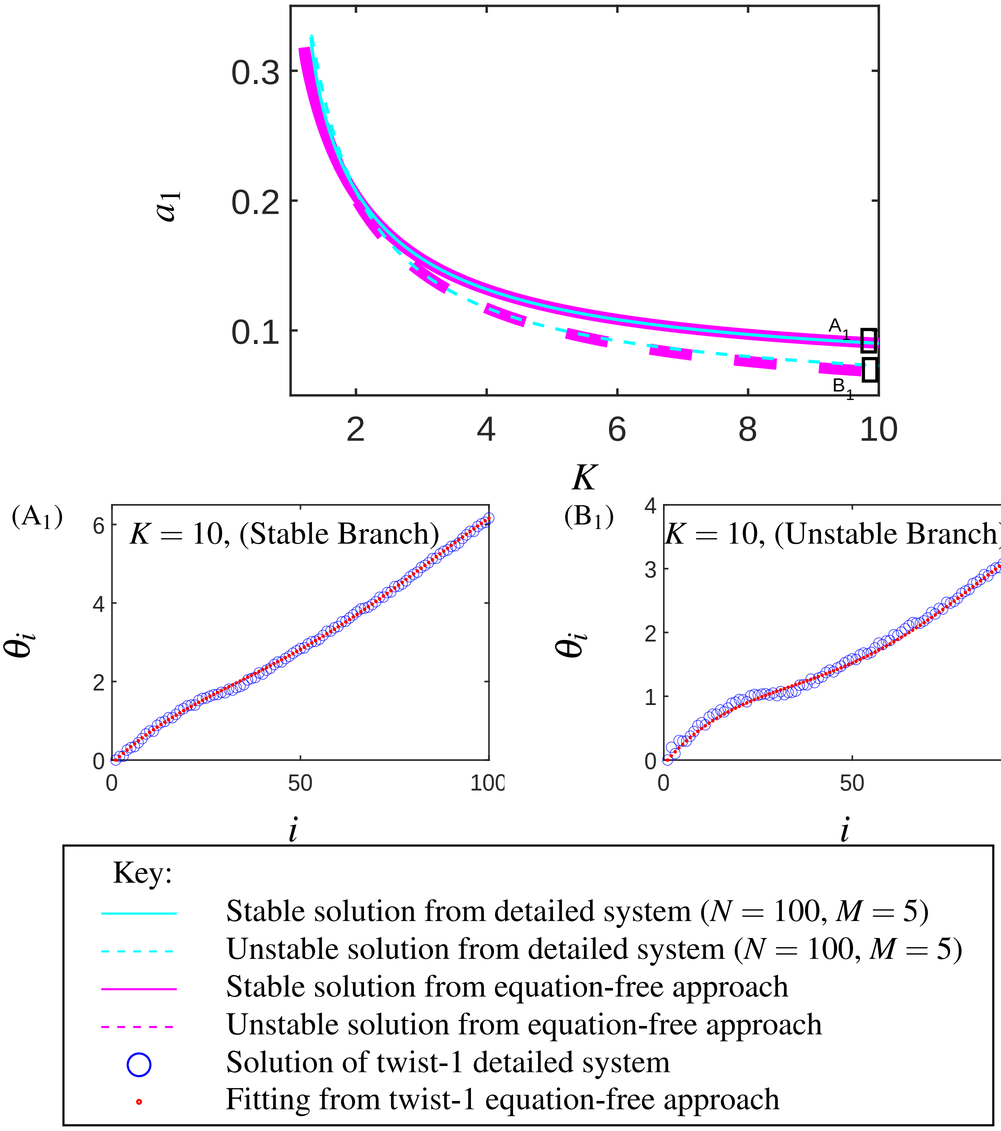

Figure 4.4 Comparison of the fitting of the stable and unstable branches for twist-1 at $K = 10$ (marked by A_1 and B_1) when the number of coefficients is 4.

Next, we show an example of twist-2. Again, we estimate our solution for $N = 100$ oscillators and $M = 5$. The angular frequencies are equally distributed within the interval $[0.3, 0.7]$. The point of bifurcation for the detailed system is $K = 2.09$, whereas the point of bifurcation with the 2, 3 and 4 coefficients is $K = 1.56$, $K = 1.74$ and $K = 1.76$ respectively. Figure 4.5 shows the comparison of the detailed system (turquoise color) with an equation-free approach (pink color).

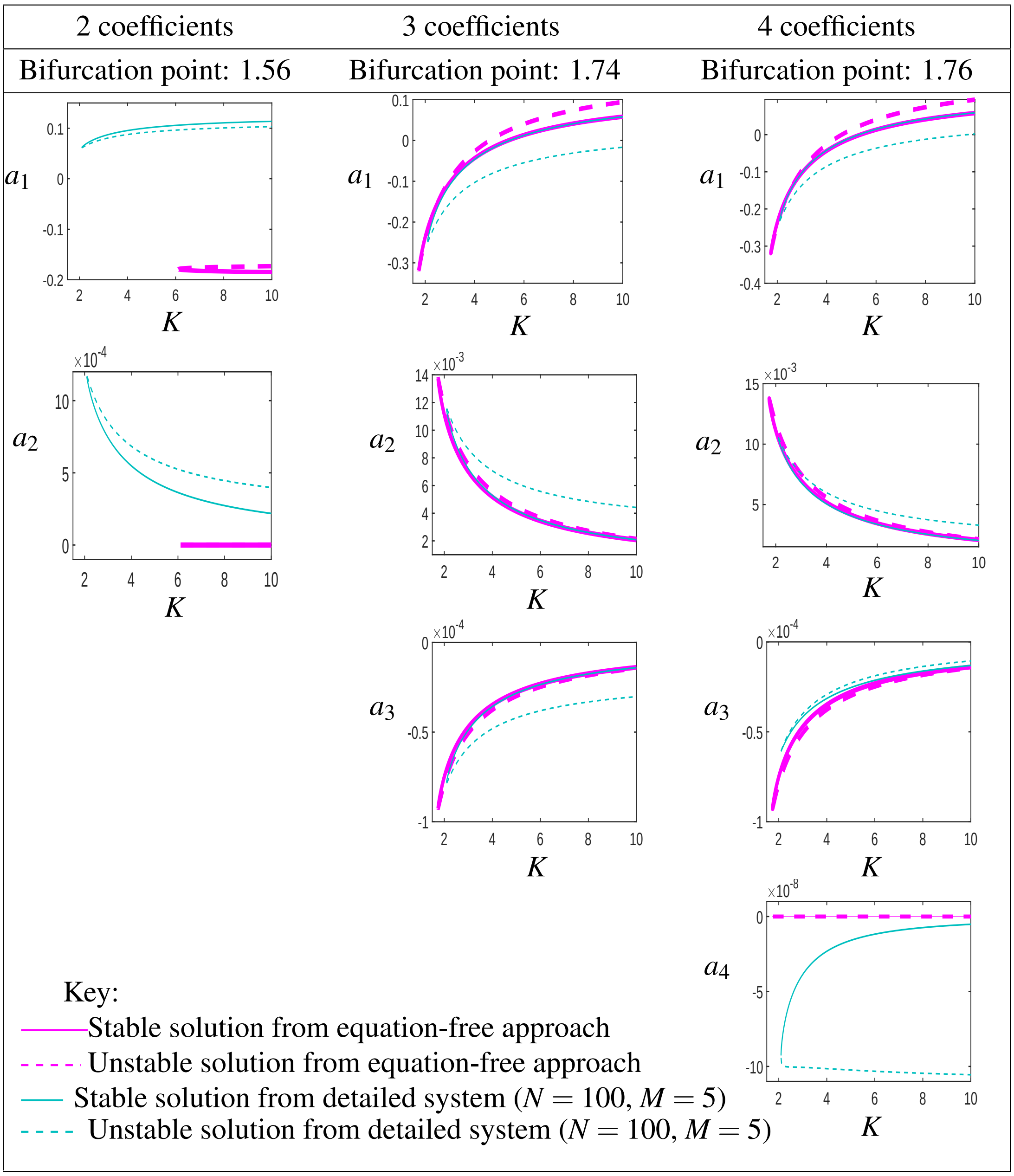

Figure 4.5 Comparison of the bifurcation diagrams of twist-2 obtained by the equation-free approach and the detailed system. The natural frequencies are equally distributed between 0.3 and 0.7. The spatial functions are $i-1$, $(i-1)^2, (i-1)^3, (i-1)^4$ where i is the oscillator number. The point of bifurcation for the detailed system is $K = 2.09$, whereas the point of bifurcation with an equation-free approach for 2, 3 and 4 coefficients is $K = 1.56$, $K = 1.74$ and $K = 1.76$ respectively.

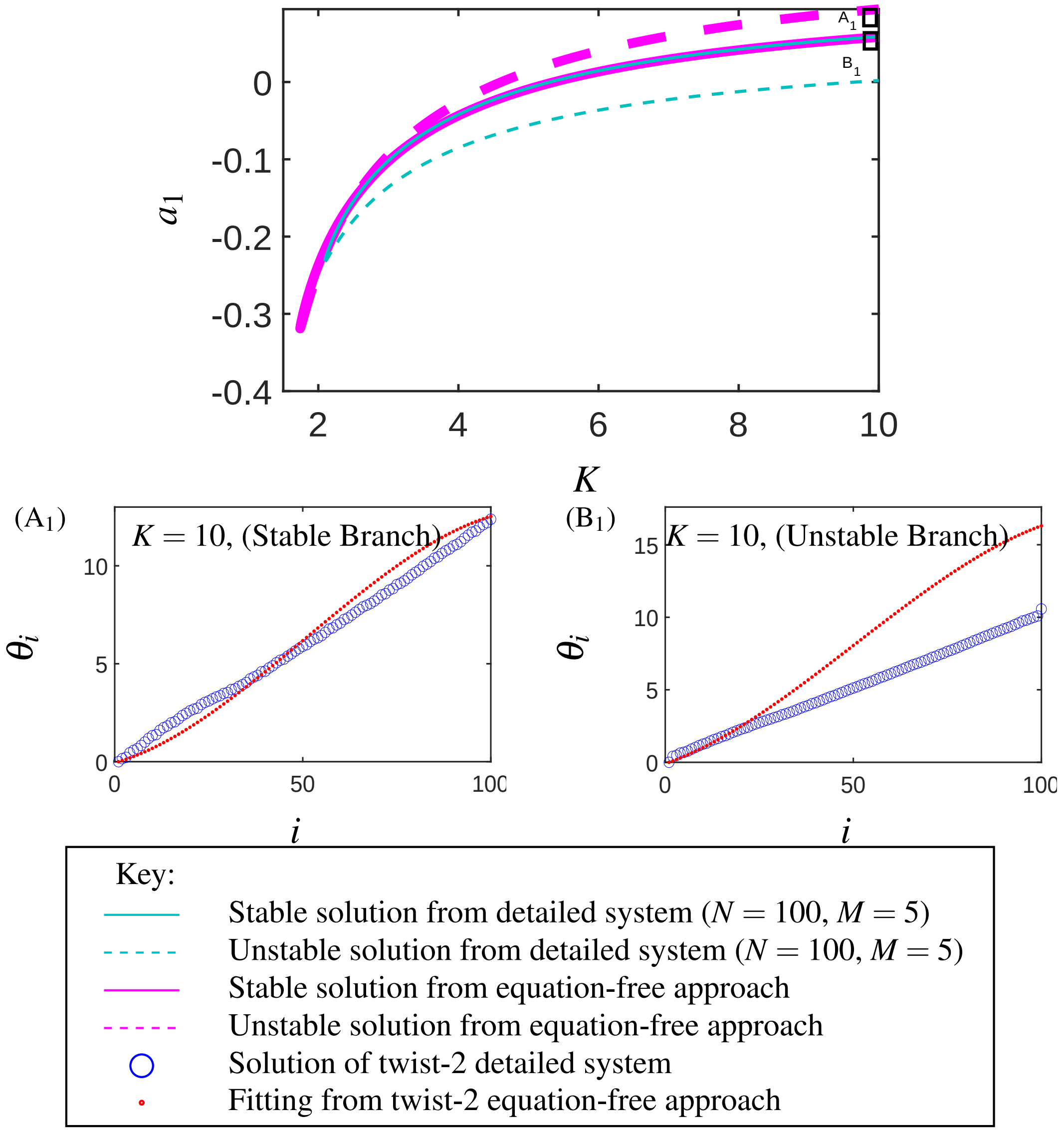

Figure 4.6 Comparison of the fitting of the stable and unstable branches for twist-2 at $K = 10$ (marked by A_1 and B_1) when the number of coefficients is 4.

We can observe in Figure 4.5 that for twist-2, the stable branch of the equation-free approach converges to the stable branch of the detailed system but the unstable branch does not. Moreover, the point of bifurcation for an equation-free approach is always ahead of the detailed system in all these cases. Additionally, our analysis of the fitting depicted in Figure 4.6, indicates that the stable branch adheres to twist-2 behavior, whereas the unstable branch does not. We will now investigate the possibility that the equation-free solution for the unstable branch follows other twists.

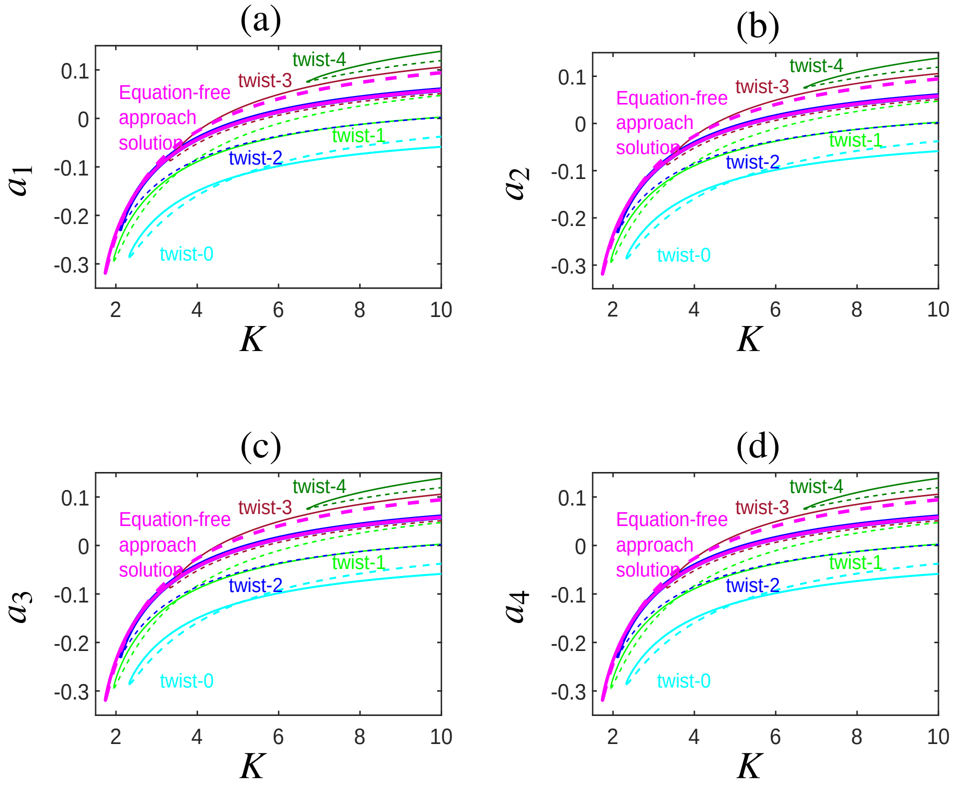

Figure 4.7 Bifurcation diagrams of twist-2 obtained by the equation-free approach (with four coefficients, pink line) and other twisted solutions of the detailed system with the frequencies equally distributed between 0.3 and 0.7. The spatial functions are $(i-1)$, $(i-1)^2$, $(i-1)^3$, $(i-1)^4$ where i is the oscillator number.

In Figure 4.7, we consider the case of 4 coefficients from Figure 4.5 and compare the solutions with several twisted states of the detailed system. As can be seen the solutions of all the twisted states are very close by. For a_1, the stable branch of twist-2 in both the detailed and coarse-grained systems are indistinguishable but the stable solution of the coarse-grained system continues towards twist-1 while the unstable branch then converges to the stable solution of twist-3. For a_2, the unstable branch of twist-2 obtained by the equation-free approach converges to the solution of twist-1. For a_3, it is in the middle of twist-3 and twist-1 while a_4 seems to converge to twist-3 but is negligible. The solution we see for twist-2 might capture an emergent property of the coarse-grained system.

Next, we look at the fitting for one of the solutions at $K = 10$ (marked by A_1). In Figure 4.8, we plot a solution of twist-3 obtained by the detailed system and compare it with the equation-free solution of twist-2. We can observe that the equation-free twist-2 solution is getting closer to detailed system twist-3.

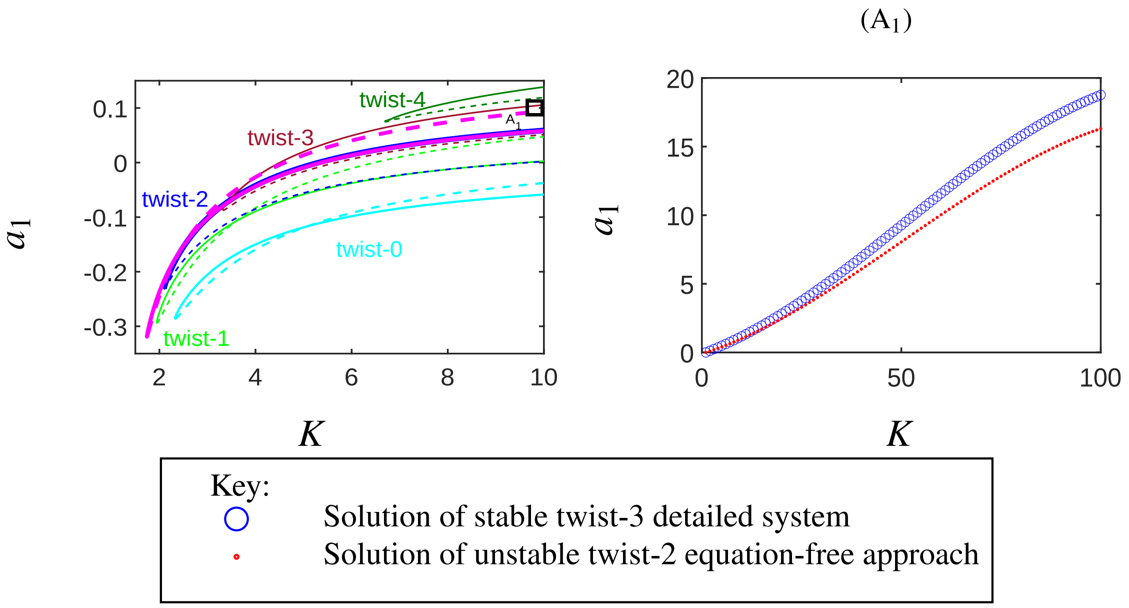

Figure 4.8 Comparison of the fitting of the stable and unstable branches at $K = 10$ (marked by A_1) for twist-2 when the number of coefficients is 4.

4.4 Bifurcation Diagrams when θ_i are functions of their angular frequencies

In this section, we return to the case where in a synchronized state, θ_i, become a function of their natural angular frequencies, ω_i, as we considered in Chapter 3. The algorithm for creating a bifurcation diagram in this case is similar to the algorithm we described in section 4.3 but with $v_k(i)$ replaced with $\phi_k(\omega_i)$. To remove the degree of freedom and for simplicity we choose the functions $\phi_k = \omega^k$ instead of the Legendre functions we used in Chapter 3. For convenience, we choose $\omega_1 = 0$ with $a_0 = 0$ and the other ω_i distributed *equally* between 0 and 1. Figure 4.9 shows the bifurcation diagrams of a spatially extended network with $N = 100$, $M = 5$.

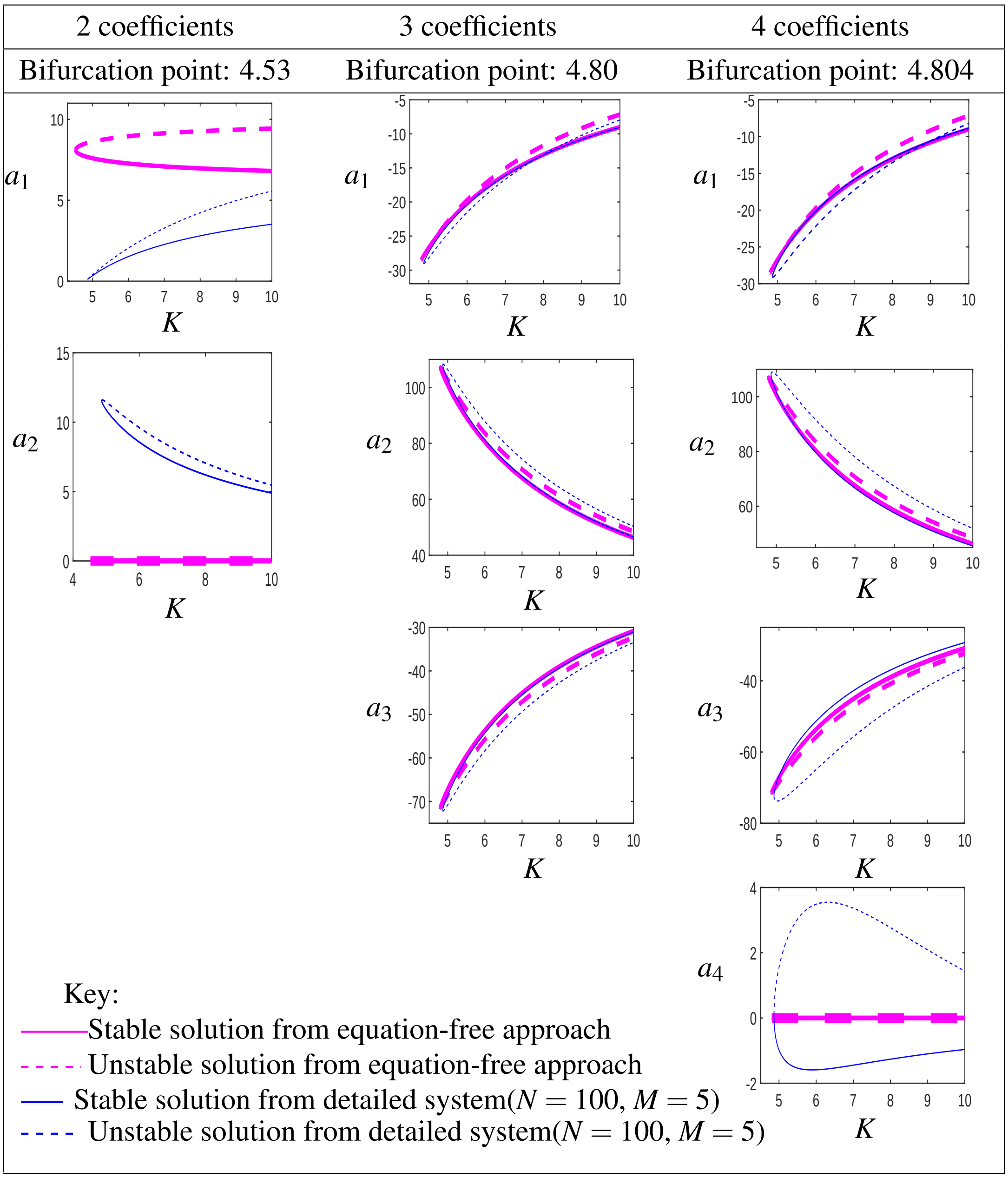

Figure 4.9 Comparison of the solutions of twist-1 equation-free approach (pink) with the twist-1 detailed system (blue) with equally distributed frequencies between 0 and 1. The functions are $\phi_k = (\omega)^k, k = 1, \ldots 4$, where ω is the angular frequencies of the oscillators. The actual point of bifurcation for the detailed system is $K = 4.865$

Here, in Figure 4.9, the solution of twist-1 equation-free approach is represented by the pink color, whereas the blue one represents the solution of twist-1 detailed system. The actual point of bifurcation for the detailed system is $K = 4.865$. We can observe from these figures that the stable branch of an equation-free approach converges to the stable solution of the detailed system but this is not the case for the unstable branch. This behaviour can be observed in Figure 4.10, where we see the fitting for the detailed system at $K = 10$. We can see that for the stable branch of twist-1 (marked by A_1), the fitting is good. However, this is not the case for the unstable branch (marked by B_1).

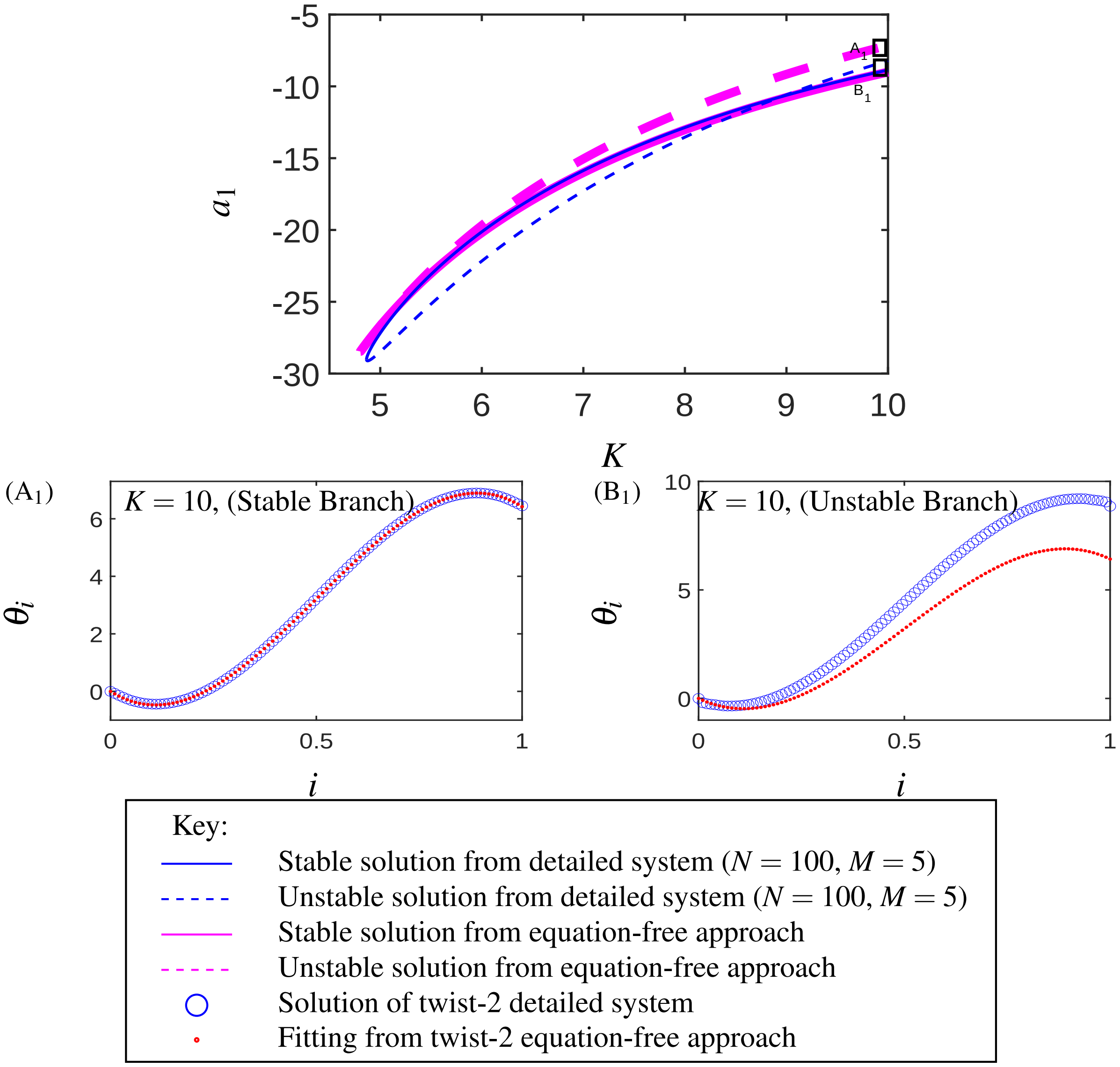

Figure 4.10 Comparison of the fitting of the stable and unstable branches at $K = 10$ for twist-1 when the number of coefficients is 4.

Now, we consider the case $N = 100$ and $M = 50$ which is the all-all Kuramoto model and form its bifurcation diagram. The bifurcation point for a detailed system is $K = 0.6431$. In Figure 4.11, we show the results for twist-0 with the detailed and equation-free approach. The blue line represents the solution from the detailed system whereas the bold pink line represents the solution from the equation-free approach with 3 and 4 coefficients. The point of bifurcations are $K = 0.62$, $K = 0.63$ and $K = 0.632$ from 2, 3 and 4 coefficients respectively.

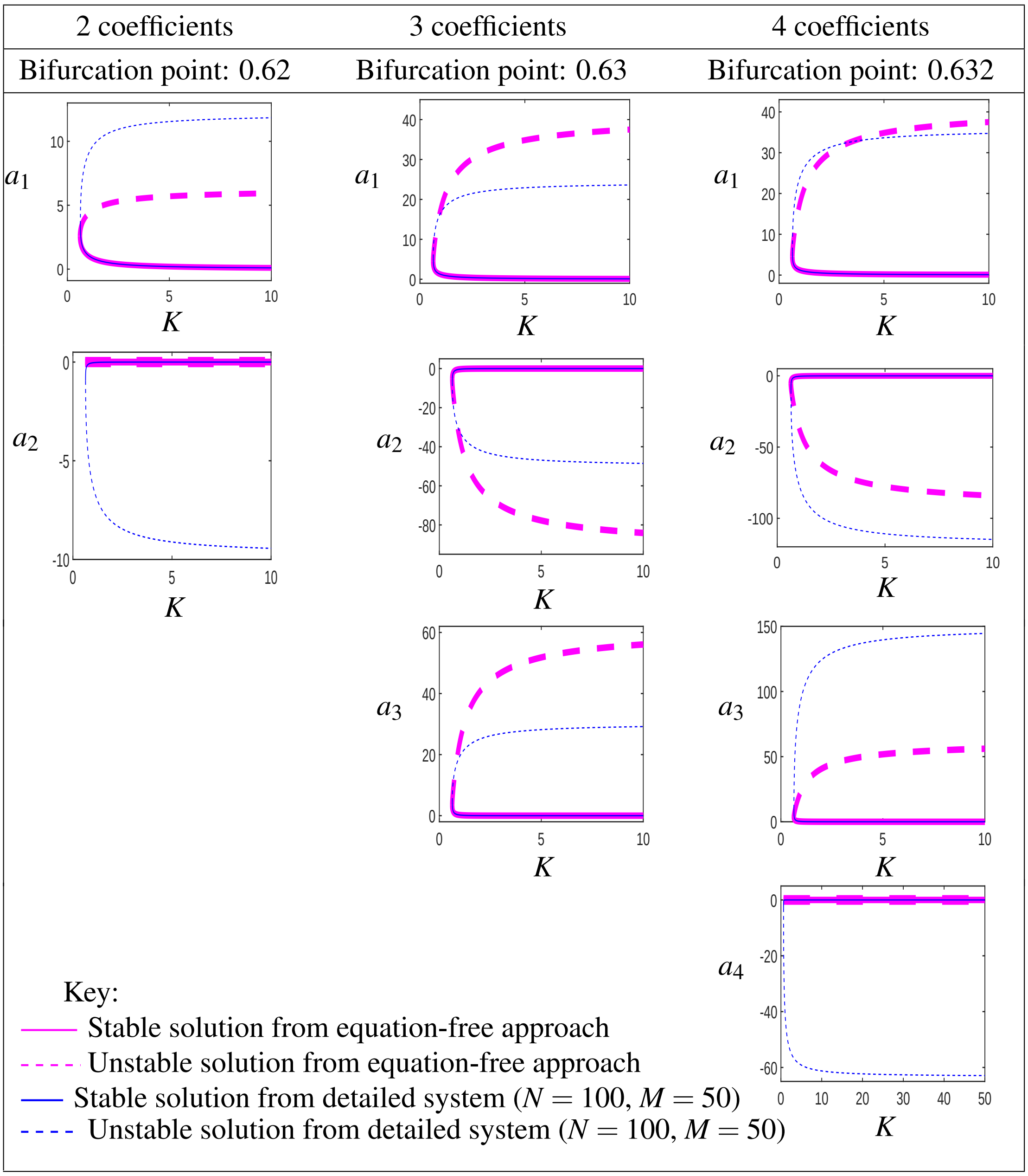

Figure 4.11 Comparison of the solutions of twist-0 equation-free approach (pink) with the twist-0 detailed system (blue) with the equally distributed frequencies between 0 and 1. The functions are $\phi_k = (\omega)^k, k = 1, \ldots, n$, where ω is the angular frequencies of the oscillators.

We can observe that in all the subfigures of Figure 4.11, the stable branches from the detailed system and the equation-free approach converge but this is not the case for the unstable branch. For the unstable branch, the equation-free solution of 3 and 4 coefficients converge to each other. This is shown in Figure 4.12, where we can see the overlapping solutions of 3 and 4 coefficients for a_1, a_2 and a_3.

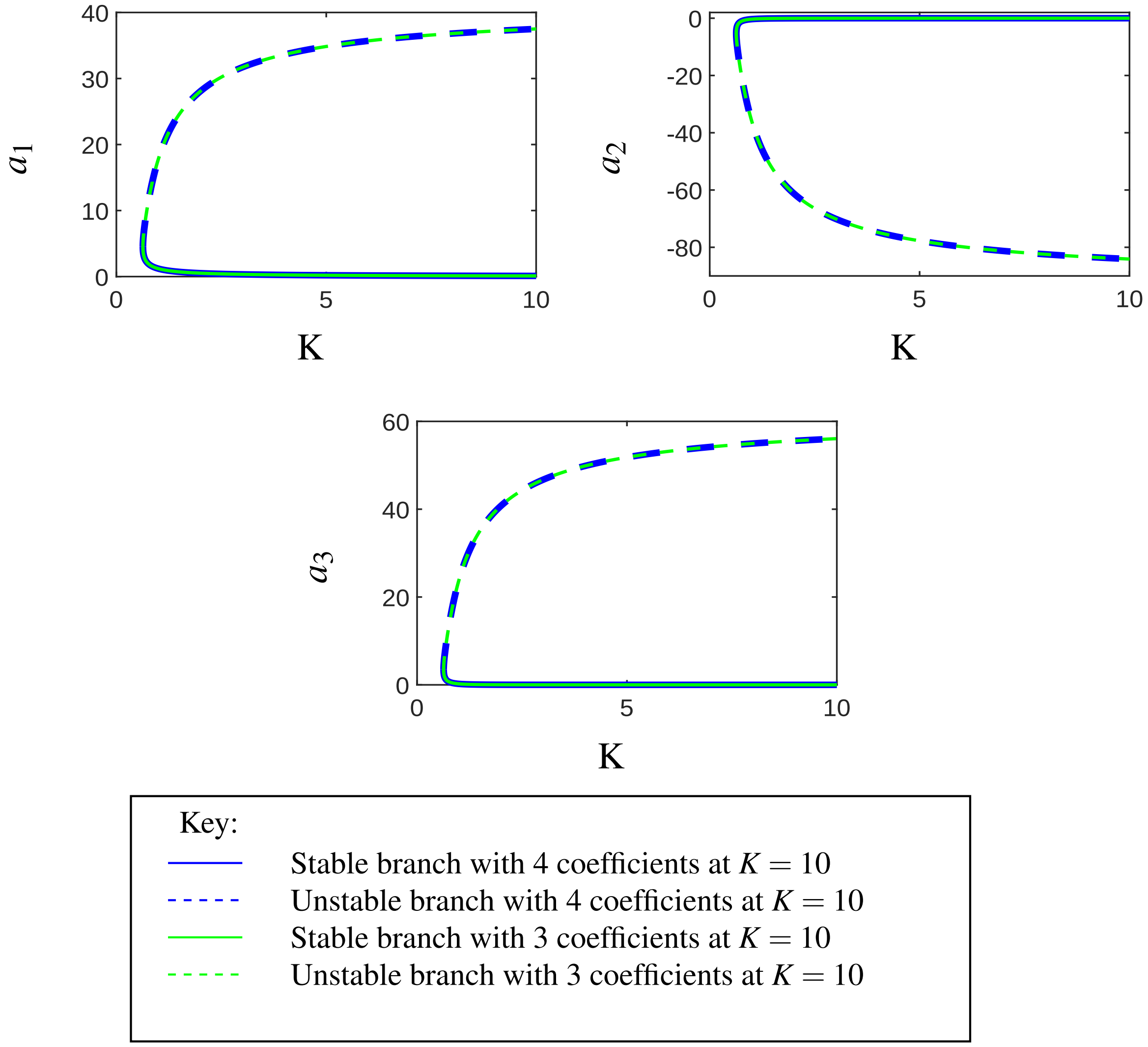

Figure 4.12 Overlapping solutions of 3 and 4 coefficients for a_1, a_2, a_3. The stable and unstable branch with 3 and 4 coefficients converges for a_1, a_2, a_3.

Now, we investigate the reason for why the unstable branch of the equation-free approach and the detailed system does not converge. By considering the same value $K = 10$, from the stable and unstable branch (marked by A_1 and B_1), we check the fitting for a detailed system. We can observe in Figure 4.13 that there exists an outlier in the all-all Kuramoto model. Because of this outlier, the unstable branches of the detailed and equation-free solutions do not converge.

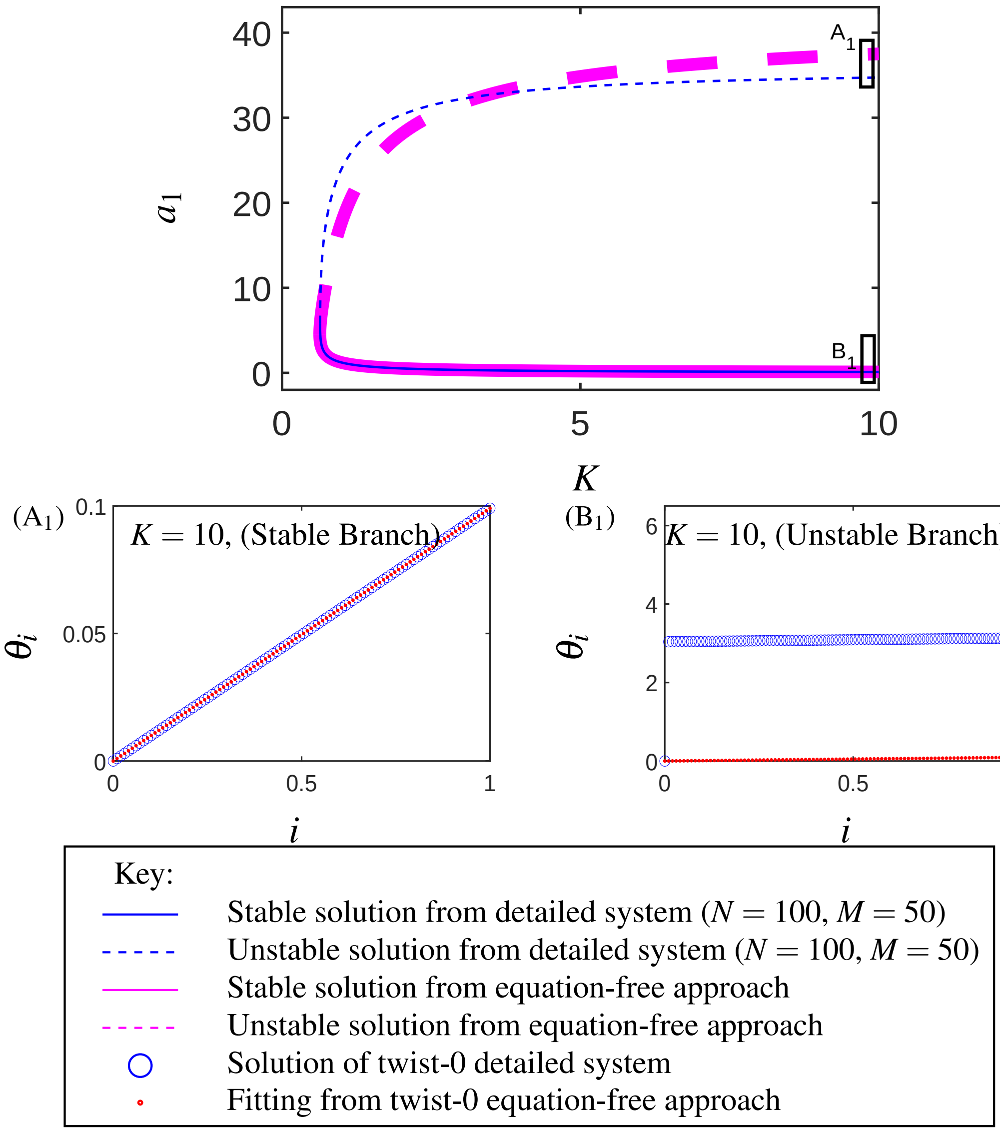

Figure 4.13 Relationship between the state of the oscillators and the their natural frequencies for the all-all Kuramoto model twist-0. Top figure shows the bifurcation diagram. (B_1) Unstable solution at $K = 10$. (A_1) Stable solution at $K = 10$. The blue circles represent the oscillators in a detailed system (Eq. (2.1)), and the red dots represent the estimated solution from the equation-free approach.

4.5 Discussion and Conclusions

In this chapter, we explained the methodology of applying an equation-free approach along with the numerical continuation technique to form bifurcation diagrams. We used two representations for θ_i and discussed both the spatially extended network and all-all Kuramoto model. We considered an example (see Figure 4.3, and Figure 4.9) where the equation-free solution captures the behaviour of the detailed system well. And some other examples where it failed to do so (see Figure 4.5). We have also seen the emergent behaviour of the coarse grained system where the solution of one of the twisted state follows the solution of other twisted states. Lastly, we also observed that in the all-all Kuramoto model, the stable branch from the equation-free approach and the detailed system converge but the unstable branch does not due to the existence of an outlier.

Chapter 5

Creating Bifurcation Diagrams Using the Equation-Free Approach in Two Dimensions

In this chapter we attempt to improve the results of the previous chapter by considering the equation-free approach in two dimensions using two summations. We first motivate our approach with an example. We then explain the approach and show some examples with $M = 5$ and $M = 10$ for different twisted solutions.

5.1 Bifurcation Diagrams when θ_i are functions of both positions and angular frequencies.

Consider the example of twist-1 from Chapter 4 (section 4.3) when $N = 100$, $M = 5$ and the number of coefficients are 3 and 4 with the spatial function $v_k = (i-1)^k$. We already observed in Figure 4.4 that for the given example the fitting is good at $K = 10$ for both the stable and unstable branches. Figure 5.1 shows the fitting at $K = 2$. The solution of the detailed system is depicted by a blue circle, whilst the green and red curved lines indicate the fitting from the twist-1 equation-free approach with 3 and 4 coefficients of the spatial function $v_k = (i-1)^k$ respectively. We can see that increasing the number of spatial coefficients enhances the shape of the fitting. However, it is evident that there is a width to the solution of the detailed system indicating that we need an additional summation.

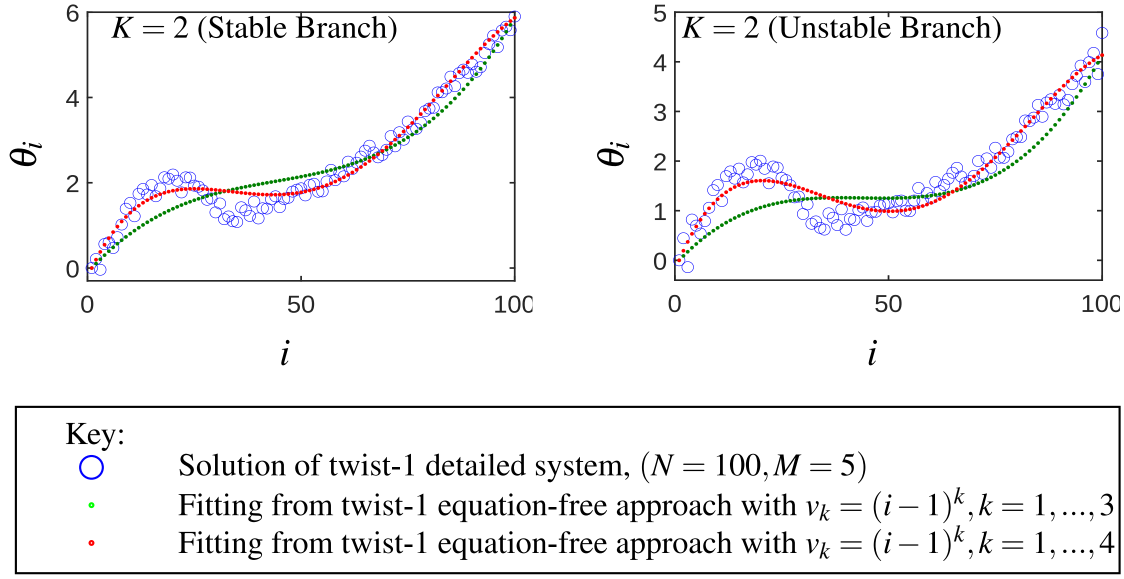

Figure 5.1 Comparison of the fitting of the stable and unstable branches at $K = 2$ for twist-1 when the number of coefficients are 3 and 4 with spatial function $v_k = (i-1)^k$.

We therefore treat θ_i as a function of both the angular frequencies, ω_i, and its position, i. Thus, we can express θ_i as follows:

$$\theta_i(t) = \sum_{k=0}^{n} \sum_{j=0}^{m} a_{kj}(t) v_k(i) \phi_j(\omega_i), \qquad i = 1, \ldots, N \tag{5.1}$$

where, a_{kj} are the time dependent coarse grained coefficients, v_k are the n spatial functions, ϕ_j are the m functions depending on the natural angular frequencies, ω_i, where i is the position of the oscillators and N is the total number of oscillators. To reduce the degree of freedom, we consider v_k as $v_k = (i-1)^k, k = 0, ..., n$ and $\phi_j = \omega^j$ with $a_{00} = 0$.

To find the solutions with an equation-free approach, we consider Equation 5.1 as our lifting operator whereas the restricting operator is defined as:

$$min \left[\theta_i(t) - \sum_{k=0}^{n} \sum_{j=0}^{m} a_{kj}(t) v_k(i) \phi_j(\omega_i) \right]^2, \qquad i = 1 \ldots N \tag{5.2}$$

To create bifurcation diagrams using an equation-free approach, we follow the same algorithm outlined in section 4.2, with the lifting and restricting operators provided in Equation 5.1 and Equation 5.2.

We begin by taking into consideration the same example from Chapter 4 that we previously discussed and solving it using an equation-free approach involving two summations. Equation 5.2 shows the system of $N = 100$, $M = 5$ with randomly distributed frequencies between 0 and 1. We find the solutions using a total of 8 coefficients, ($\phi_j = \omega^j, j = 1,2$ and $v_k = (i-1)^k, k = 1,...,4$). In Figure 5.2, the results of an equation-free approach involving two summations are displayed in pink, whereas those of the detailed system are presented in turquoise color. Furthermore, as we move away from the bifurcation point, the stable and unstable branches of the equation-free approach appear to converge to the stable and unstable branches of the detailed system, respectively.

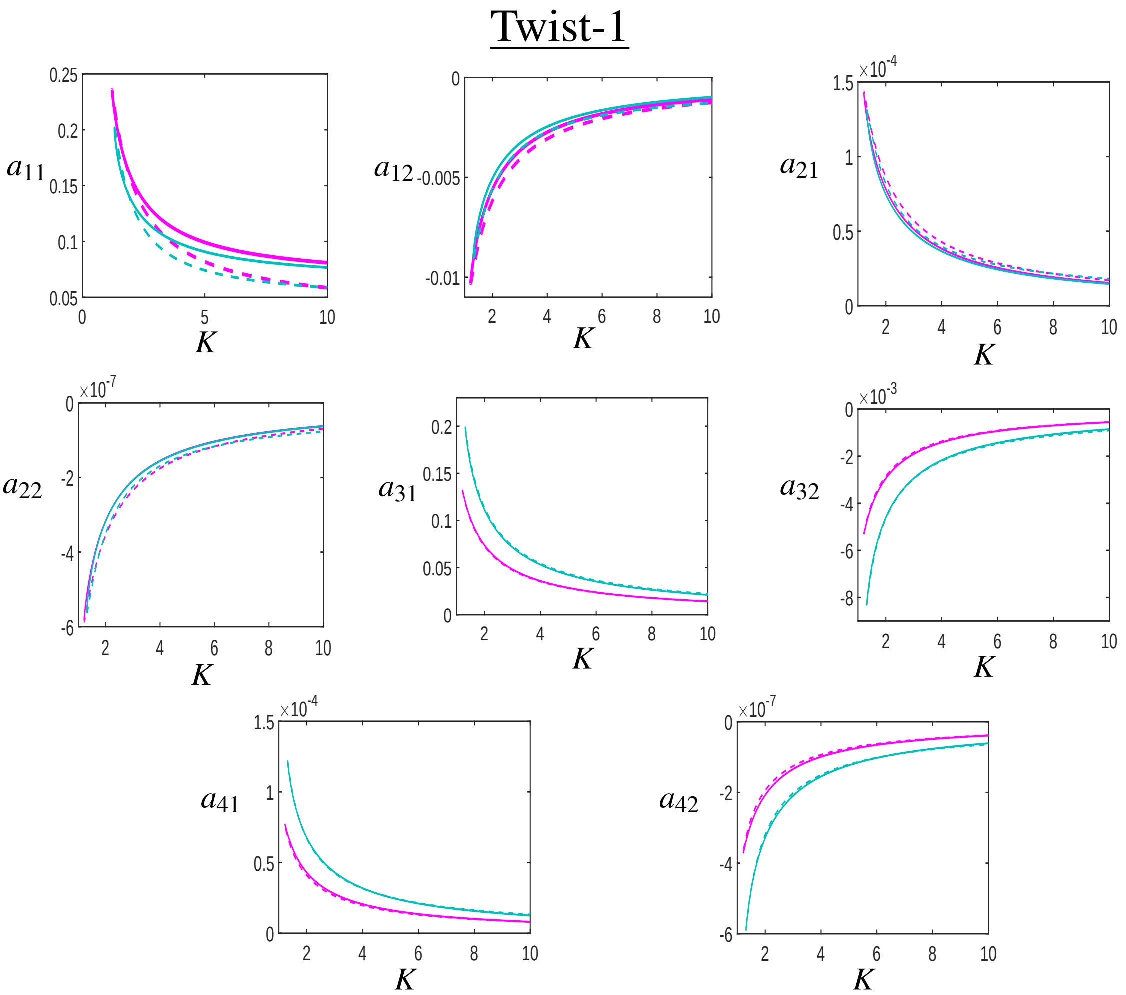

Key:

—— Stable solution of twist-1 detailed system ($N = 100$, $M = 5$)
- - - Unstable solution of twist-1 detailed system ($N = 100$, $M = 5$)
—— Stable solution from equation-free approach with combinations of 8 coefficients
- - - Unstable solution from equation-free approach with combinations of 8 coefficients

Figure 5.2 Comparison of the solutions of twist-1 equation-free approach (pink color) using two-summation with the twist-1 solution of the detailed system (turquoise color) for $N = 100$, $M = 5$ and randomly distributed frequencies between 0 and 1. The spatial functions are $v_k = (i-1)^k, k = 1, \ldots, 4$ where i is the oscillator number and $\phi_j = \omega^j, j = 1, 2$. The detailed system's bifurcation point is $K = 1.313$, whereas the bifurcation point with an equation-free approach for 8 coefficients is $K = 1.217$. It can be observed that for eight coefficients, the solution converges to both the stable and unstable branches of the detailed system when K gets larger.

Next, we consider the fitting at $K = 2$ for both the stable and unstable solutions (see Figure 5.3). The red dots show the estimated solution from the equation-free approach using two summations, and the blue circles represent the phase of the oscillators of the detailed system. The two-dimensional (using two-summations) fitting for which θ_i is a projection of both ω_i and i is presented in panels A1 and B1. Additionally, panels A2 and A3 show projections of θ_i as a function of i and θ_i as a function of ω_i for the stable branch respectively. Similarly, panels B2 and B3 show projections for the unstable branch of θ_i as a function of i and θ_i as a function of ω_i respectively. It is evident that by adding another function, the shape and width of the fitting improved for both the stable and unstable branches at $K = 2$.

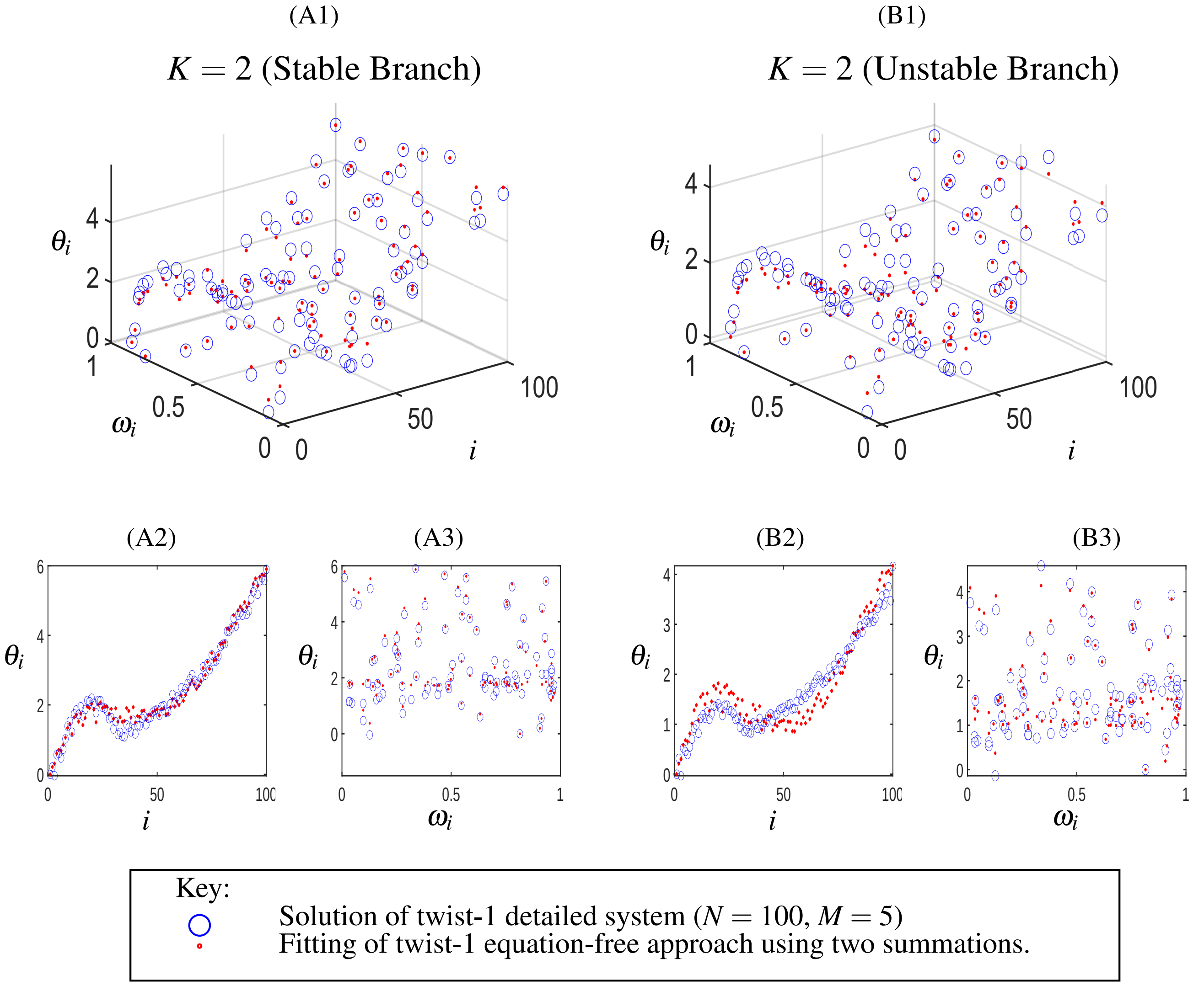

Figure 5.3 Comparison of the two-dimensional (using two summations) fitting of the stable and unstable solutions at $K = 2$ for twist-1 when there are 8 combinations of coefficients, i.e. $v_k = (i-1)^k, k = 1,\ldots,4$ and $\phi_j = \omega^j, j = 1,2$.

To examine the effects of changing the coefficients, we consider different combinations of v_k and ϕ_j with varying values of n and m. We start by fixing n at 3 and let the index k vary from 0 to this value. We also increase m from 1 to 3, obtaining 3, 6, and 9 coefficients. It's worth noting that when $a_{00}(t) = 0$, the coefficient with index 0 is not included, resulting in 2, 5, and 8 nonzero coefficients, respectively. Next, we fix n at 4 and again let the index k vary from 0 to 4. We then increase m from 1 to 2, obtaining 4 and 8 coefficients. In this case, if $a_{00}(t) = 0$, the coefficient with index 0 is not required, resulting in 3 and 7 nonzero coefficients, respectively. The bifurcation diagram of the first coefficient, a_{11} for the different number of coefficients, is shown in the Figure 5.4. The pink line depicts the solution of the two summations equation-free approach whereas the other coloured lines show the solution of detailed system. We evaluate the bifurcation point for each of these coefficient combinations and find that increasing the number of coefficients brings us closer to the actual bifurcation point of the detailed system, $(K = 1.313)$, albeit not uniformly.

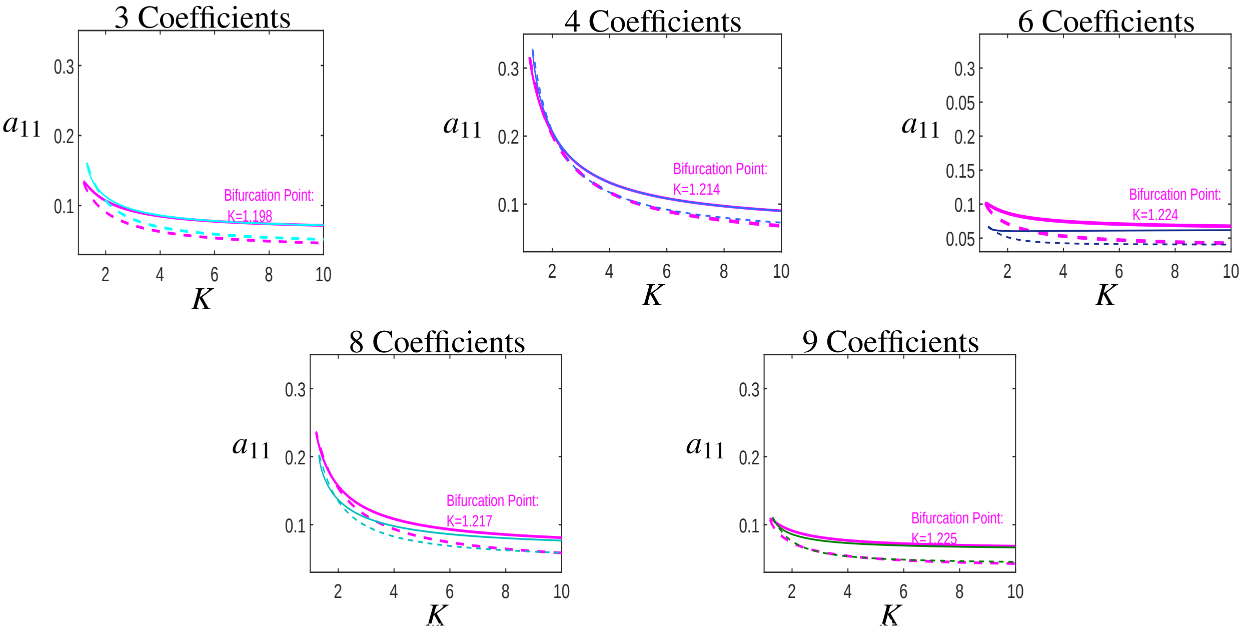
3 Coefficients

4 Coefficients

6 Coefficients

8 Coefficients

9 Coefficients

Figure 5.4 Bifurcation diagrams for a_{11} of twist-1, $N = 100$, $M = 5$ with various coefficients. The results show that the bifurcation point of an equation-free approach gets closer to the bifurcation point of the detailed system albeit not uniformly, and the stable and unstable branches from the equation-free approach and detailed system become indistinguishable as we move away from the bifurcation point.

Next, we compare the errors at two points on the stable and unstable branches (one closer to the bifurcation point, $K = 2$, and one further away from the bifurcation point, $K = 10$). For both the points from the stable and unstable branch of the bifurcation diagrams shown in Figure 5.4, we evaluate the absolute error differences between the detailed solution (represented as $a_{11,ds}$) and the equation-free solution (represented as $a_{11,Ef}$) and summarized the results in Table 5.1. Further, we also calculated L_2-norm at the same points (see Table 5.2) as the error differences calculated from the bifurcation diagram (given in Table 5.1) is not related to the goodness of fitting. The results show that as the number of coefficients increases, the estimated solution appears to converge to the true solution, though not uniformly.

Coefficient Numbers	$\lvert a_{11,Ef} - a_{11,ds}\rvert$ **at** $K = 10$ **(Stable Branch)**	$\lvert a_{11,Ef} - a_{11,ds}\rvert$ **at** $K = 10$ **(Unstable Branch)**	$\lvert a_{11,Ef} - a_{11,ds}\rvert$ **at** $K = 2$ **(Stable Branch)**	$\lvert a_{11,Ef} - a_{11,ds}\rvert$ **at** $K = 2$ **(Unstable Branch)**
3	0.0001	0.0052	0.0061	0.0149
4	0.0001	0.0048	0.0037	0.0061
6	0.0059	0.0019	0.0264	0.0197
8	0.0042	0.0001	0.0200	0.0191
9	0.0018	0.0024	0.0051	0.0021

Table 5.1 The absolute error differences at several points from the stable and unstable branches of bifurcation diagrams with various coefficients.

Coefficient Numbers	L_2 **norm of fitting at** $K = 10$ **(Stable Branch)**	L_2 **norm of fitting at** $K = 10$ **(Unstable Branch)**	L_2 **norm of fitting at** $K = 2$ **(Stable Branch)**	L_2 **norm of fitting at** $K = 2$ **(Unstable Branch)**
3	0.82	1.09	4.19	4.72
4	0.51	0.64	2.56	2.62
6	0.69	0.98	3.52	4.30
8	0.37	0.56	1.91	3.14
9	0.69	0.97	3.49	4.06

Table 5.2 The L_2-norm fitting at several points from the stable and unstable branches of bifurcation diagrams with various coefficients.

5.2 The equation-free approach with two summations for other twisted solutions

Figures 5.6, 5.7 and 5.8 show solutions of twist-2, twist-3, and twist-4 respectively. The pink color represents the equation free approach solution, whereas the navy blue, dark blue and green colour represent the twist-2, twist-3 and twist-4 solutions in the detailed system respectively. We once again compare the L_2 norm and the error differences between the equation-free approximation and the detailed system at two points. The Table 5.3 presents the differences between the bifurcation points calculated from the detailed system and the equation-free approach. Further, Table 5.4 calculates the error differences between the actual bifurcation point calculated from the detailed system and the equation-free approximated bifurcation point for various twisted states.The results show that the error difference between the true bifurcation point and the approximated bifurcation point increases as the number of twists increases.

In Table 5.5, we observe that when we choose a point away from the bifurcation point, ($K = 10$), the value of L_2-norm at the stable branch is lowest for twist-2 and highest for twist-1. On the unstable branch of the same point, twist-1 has a small L_2-norm value but twist-4 has a significantly large L_2-norm. Since twist-4 has a bifurcation point $K = 5.313$, we pick $K = 6$ as the second point nearer the bifurcation point to ensure that this point occurs for all twisted states. While the value for L_2-norm for twist-3 is largest and is least for twist-1 unstable branch at $K = 6$, the L_2-norm increases continuously from twist-1 to twist-4 for the stable branch of the same point.

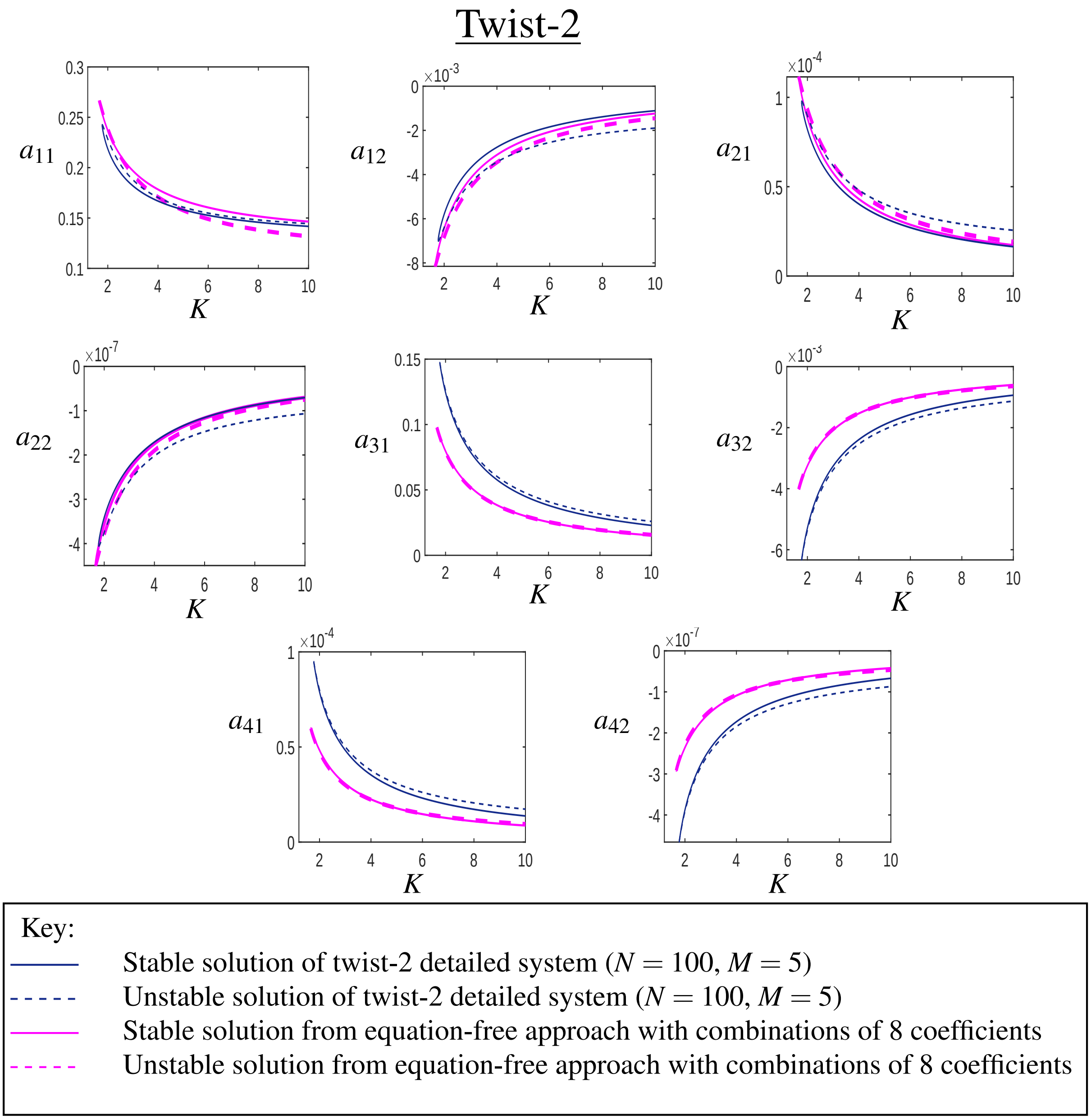

Figure 5.5 Comparison of the solutions of twist-2 equation-free approach (pink color) using two summations with the twist-2 detailed system (dark blue color) for $N = 100, M = 5$. The spatial functions are $v_k = (i-1)^k, k = 1, \ldots, 4$ where i is the oscillator number and $\phi_j = \omega^j, j = 1, 2$ with ω_j are randomly distributed frequencies between 0 and 1. The bifurcation point for the detailed system is $K = 1.663$, whereas the bifurcation point with an equation-free approach for 8 coefficients is $K = 1.775$.

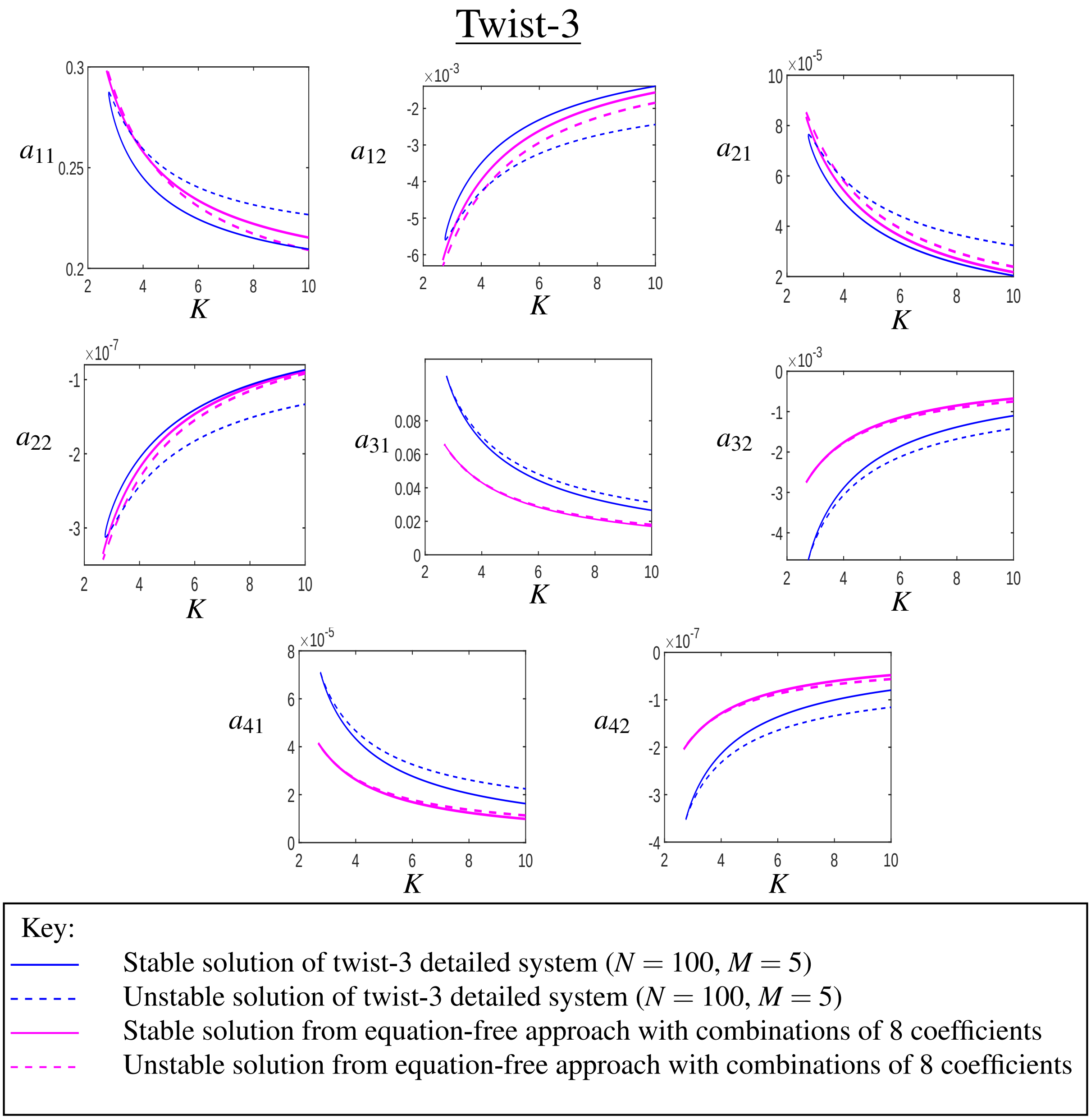

Figure 5.6 Comparison of the solutions of twist-3 equation-free approach (pink color) using two summations with the twist-3 detailed system (dark blue color) for $N = 100, M = 5$. The spatial functions are $v_k = (i-1)^k, k = 1,\ldots,4$ where i is the oscillator number and $\phi_j = \omega^j, j = 1,2$ with ω_j are randomly distributed frequencies between 0 and 1. The bifurcation point for the detailed system is $K = 2.7542$, whereas the bifurcation point with an equation-free approach for 8 coefficients is $K = 2.606$.

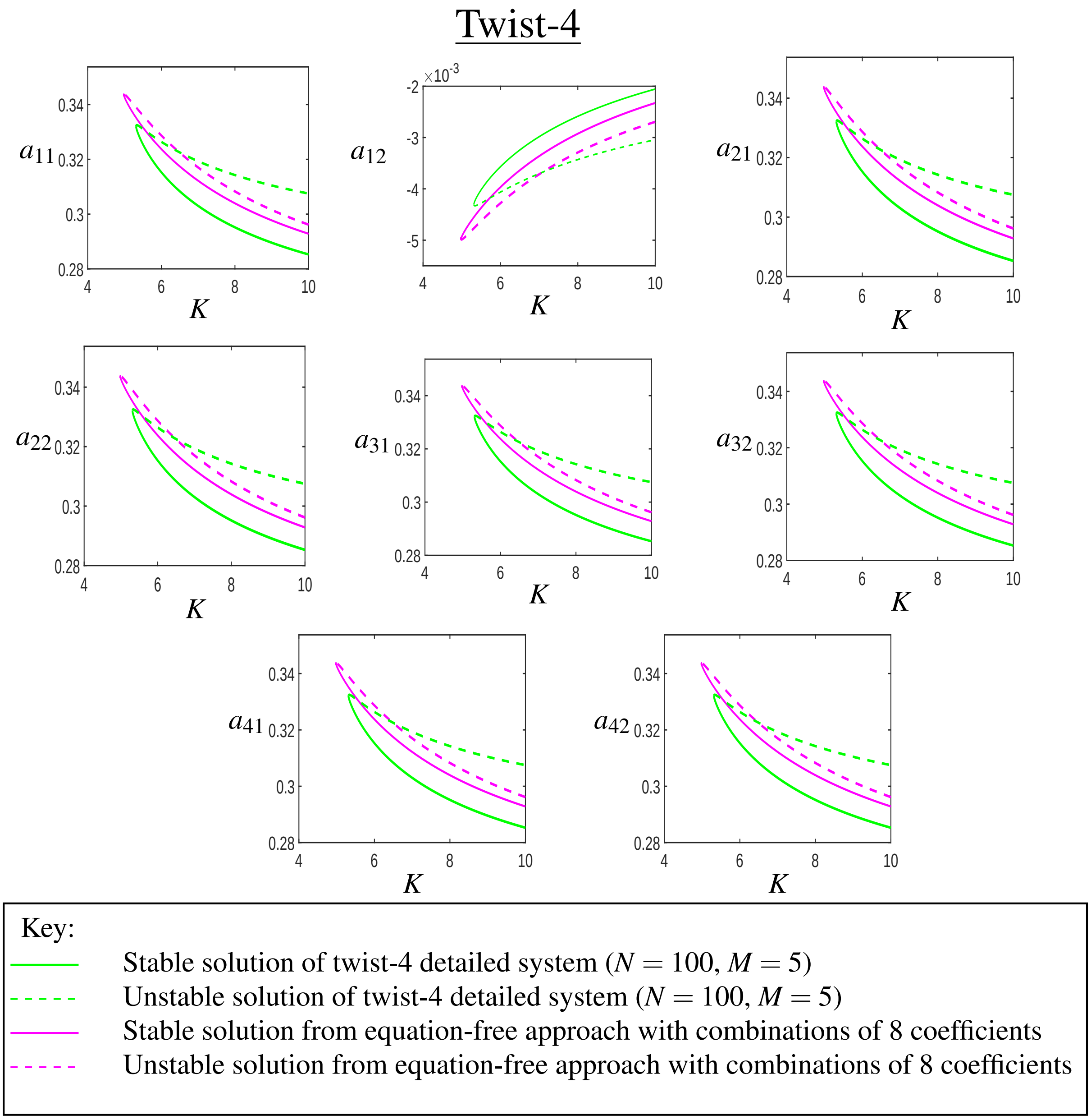

Figure 5.7 Comparison of the solutions of twist-4 equation-free approach (pink color) using two summations with the twist-4 detailed system (green color) for $N = 100, M = 5$. The spatial functions are $v_k = (i-1)^k, k = 1,\ldots,4$ where i is the oscillator number and $\phi_j = \omega^j, j = 1,2$ with ω_j are randomly distributed frequencies between 0 and 1. The bifurcation point for the detailed system is $K = 5.313$, whereas the bifurcation point with an equation-free approach for 8 coefficients is $K = 4.982$.

Number of Twists	**Bifurcation Point (Detailed System)**	**Bifurcation Point (Equation-free approach)**	**Differences between bifurcation points**
1	1.313	1.217	0.096
2	1.775	1.663	0.112
3	2.754	2.606	0.148
4	5.313	4.982	0.331

Table 5.3 Comparison of bifurcation points for various twisted states.

Number of Twists	$\lvert a_{11,Ef} - a_{11,ds}\rvert$ **at** $K = 10$ **(Stable Branch)**	$\lvert a_{11,Ef} - a_{11,ds}\rvert$ **at** $K = 10$ **(Unstable Branch)**	$\lvert a_{11,Ef} - a_{11,ds}\rvert$ **at** $K = 6$ **(Stable Branch)**	$\lvert a_{11,Ef} - a_{11,ds}\rvert$ **at** $K = 6$ **(Unstable Branch)**
1	0.0042	0.0002	0.0070	0.0052
2	0.0048	0.0126	0.0077	0.0058
3	0.0058	0.0171	0.0093	0.0095
4	0.0076	0.0113	0.0085	0.0022

Table 5.4 Error differences between true solution and approximated solution for various twisted states.

Number of Twists	L_2 **norm of fitting at** $K = 10$ **(Stable Branch)**	L_2 **norm of fitting at** $K = 10$ **(Unstable Branch)**	L_2 **norm of fitting at** $K = 6$ **(Stable Branch)**	L_2 **norm of fitting at** $K = 6$ **(Unstable Branch)**
1	0.821	1.091	0.627	0.728
2	0.413	1.547	0.676	1.441
3	0.489	2.265	0.788	2.098
4	0.657	2.407	1.196	2.069

Table 5.5 L_2-norm of fitting at two different points for various twisted states.

5.3 Varying the coupling range

In this section, we consider the same example of twist-1 with $N = 100$ and randomly distributed frequencies between 0 and 1, but we increase the coupling range from $M = 5$ to $M = 10$. Our aim is to improve the approximation by employing an equation-free approach with two summations.

We first compare the twist-1 solution in the detailed system for $N = 100$ and $M = 10$, and we see the fitting of a spatial function $v_k = (i-1)^k$ with three and then four coefficients. In Figure 5.8, one can observe that the fitting for 3 and 4 coefficients are very good for the stable branch at $K = 10$ but not for the unstable branch where outliers start to be an issue.

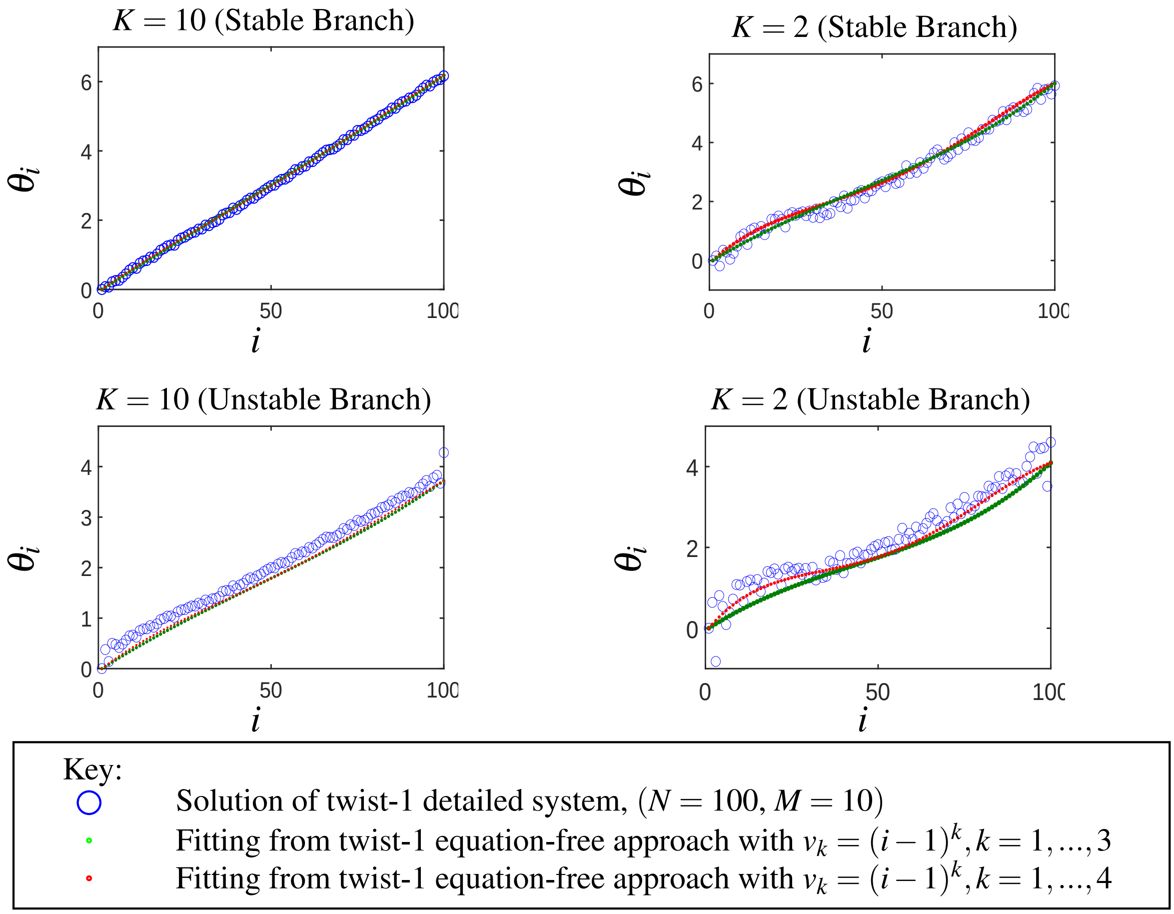

Figure 5.8 Comparison of the fitting of the stable and unstable branches at $K = 10$ and $K = 2$ for twist-1, $N = 100$, $M = 10$ when the number of coefficients are 3 and 4 with spatial function $v_k = (i-1)^k$.

The fitting at $K = 2$ (which is closer to the bifurcation point) is also shown in Figure 5.8 for both the stable and unstable branches. For both the points at $K = 2$ and $K = 10$, the green and red lines demonstrate the fitting of 3 and 4 coefficients using the spatial function $v_k = (i-1)^k$, while the blue circular line displays the solution of a detailed system. It can be seen that for the given system, the width does exist at $K = 2$ and that adding additional spatial functions improves the fitting in terms of shape but not in terms of width. Therefore, we require an additional function to improve both the width and shape of the fitting.

We apply an equation-free approach with the lifting and restricting operator defined in Equation 5.1 and Equation 5.2. We find the solution with an equation-free approach using the combination of 6 (with $\phi_j = \omega^j, j = 1,...2$ and $v_k = (i-1)^k, k = 1,...,3$) and 8 coefficients (with $\phi_j = \omega^j, j = 1,...2$ and $v_k = (i-1)^k, k = 1,...,4$). Here, the fitting of a twist-1 detailed system with the combination of 6 coefficients are represented by Figure 5.9, whereas the fitting with 8 coefficients are represented by Figure 5.10. For both the figures, A1 depicts the two-dimensional fitting (using two summations), whereas A2 and A3 show the projection of the fitting into the θ_i-i plane and θ_i-ω_i plane respectively, at $K = 2$ stable branch. Similarly, B1 represents the two-dimensional fitting (using two summations) at $K = 2$ unstable branch, whereas B2 and B3 illustrate the projection of the fitting into the θ_i-i and θ_i-ω_i planes respectively. One can see from both figures that the 8 coefficient fitting is better than the 6 coefficient fitting.

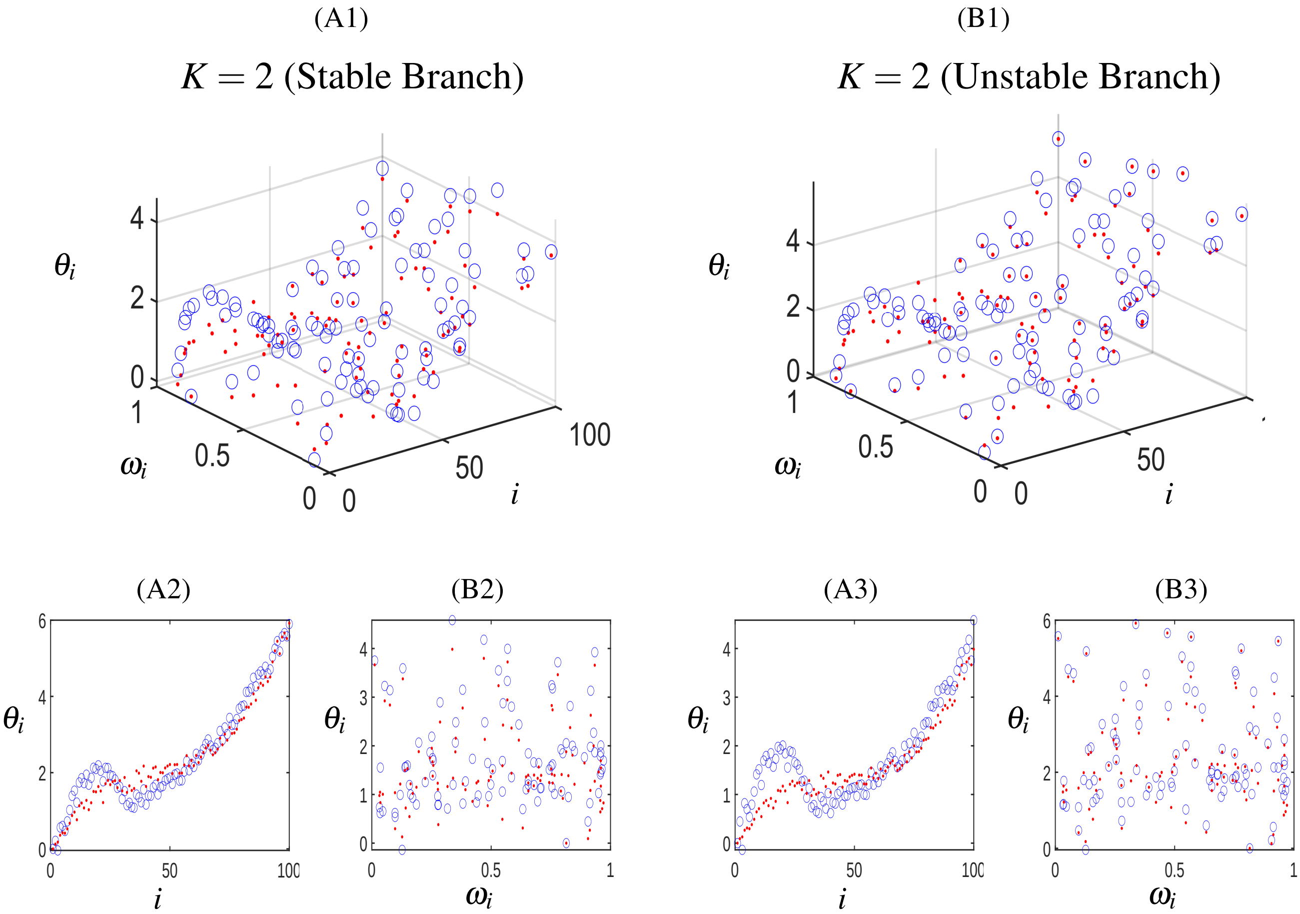

Figure 5.9 Comparison of the two-dimensional fitting (using two summations) of stable and unstable branches at $K = 2$ for twist-1 when there are 6 coefficients. Here, $v_k = (i-1)^k, k = 1,...,3$ and $\phi_j = \omega^j, j = 1,2$.

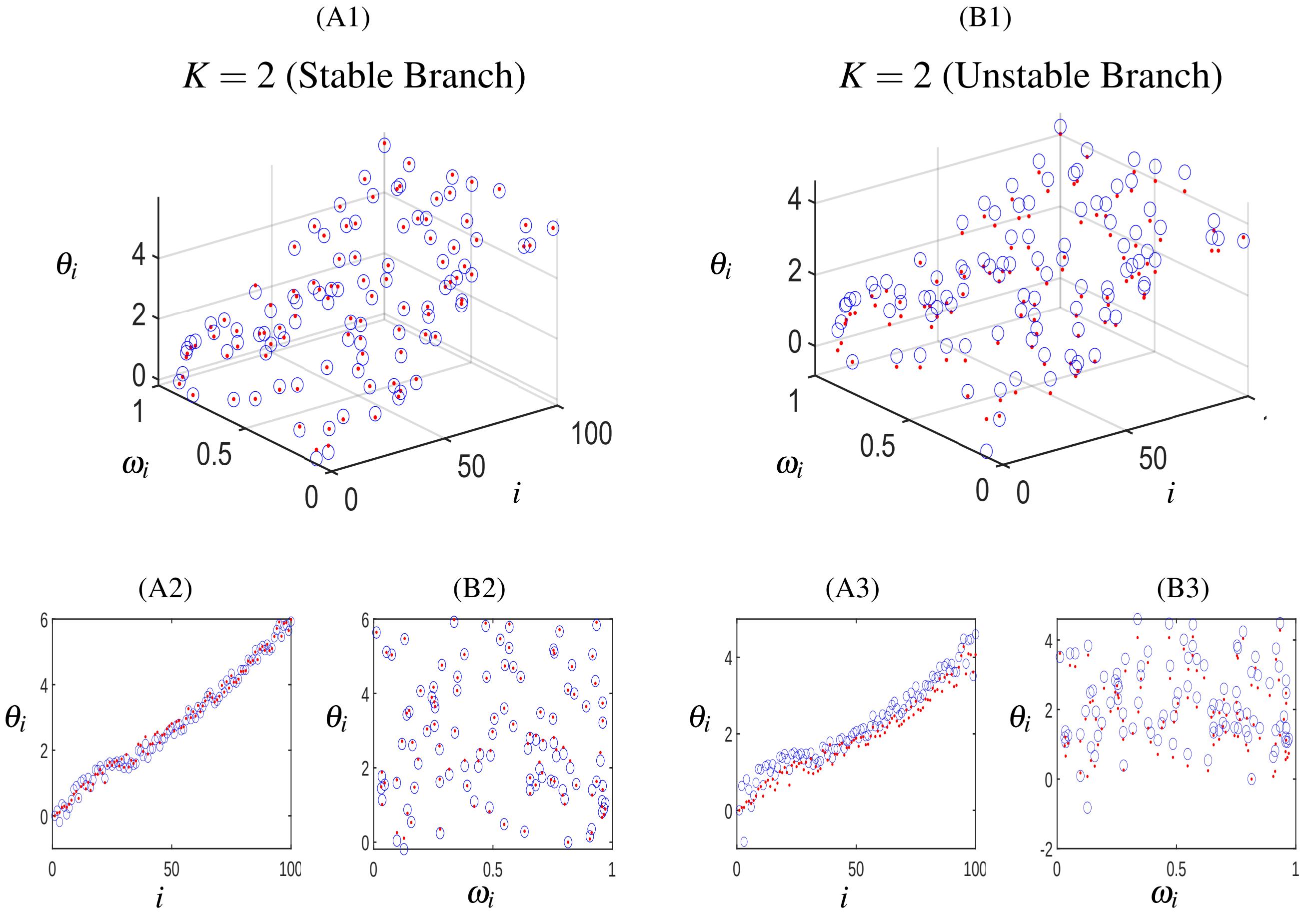

Figure 5.10 Comparison of the two-dimensional fitting (using two summations) of stable and unstable branches at $K = 2$ for twist-1 when there are 8 coefficients. Here, $v_k = (i-1)^k, k = 1, \ldots, 4$ and $\phi_j = \omega^j, j = 1, 2$.

Next, for both scenarios where the coefficients are 6 and 8, we create the bifurcation diagrams (Figure 5.11 and Figure 5.12 respectively).

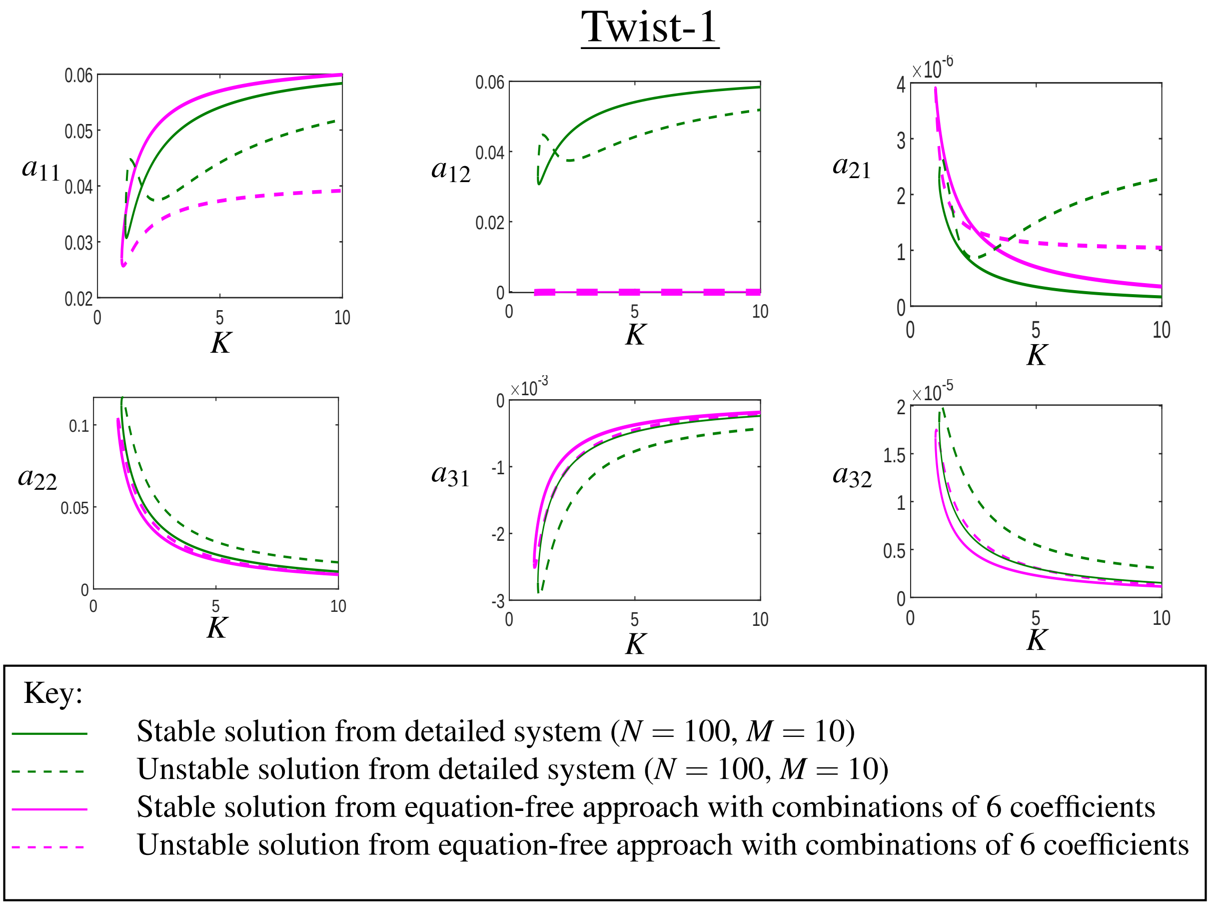

Figure 5.11 Comparison of the solutions of twist-1 equation-free approach (pink color) using two summations with the twist-1 detailed system (green color) for $N = 100$, $M = 10$ and randomly distributed frequencies between 0 and 1. The spatial functions are $v_k = (i-1)^k, k = 1, ..., 3$ where i is the oscillator number and $\phi_j = \omega^j, j = 1, 2$. The bifurcation point for the detailed system is $K = 1.163$, whereas the bifurcation point with an equation-free approach for 6 coefficients is $K = 0.996$. It can be seen that for six coefficients, the solution converges to the stable branch of the detailed system for a_{22}, a_{31}, a_{32}.

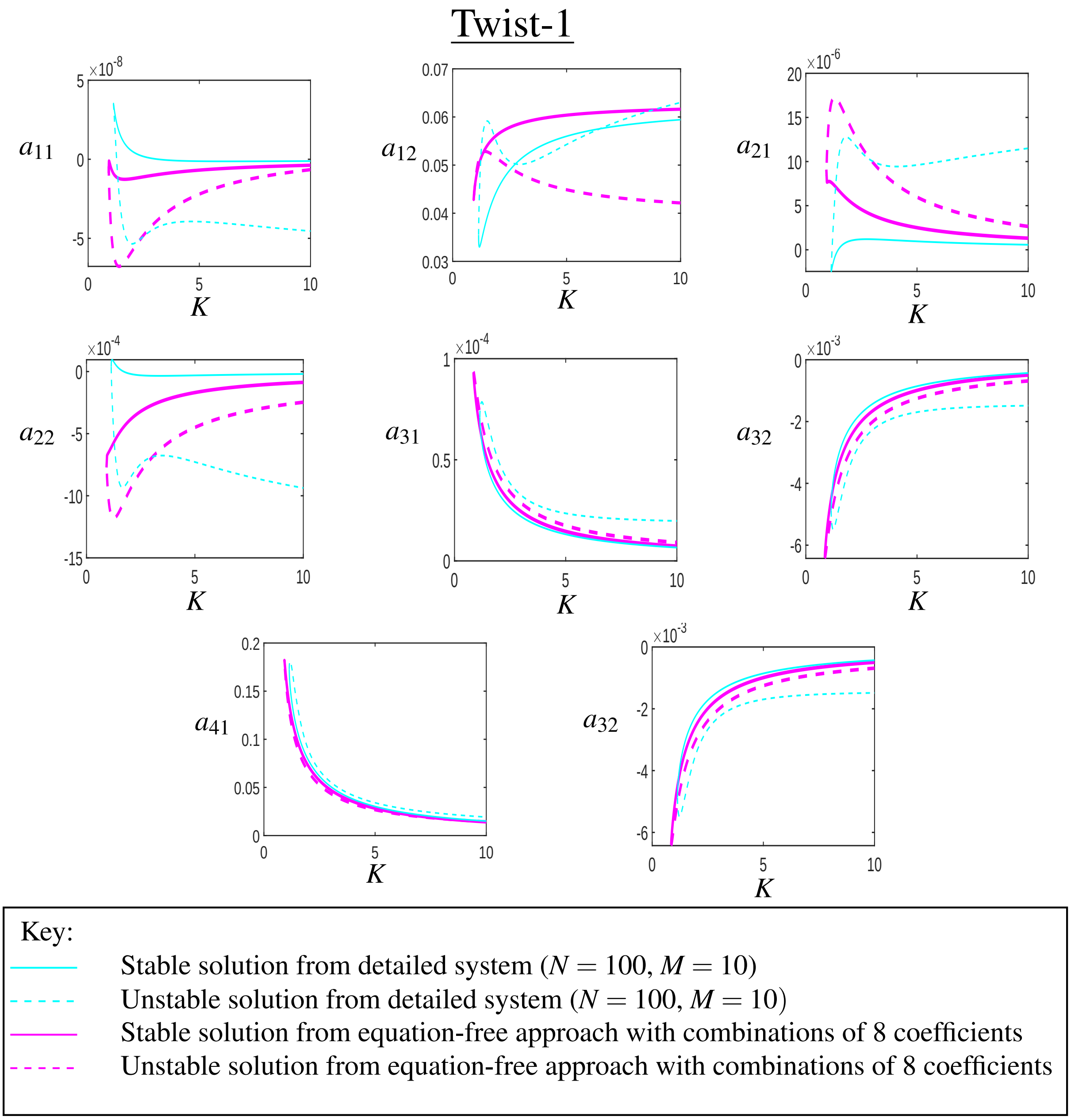

Figure 5.12 Comparison of the solutions of twist-1 equation-free approach (pink color) using two summations with the twist-1 detailed system (cyan color) for $N = 100$, $M = 10$ and randomly distributed frequencies between 0 and 1. The spatial functions are $v_k = (i-1)^k, k = 1, \ldots, 4$ where i is the oscillator number and $\phi_j = \omega^j, j = 1, 2$. The bifurcation point for the detailed system is $K = 1.163$, whereas the bifurcation point with an equation-free approach for 8 coefficients is $K = 0.927$. It can be seen that for eight coefficients, the solution converges to both the stable and unstable branches of the detailed system for $a_{31}, a_{32}, a_{41}, a_{42}$ while for $a_{11}, a_{12}, a_{21}, a_{22}$ the solution converges only to the stable branch.

We now vary the number of coefficients from 3 to 9 for $M = 10$ using the same combinations of ϕ_j and v_k as we considered for $M = 5$ and compare the solution of the detailed system with an equation-free approach. Figure 5.13 shows that for a_{11}, as the

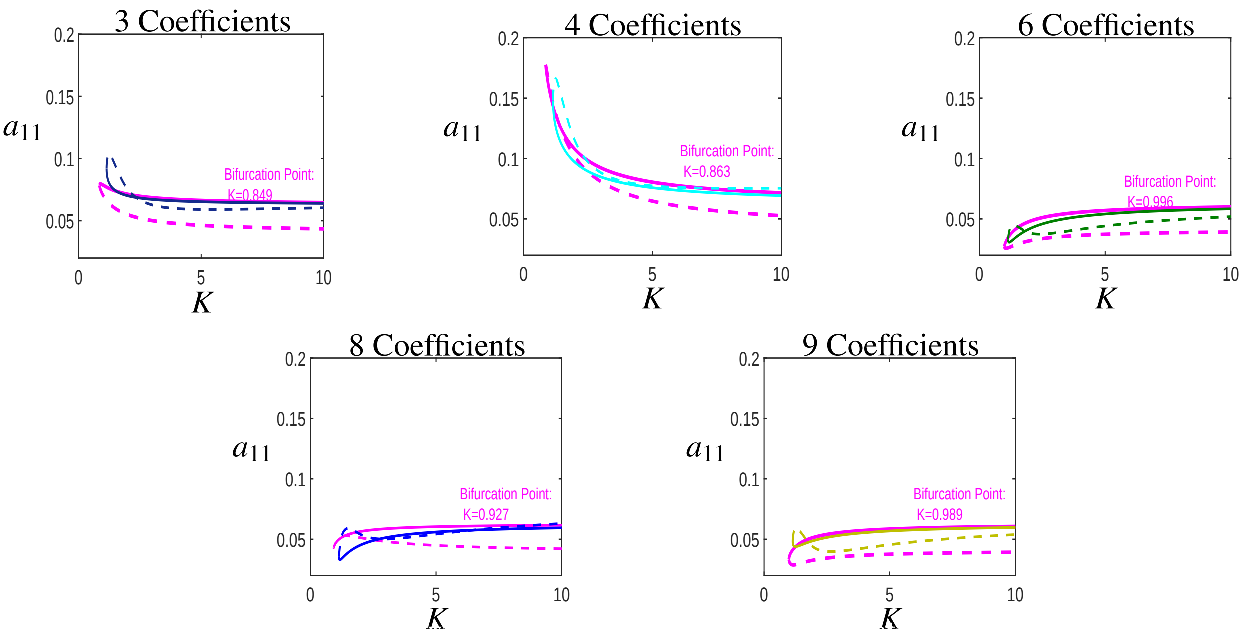

Figure 5.13 Bifurcation diagrams for a_{11} of twist-1, $N = 100$, $M = 10$ with various coefficients. The results show that the bifurcation point of an equation-free approach gets closer to the bifurcation point of the detailed system albeit not uniformly, and the stable and unstable branches from the equation-free approach and detailed system become indistinguishable as we move away from the bifurcation point.

number of coefficients increases, the bifurcation point of an equation-free approach gets closer to the bifurcation point of the detailed system. ($K = 1.163$). Furthermore, in all of these cases of varying coefficients, the stable branch of an equation-free approach converges to that of the detailed system.

Coefficient Numbers	$\lvert a_{11,Ef} - a_{11,ds}\rvert$ **at $K = 10$ (Stable Branch)**	$\lvert a_{11,Ef} - a_{11,ds}\rvert$ **at $K = 10$ (Unstable Branch)**	$\lvert a_{11,Ef} - a_{11,ds}\rvert$ **at $K = 2$ (Stable Branch)**	$\lvert a_{11,Ef} - a_{11,ds}\rvert$ **at $K = 2$ (Unstable Branch)**
3	0.0005	0.0168	0.0011	0.0204
4	0.0023	0.0227	0.0106	0.0133
6	0.0015	0.0127	0.0061	0.0064
8	0.0021	0.0208	0.0111	0.0027
9	0.0008	0.0145	0.0026	0.0100

Table 5.6 Error difference between the detailed system's true solution $a_{11,ds}$ and the equation-free's estimated solution $a_{11,Ef}$ for various coefficients at $K = 2$ and $K = 10$.

It can be seen that as the number of coefficients increases, the bifurcation point from the equation-free approach gets closer to the actual bifurcation point of the detailed system

Coefficient Numbers	**L_2 norm of fitting at $K = 10$ (Stable Branch)**	**L_2 norm of fitting at $K = 10$ (Unstable Branch)**	**L_2 norm of fitting at $K = 2$ (Stable Branch)**	**L_2 norm of fitting at $K = 2$ (Unstable Branch)**
3	0.391	2.261	1.941	3.986
4	0.381	1.961	1.945	2.763
6	0.196	2.169	0.937	3.151
8	0.187	1.996	0.966	2.355
9	0.191	2.178	0.916	3.135

Table 5.7 L_2-norm for detailed solution and the approximated solution at $K = 2$ and $K = 10$.

$K = 1.163$. We now evaluate the error differences between the detailed solution $a_{11,ds}$ and the approximated solution $a_{11,Ef}$ in Table 5.6 and the L_2-norm in Table 5.7. Once again, we make the comparison of two values of coupling strength on the stable and unstable branches, one close to the bifurcation point ($K = 2$) and one farther away ($K = 10$). As the number of coefficients increases, we can observe that the estimated solution begins to converge towards the true solution and the error between them reduces.

5.4 Discussion and Conclusions

This chapter is motivated by the fact that closer to the bifurcation point, the solution curve θ_i as a function of i, has width. We developed a two-summations, equation-free approach to enhance the fitting in terms of width. One summation is for changing the oscillators' location i, which will improve the shape of the fitting, and the other is for altering the oscillators' angular frequencies that will increase the fitting's width. We presented the two-dimensional fitting from both the stable and unstable branches, illustrating how the fitting was improved by the addition of a second function. Using the two summations equation-free approach, we formed the bifurcation diagrams. Later, we picked two different points on the bifurcation curve and found the error differences between the true solution and the equation-free approach's estimated solution for various coefficients. We varied those coefficients by considering different combinations of v_k and ϕ_j and found that the error between them decreases non-uniformly. We also varied the coupling range and observed the same convergence behavior of the solution. In general, the stable solution obtained by the equation-free approach converged to those obtained by the detailed system for large values of the coupling strength, K, but the convergence of the unstable solutions seem to be affected by poor fitting due to outliers.

Chapter 6

Conclusions

The aim of this thesis was to find a reasonable lower-dimensional representation for a large network of coupled oscillators with heterogeneous frequencies. Such a representation may speed up simulations and provide insights into the emergent properties of large networks. We investigated two kinds of networks: one in which each oscillator is connected to its nearby oscillators (known as a spatially extended network) and another in which each oscillator is connected to all other oscillators (known as an all-all network). By increasing the coupling range, M, we could transit between a spatially extended network to the all-all network. Hence we treat the all-all network as a special case of the spatially extended network.

Each oscillator in our network was represented by a Kuramoto model. To facilitate the transition between the spatially extended network and the all-all network, we scaled the coupling range, K, by $(N-1)$ in the all-all network (see Eq. (2.1)) rather than by N (as has been done for example in [31, 1, 56, 46, 39, 53, 38, 22, 37, 40, 52]) and dividing K by $2M$ in the spatially extended network (see Eq. (2.2)) rather than other parameters as has been done previously in [61, 44, 34, 63]. The Kuramoto model has been studied by many before (see Chapter 1), but few studies have applied the equation-free technique to this system. The specific analysis we present in this thesis is new.

In Chapter 2, we presented a detailed numerical analysis of both networks in the absence of an equation-free approach. We utilized these results as a benchmark in the following chapters, as we study both networks in lower dimensions using an equation-free approach. As the state of the oscillators in both networks changed with time, we applied two methods for analyzing the moving pattern.

For the first method, we observed that all the oscillators move with the same angular speed at steady state, and we subtracted this angular speed from the equations, effectively analyzing the equations on a rotating frame. We showed that the angular speed of the synchronized network at steady state is equal to the average of the natural frequencies of the oscillators. Although this idea has been used in [5] to analyze the Kuramoto network, it was not proved there. Furthermore, our theorem is true for the more general spatially extended network.

For the second method, we considered the oscillator's relative positions, which remain unchanged at steady state. We wrote the equations explicitly for the all-all Kuramoto network, but generated the equations numerically for the spatially extended network.

In this chapter, we used both methods to calculate fixed points, determine their stability, and generate bifurcation diagrams when the coupling strength, K, varies. We generated the bifurcation diagrams using our own software and compared them with those generated by the software CLMATCONT-L (an advanced Matlab package used for studying large-scale dynamical systems and their bifurcations, [6]). We showed numerically that the twisted states exist for lower values of the coupling range, M. By gradually increasing the coupling range, more oscillators connect with each other, and the only twist we get is twist-0.

We noticed that for large values of M, the state of the oscillators becomes a function of their angular frequencies. We also discovered that for smaller values of M, the state of the oscillators becomes a function of their positions. This correlation allows us to expand θ_i in terms of polynomials. Thus, we used a polynomial expansion technique to apply an equation-free approach to both networks.

The technique of using a polynomial expansion for an equation-free approach on the all-all Kuramoto model has also been studied in the past. In [40], the state of the oscillators was expressed as a function of only one of its heterogeneous parameters, namely the frequency. Bertlan et al. (2017) expressed the state of oscillators in terms of two heterogeneous parameters: intrinsic frequency and the degree of connectivity. In this thesis, we expressed θ_i as a function of the frequency and the position.

Because we have a degree of freedom for our rotating frame, we selected polynomials in a power series as a convenient way to make sure that $\theta_i = 0$ at $i = 1$ (an arbitrary condition we imposed). The choice of polynomials is different from those chosen in [40] who used the Hermite polynomials and [5] who used univariate polynomials. Other authors, such as [64], showed that if the frequencies are taken from the normal distribution, Hermite polynomials give the best convergence of expansion. In case of a uniform distribution of frequencies, Legendre polynomials are appropriate, and if a gamma distribution is used, then Laguerre polynomials are best. Our findings indicate that although the polynomials we chose are simpler, we still get good convergence with a small number of coefficients.

We discussed the equation-free framework in Chapter 3. To assess and enhance the efficiency of our computations, we demonstrated computing tasks such as the coarse-projective integration.We created bifurcation diagrams at the coarse-grained level for both networks in Chapter 4. The bifurcation diagrams were created using the equation-free approach with one summation when θ_i were functions of their positions, and when θ_i were functions of their natural angular frequencies. We compared the results with those of the detailed system obtained in Chapter 2. We found that at lower values of the coupling range, M, the stable and unstable solutions of the twist-1 state of the equation-free system converged to the stable and unstable branches of the twist-1 state of the detailed system. For this, we used only 4 coefficients and represented θ_i in terms of their positions. However, when we got to higher twisted states (such as twist-2), although the stable solution converged to that of the detailed system, the unstable branch did not. When we compared the coarse-grained solution for twist-2 with various twisted states of the detailed system, we found that the unstable solution for twist-2 of the equation-free system became close to the stable solution of twist-3 (see Figure 4.7). This is because, when viewed at the coarse level, the distinction between the twisted states is not obvious.

When we increased the coupling range and created a bifurcation diagram using the equation-free approach with one summation approximating θ_i as a function of its natural frequencies, we noticed that for twist-0, the stable branch converged to the stable solution of the twist-0 detailed system. However, the unstable branches for an equation-free solution converged to each other but not to the unstable solution of the detailed system (see Figure 4.12).

To understand why the solution failed to converge, we checked the fitting of an equation-free solution with the detailed system. The fitting was very good for the stable branch, however, for the unstable branch an outlier in the detailed system existed (see Figure 4.13).

We also compared the bifurcation point of the equation-free approach to the bifurcation point of the detailed system. We demonstrated that 3 to 4 coefficients are sufficient to come closer to the bifurcation point of the detailed system. We did notice, however, that the bifurcation point of the equation-free approach is always ahead of the bifurcation point of the detailed system. To find the reason behind this behaviour, we compared the fitting at a point closer to the bifurcation point of the approximated solution with the detailed solution. We observed that there exists a width in the solution of the detailed system.

To enhance the fitting, we represented θ_i in terms of both position and their natural angular frequencies in Chapter 5 using two summations. We found this caused the bifurcation points of the coarse-grain and detailed systems to become closer. For twist-1, both the stable and unstable solutions converged to the solution of the detailed system as the value of K was increased (see Figure 5.4). The solutions were less close for higher twists, and the same behaviour was observed for larger values of the coupling range, M (see Figure 5.13).

Overall, we can conclude that the equation-free approach worked for stable solutions and relatively low twist solutions but that the unstable solutions did not converge in most cases due to the existence of outliers.

Future studies could explore ways to improve the fitting when outliers exist in the solution and test the equation-free approach on other types of networks. The fact that the convergence of higher twisted states is worse than lower twisted states (see Table 5.5) could be explored further.

Appendix A

Appendix

A.1 Numerical Continuation

In this section, we extract the ideas from the paper [32] to explain bifurcation theory and numerical continuity processes. Consider a differential equation, assuming that its solution can not be analytically achievable.

$$\frac{dx}{dt} = f(x,\mu) = x^4 - x + \mu^2 - 1 \quad \forall x \in \mathbb{R},\ \mu \in \mathbb{R} \tag{A.1}$$

In this example, the two elements x and μ are both components of a function f, where vector x is a time-dependent quantity, μ is a parameter and $\frac{d}{dt}$ is the time differentiation operator. Note that for larger positive or negative values of μ, $\frac{dx}{dt}$ is always positive so no fixed points exist for Eq.(A.1). However, we have two fixed points for smaller values of μ.

One approach for finding fixed points for the system Eq.(A.1) is the numerical integration method in which the system is integrated for a longer period of time. However, this can only be possible if the initial conditions are small enough. Newton's method is another convenient way to locate Eq.(A.1)'s fixed points, if we start near enough to their roots. The only drawback is that the convergence of this approach does not depend on a particular point's stability therefore we might get unstable fixed points.

A better way to determine all the stable and unstable fixed points for our system Eq.(A.1) is a numerical continuation technique. For that, we find a fixed point at one of the parameter's value and pursue this solution as that parameter varies, eventually mapping the entire solutions to get a complete picture of convergence.

Consider a fixed point which satisfies the condition $f(x_0,\mu_0) = 0$. Another close by point (x_1,μ_1) will be found so that it fits $f(x_1,\mu_1) = 0$. We would like to follow the solutions of x as the parameter μ varies. Considering an initial point (x_1,μ_1) which satisfies

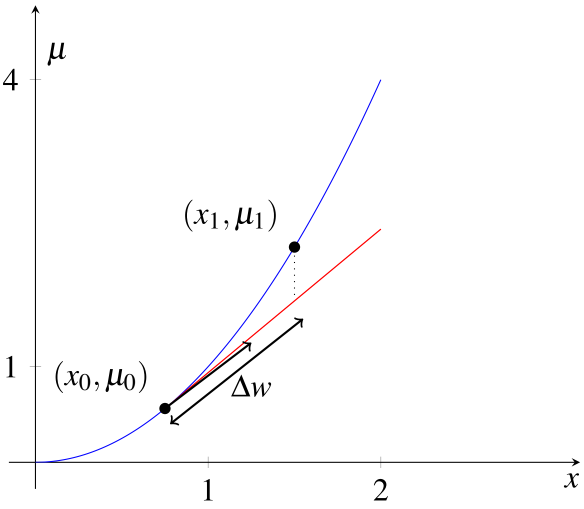

Figure A.1 Graphical representation of Eq.(A.2). The dotted line is the normal to the tangent line. The part of the solution is shown with the blue curve, and the bold, single-headed straight arrow line is representing the tangent at (x_0,μ_0)

the condition $f(x_1,\mu_1) = 0$ and the condition

$$(x_1 - x_0)\dot{x}_0 + (\mu_1 - \mu_0)\dot{\mu}_0 - \Delta w = 0 \tag{A.2}$$

In the above (A.2), Δw is the arc length, which reflects the distance between two consecutive points. It might be of any appropriate step size. The tangent vector of the curve at the point (x_0,μ_0) is $(\dot{x}_0,\dot{\mu}_0)$. It might be long, but we normalized it to have 1 unit length. The tangent vector leads us to the next point by giving us the direction, while Δw tells us how far we should go that way. Moreover, the over dot implies differentiation with respect to arc length w. Therefore, we have parametrized the curve to arc-length w, so that our $f(x,\mu)$ function becomes $f(x(w),\mu(w)$. By varying w, x and μ vary and arc length w can be used to find the solutions. It should be kept in mind that if one is taking constant arc-length measures, the interval between the points should be approximately constant.

Geometrically, this illustrates the linearization condition, as the tangent line or arc length approximates the curve. It shows that we move along the tangent from the initial point (x_0,μ_0), through the span of Δw, then heads perpendicularly towards the curve to get our desired next point (x_1,μ_1). It is located simultaneously on a curve (solid blue arc) , right angled to a tangent (dotted line) and Δw distance away from a point (x_0,μ_0). Notice that there are many points on this dotted line but the one we like, must be the one on the curve, too. We must, therefore, have two equations to meet two conditions and to find a solution to one point. Thus, for (x_1, μ_1), we solve $f(x_1, \mu_1) = 0$ and the following condition simultaneously

$$\begin{pmatrix} x_1^{(n)} \\ \mu_1^{(n)} \end{pmatrix} = \begin{pmatrix} x_1^{(n-1)} \\ \mu_1^{(n-1)} \end{pmatrix} - \boldsymbol{J}_{(n-1)}^{-1} \begin{pmatrix} f(x_1^{(n-1)}, \mu_1^{(n-1)}) \\ (x_1^{(n-1)} - x_0)\dot{x}_0 + (\mu_1^{(n-1)} - \mu_0)\dot{\mu}_0 - \Delta w \end{pmatrix} \tag{A.3}$$

$\forall\ n = 1, 2, ..., N_N$, To get a tangent line, $f(x(w), \mu(w)) = 0$ is differentiated w.r.t arc length w and then computed at (x_0, μ_0).

$$[f_x \qquad f_\mu] \begin{bmatrix} \dot{x}_0 \\ \dot{\mu}_0 \end{bmatrix} = 0 \tag{A.4}$$

$$\left[\left(\frac{\partial f}{\partial x} \right) \left(\frac{dx}{dw} \right) + \left(\frac{\partial f}{\partial \mu} \right) \left(\frac{d\mu}{dw} \right) \right] \Bigg|_{(x_0, \mu_0)} \begin{pmatrix} \dot{x}_0 \\ \dot{\mu}_0 \end{pmatrix} = 0 \tag{A.5}$$

where,

$$\boldsymbol{J}_{(n)} = \begin{pmatrix} f_x & f_\mu \\ \dot{x}_0 & \dot{\mu}_0 \end{pmatrix} \tag{A.6}$$

Consider N_N iterations with an assumption that Eq.(A.1) converges, such as $(x_1, \mu_1) = (x_1^{(N_N)}, \mu_1^{(N_N)})$. Initially, we take $(x_1^0, \mu_1^{(0)}) = (\mu_0 + \dot{\mu}_0 \Delta w, x_0 + \dot{x}_0 \Delta w)$. This refers to a point where both the tangent line and dotted line intersects (see Figure A.2). After that, we used Newton-Raphson method to compute N_N Newton's iteration with Eq.(A.2). If Eq.(A.2) converges, (x_1, μ_1) equals $(x_1^{(N_N)}, \mu_1^{(N_N)})$ regards as the corrector of the prediction step. We are able to check this point stability (x_1, μ_1) by finding the sign of f_x which is evaluated at the top left of Jacobian. To determine the next point, (x_2, μ_2) along the curve, we can use newtonian iterations, i.e

$$\begin{pmatrix} x_2^{(n)} \\ \mu_2^{(n)} \end{pmatrix} = \begin{pmatrix} x_2^{(n-1)} \\ \mu_2^{(n-1)} \end{pmatrix} - \boldsymbol{J}_{(n-1)}^{-1} \begin{pmatrix} f(x_2^{(n-1)}, \mu_2^{(n-1)}) \\ (x_2^{(n-1)} - x_0)\dot{x}_0 + (\mu_2^{(n-1)} - \mu_0)\dot{\mu}_0 - \Delta w \end{pmatrix} \tag{A.7}$$

$\forall n = 1, 2, \cdots, N_N$, where the Jacobian is already defined in Eq. (A.6) and the partial derivatives are computed at $(x_2^{(n)}, \mu_2^{(n)})$. Moreover, we can compute the tangent vector $(\dot{x}_1, \dot{\mu}_1)$ by using the approximation

$$\dot{x}_1 \approx \frac{x_1 - x_0}{\Delta w} \qquad \dot{\mu}_1 \approx \frac{\mu_1 - \mu_0}{\Delta w} \tag{A.8}$$

This procedure can locate as many points as required.

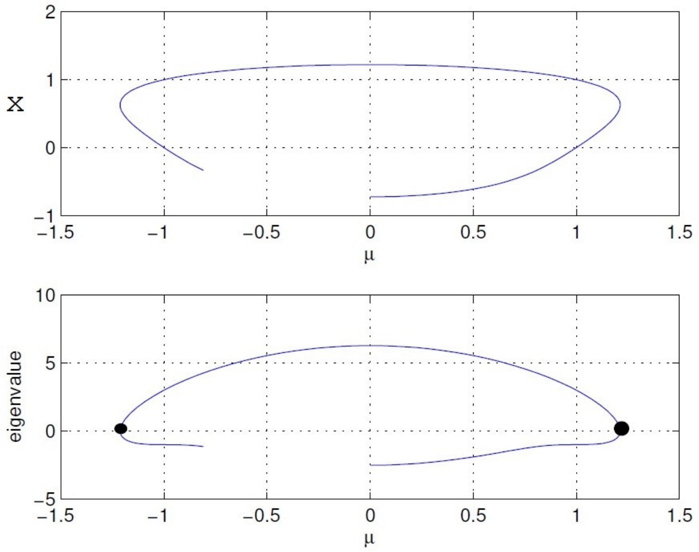

Figure A.2 Phase portrait representation of the system described by Eq. (A.1) with respect to the variable x and parameter μ. The first panel in Figure A.2 displays the phase portrait of the system for variable x as μ varies. The second panel illustrates the corresponding eigenvalues with respect to μ. Notably, as we vary the values of μ, the eigenvalues undergo a transition from negative to positive, leading to an unstable solution at the point $(-1.25, 1.25)$. These critical points are indicated by two solid dots, representing the bifurcation points in the system.

A.2 List of Shifted Legendre Polynomials

Shifted Legendre polynomials are a family of orthogonal polynomials defined on the interval $[-1,1]$. They are related to the classical Legendre polynomials but are shifted and normalized to have specific properties. The nth normalized shifted Legendre polynomial, denoted by $P_n(x)$, is defined as follows:

$$P_n(x) = \sqrt{n+\frac{1}{2}} \cdot P_n^{(s)}(x),$$

where $P_n^{(s)}(x)$ is the nth shifted Legendre polynomial and is defined by the recurrence relation:

$$P_n^{(s)}(x) = \frac{1}{n}\left[(2n-1)xP_{n-1}^{(s)}(x) - (n-1)P_{n-2}^{(s)}(x)\right],$$

with initial conditions $P_0^{(s)}(x) = 1$ and $P_1^{(s)}(x) = x$.

In an equation-free approach, shifted Legendre polynomials are employed as a reduced representation for unknown or complex functions in dynamical systems. By projecting the unknown function onto a finite series of shifted Legendre polynomials, we can approximate it as a linear combination of these orthogonal basis functions. The coefficients of the shifted Legendre polynomials serve as reduced variables, and the unknown function is evolved in time using these coefficients. This approach is particularly useful when the underlying equations of the system are unknown, computationally expensive, or challenging to solve directly. It allows for efficient simulations and exploration of system dynamics without explicit knowledge of the governing equations, leveraging the orthonormality and other useful properties of shifted Legendre polynomials. The equation-free approach with shifted Legendre polynomials offers advantages in efficiently simulating complex systems when explicit equations are unknown or computationally expensive. However, it comes with limitations, including reduced accuracy for low truncation orders, limited applicability for highly nonlinear or chaotic systems, and high computational cost for high-dimensional systems. Collecting sufficient data for accurate representation can be challenging, and the reduced models lack clear physical interpretations. Additionally, stability issues may arise depending on the numerical integration scheme used. Despite these drawbacks, the equation-free approach remains a valuable tool for understanding system behavior when traditional methods are impractical. Some of the shifted legendre polynomials are listed below which have been used in Chapter 2 (upto ϕ_3).

$$
\begin{aligned}
\phi_0 =& 1 \\
\phi_1 =& 2\omega - 1 \\
\phi_2 =& 6\omega^2 - 6\omega + 1 \\
\phi_3 =& 20\omega^3 - 30\omega^2 + 12\omega - 1 \\
\phi_4 =& 70\omega^4 - 140\omega^3 + 90\omega^2 - 20\omega + 1 \\
\phi_5 =& 252\omega^5 - 630\omega^4 + 560\omega^3 - 210\omega^2 + 30\omega - 1 \\
\phi_6 =& 924\omega^6 - 2772\omega^5 + 3150\omega^4 - 1680\omega^3 + 420\omega^2 - 42\omega + 1 \\
\phi_7 =& 3432\omega^7 - 12012\omega^6 + 16632\omega^5 - 11550\omega^4 + 4200\omega^3 - 756\omega^2 + 56\omega - 1 \\
\phi_8 =& 12870\omega^8 - 51480\omega^7 + 84084\omega^6 - 72072\omega^5 + 34650\omega^4 - 9240\omega^3 + 1260\omega^2 \\
& - 72\omega + 1 \\
\phi_9 =& 48620\omega^9 - 218790\omega^8 + 411840\omega^7 - 420420\omega^6 + 252252\omega^5 - 90090\omega^4 + 18480\omega^3 \\
& - 1980\omega^2 + 90\omega - 1 \\
\phi_{10} =& 184756\omega^{10} - 923780\omega^9 + 1969110\omega^8 - 2333760\omega^7 + 1681680\omega^6 - 756756\omega^5 + \\
& 210210\omega^4 - 34320\omega^3 + 2970\omega^2 - 110\omega + 1 \\
\phi_{11} =& 705432\omega^{11} - 3879876\omega^{10} + 9237800\omega^9 - 12471030\omega^8 + \\
& 10501920\omega^7 - 5717712\omega^6 + 2018016\omega^5 - 450450\omega^4 + 60060\omega^3 - 4290\omega^2 + 132\omega - 1
\end{aligned}
\tag{A.9}
$$

A.3 Algorithm for applying Equation-free approach on heterogenous networks

Algorithm 1 Main algorithm for solving heterogenous networks using an equation-free approach.

```
Solve the ODE using ode45 with ddKuraNode function, time interval $[0 : 0.1 : 200]$, and initial values linspace(0, $2\pi$, N)
Get function value $f_1$ using functionNRC_Test with input $K$ and last row of $\theta_i$, calling it as $u$.
Set $A = \phi$
Subtract first element of $u$ from the last row of $u$ and store in $uS$
Get function value $f_1$ using functionNRC_Test with input $K$ and $uS$
Calculate $b$ using $A \backslash uS'$
Calculate $\theta_{\text{matrix}}$ using $A$ and $b$
Get function value $f_1$ using functionNRC_Test with input $K$ and $\theta_{\text{matrix}}$
Set $b_{\text{old}} = b$
Get function value $f$ using functionNRC with input $K$ and $b_{\text{old}}$
Get finite difference $SS$ using finitediffNR with input $K$ and $b_{\text{old}}$
Solve linear system $SS \cdot z = f$ to get $z$
Update $b_{\text{new}} = b_{\text{old}} - z$
Calculate error1 as norm$(f)$
Set $b_{\text{old}} = b_{\text{new}}$
Plot $uS$ and $A \cdot b_{\text{old}}$
for $i$ from 1 to 20 do
    Get function value $f$ using functionNRC with input $K$ and $b_{\text{old}}$
    Get finite difference $SS$ using finitediffNR with input $K$ and $b_{\text{old}}$
    Solve linear system $SS \cdot z = f$ to get $z$
    Update $b_{\text{new}} = b_{\text{old}} - z$
    Calculate error1 as norm$(f)$
    Store $b_{\text{new}}$ in Coefficients$(:, i)$
    Update $b_{\text{old}} = b_{\text{new}}$
    if error1$(i) < 1e-8$ then
        Break loop
    end if
end for
if $i = 20$ then
    Display error message ("solution not converging")
end if
```

Algorithm 1 Main algorithm for solving heterogenous networks with an equation-free approach.(Continued)

```
Set $b_{\text{new}} = b_{\text{new}}$
Calculate nullv using null of $[\texttt{finitediffNR}(K, b_{\text{new}}, \varepsilon), \texttt{KfinitediffNR}(K, b_{\text{new}}, \varepsilon)]$ functions.
Get dimensions Nr and Nb of $b_{\text{new}}$
Set NN $= 5$, ds $= -0.0001$, and tot $= 200000$
Initialize JJ, vv, dat, and ei matrices
Set $\text{dat}(:,1) = [b_{\text{new}}; K; 0]$
Get finite difference matrix $J$ using finitediffNR with input $K$ and $b_{\text{new}}$
Calculate eigenvalues of $J$ and store in $\text{ei}(:,1)$
for Outer_loop from 1 to tot do
    Set $\text{vvold} = \text{dat}(1:\text{Nb}+1, \text{Outer\_loop})$
    Set $\text{vv}(:,1) = \text{dat}(1:\text{Nb}+1, \text{Outer\_loop}) + \text{ds} \cdot \text{nullv}$
    for inner_loop from 2 to NN do
        Get $ff$ using Ggetf function with inputs $\text{vv}(:, \text{inner\_loop} - 1)$, vvold, nullv, ds, and Nb
        Calculate ErrorInner as $\text{norm}(ff)$
        Set $\text{dat}(:, \text{Outer\_loop}+1) = [\text{vv}(:, \text{inner\_loop} - 1); \text{ErrorInner}]$
        Update $\text{JJ}(1:\text{Nb},:)$ using $[\texttt{finitediffNR}(\text{vv}(\text{end}, \text{inner\_loop} - 1), \text{vv}(1:\text{Nb}, \text{inner\_loop} - 1), \varepsilon)\ \texttt{KfinitediffNR}(\text{vv}(\text{end}, \text{inner\_loop} - 1), \text{vv}(1:\text{Nb}, \text{inner\_loop} - 1), \varepsilon)]$
        Set $\text{JJ}(\text{Nb}+1,:) = \text{nullv}'$
        Solve linear system $\text{JJ} \cdot dx = ff$ to get $dx$
        Update $\text{vv}(:, \text{inner\_loop}) = \text{vv}(:, \text{inner\_loop} - 1) - dx$
        Calculate eigenvalues of $\text{JJ}(1:\text{end}-1, 1:\text{Nb})$ and store in $\text{ei}(:, \text{Outer\_loop}+1)$
        Calculate nullv as $(\text{dat}(1:\text{Nb}+1, \text{Outer\_loop}+1) - \text{dat}(1:\text{Nb}+1, \text{Outer\_loop}))/\text{ds}$
        Normalize nullv
    end for
end for
```

Algorithm 2 For sub-function `ddKuraNode`

```
procedure DDKURANODE($t, u, K$)
    global $\omega, N, M, V$
    $aa \leftarrow \text{mean}(\omega)$
    if $M \leq \text{ceil}(N/2 - 1)$ then
        $dyddt \leftarrow \omega + \frac{K}{2M}(-\sin(u) \cdot (V \cdot \cos(u)) + \cos(u) \cdot (V \cdot \sin(u))) - aa$
    else
        $dyddt \leftarrow \omega + \frac{K}{N-1}(-\sin(u) \cdot (V \cdot \cos(u)) + \cos(u) \cdot (V \cdot \sin(u))) - aa$
    end if
    return $dyddt$
end procedure
```

Algorithm 1 Algorithm 3 For sub-function `finitediffNR`

```
procedure FINITEDIFFNR($K, b_{\text{old}}, \varepsilon$)
    global $\omega, V, N, M, \phi, aa$
    $[r, c] \leftarrow \text{size}(b_{\text{old}})$
    $I \leftarrow \text{eye}(r, r)$
    $uu_{\text{old\_EpsilonMatrix}} \leftarrow \text{zeros}(r, r)$
    for $i = 1$ to $r$ do
        $uu_{\text{old\_EpsilonMatrix}}(:, i) \leftarrow b_{\text{old}} + (\varepsilon \cdot I(:, i))$
    end for
    FiniteDifference $\leftarrow \text{zeros}(r, r)$
    for $i = 1$ to $r$ do
        FiniteDifference$(:, i) \leftarrow \frac{\texttt{functionNRC}(K, uu_{\text{old\_EpsilonMatrix}}(:, i)) - \texttt{functionNRC}(K, b_{\text{old}})}{\varepsilon}$
    end for
    return FiniteDifference
end procedure
```

Algorithm 4 For sub-function `KfinitediffNR`

```
procedure KFINITEDIFFNR($K, uu_{\text{new}}, \varepsilon$)
    global $\omega, V, N, M, A$
    $derK(:, 1) \leftarrow \frac{\texttt{functionNRC}(K + \varepsilon, uu_{\text{new}}) - \texttt{functionNRC}(K, uu_{\text{new}})}{\varepsilon}$
    return $derK$
end procedure
```

Algorithm 5 For sub-function `functionNRC`

```
procedure FUNCTIONNRC($K, b_{\text{old}}$)
    global $\omega, N, M, V, A$
    $\Theta \leftarrow A \cdot b_{\text{old}}$
    $aa \leftarrow \text{mean}(\omega)$
    if $M \leq \text{ceil}(N/2-1)$ then
        $f1 \leftarrow \omega + \frac{K}{2M} \cdot (-\sin(\Theta) \cdot (V \cdot \cos(\Theta)) + \cos(\Theta) \cdot (V \cdot \sin(\Theta))) - aa$
        $B \leftarrow A(2:\text{end},:)$
        $f2 \leftarrow f1(2:\text{end})$
        $f \leftarrow B \backslash f2$
    else
        $f1 \leftarrow \omega + \frac{K}{N-1} \cdot (-\sin(\Theta) \cdot (V \cdot \cos(\Theta)) + \cos(\Theta) \cdot (V \cdot \sin(\Theta))) - aa$
        $f \leftarrow A \backslash f1$
    end if
    return $f$
end procedure
```

Algorithm 6 For sub-function `Ggetf`

```
procedure GGETF($vv, vv_{\text{old}}, \text{nullv}, ds, Nb$)
    global $\omega, N, M, V, A$
    $K \leftarrow vv(\text{end})$
    $y \leftarrow \text{zeros}(Nb+1, 1)$
    $y(1:Nb, 1) \leftarrow$ functionNRC($K, vv(1:Nb)$)
    $y(Nb+1, 1) \leftarrow ((vv - vv_{\text{old}})' \cdot \text{nullv}) - ds$
    return $y$
end procedure
```

Bibliography

[1] Juan A. Acebrón, Luis L. Bonilla, Conrad J. Pérez Vicente, Félix Ritort, and Renato Spigler. "The Kuramoto Model: A Simple Paradigm for Synchronization Phenomena". In: *Reviews of Modern Physics* 77.1 (2005), p. 137.

[2] Alex Arenas, Albert Díaz-Guilera, Jurgen Kurths, Yamir Moreno, and Changsong Zhou. "Synchronization in Complex Networks". In: *Physics Reports* 469.3 (2008), pp. 93–153.

[3] Yernur Baibolatov, Michael Rosenblum, Zeinulla Zh Zhanabaev, Meyramgul Kyzgarina, and Arkady Pikovsky. "Periodically Forced Ensemble of Nonlinearly Coupled Oscillators: From Partial to Full Synchrony". In: *Physical Review E* 80.4 (2009), p. 046211.

[4] Alain Barrat, Marc Barthelemy, and Alessandro Vespignani. *Dynamical Processes on Complex Networks*. Cambridge University Press, 2008.

[5] Tom Bertalan, Yan Wu, Carlo Laing, C. William Gear, and Ioannis G. Kevrekidis. "Coarse-grained Descriptions of Dynamics for Networks with Both Intrinsic and Structural Heterogeneities". In: *Frontiers in Computational Neuroscience* 11 (2017), p. 43.

[6] David Bindel, Mark Friedman, Willy Govaerts, Jeremy Hughes, and Yuri A Kuznetsov. "CL MATCONTL: a continuation toolbox for large equilibrium problems in MATLAB". In: (2008).

[7] Ilia Izrailevich Blekhman. *Synchronization in Science and Technology*. ASME Press, 1988.

[8] Katherine A. Bold, Yu Zou, Ioannis G. Kevrekidis, and Michael A. Henson. "An equation-free approach to analyzing heterogeneous cell population dynamics". In: *Journal of Mathematical Biology* 55.3 (2007), pp. 331–352.

[9] Ligang Chen, Pablo G. Debenedetti, C. William Gear, and Ioannis G. Kevrekidis. “From Molecular Dynamics to Coarse Self-Similar Solutions: A Simple Example Using Equation-Free Computation”. In: *Journal of Non-Newtonian Fluid Mechanics* 120.1-3 (2004), pp. 215–223.

[10] Shih-Hsin Chen, Chia-Chi Chu, Chun-Hsiung Hsia, and Ming-Cheng Shiue. “Synchronization of Heterogeneous Forced First-Order Kuramoto Oscillator Networks: A Differential Inequality Approach”. In: *IEEE Transactions on Circuits and Systems I: Regular Papers* 69.2 (2021), pp. 757–770.

[11] Hayato Chiba and Georgi S Medvedev. “Stability and bifurcation of mixing in the Kuramoto model with inertia”. In: *SIAM Journal on Mathematical Analysis* 54.2 (2022), pp. 1797–1819.

[12] Chulho Choi, Meesoon Ha, and Byungnam Kahng. “Extended finite-size scaling of synchronized coupled oscillators”. In: *Physical Review E* 88.3 (2013), p. 032126.

[13] David Cumin and Charles P Unsworth. “Generalising the Kuramoto model for the study of neuronal synchronization in the brain”. In: *Physica D: Nonlinear Phenomena* 226.2 (2007), pp. 181–196.

[14] Florian Dörfler and Francesco Bullo. “Synchronization and transient stability in power networks and nonuniform Kuramoto oscillators”. In: *SIAM Journal on Control and Optimization* 50.3 (2012), pp. 1616–1642.

[15] Florian Dörfler and Francesco Bullo. “Synchronization in complex networks of phase oscillators: A survey”. In: *Automatica* 50.6 (2014), pp. 1539–1564.

[16] Sergey N Dorogovtsev, Alexander V Goltsev, and José FF Mendes. “Critical phenomena in complex networks”. In: *Reviews of Modern Physics* 80.4 (2008), p. 1275.

[17] Bard Ermentrout and David H. Terman. *Mathematical Foundations of Neuroscience*. Springer, 2010.

[18] Reza Farhangi and Mohammad Taghi Hamidi Beheshti. “The Kuramoto Model: The Stability Conditions in the Presence of Phase Shift”. In: *Neural Processing Letters* 53.4 (2021), pp. 2631–2648.

[19] C. William Gear, James M Hyman, Panagiotis G Kevrekidis, Ioannis G Kevrekidis, Olof Runborg, and Constantinos Theodoropoulos. “Equation-free, coarse-grained multiscale computation: Enabling microscopic simulators to perform system-level analysis”. In: *Communications in Mathematical Sciences* 1.4 (2003), pp. 715–762.

[20] David Gfeller and Paolo De Los Rios. “Spectral coarse graining and synchronization in oscillator networks”. In: *Physical Review Letters* 100.17 (2008), p. 174104.

[21] JMV Grzybowski, EEN Macau, and T Yoneyama. “On synchronization in power-grids modeled as networks of second-order Kuramoto oscillators”. In: *Chaos: An Interdisciplinary Journal of Nonlinear Science* 26.11 (2016), p. 113113.

[22] Seung-Yeal Ha, Hwa Kil Kim, and Jinyeong Park. “Remarks on the complete synchronization of Kuramoto oscillators”. In: *Nonlinearity* 28.5 (2015), p. 1441.

[23] Hyunsuk Hong, Hugues Chaté, Hyunggyu Park, and Lei-Han Tang. “Entrainment transition in populations of random frequency oscillators”. In: *Physical review letters* 99.18 (2007), p. 184101.

[24] Hyunsuk Hong, Moo-Young Choi, and Beom Jun Kim. “Synchronization on small-world networks”. In: *Physical Review E* 65.2 (2002), p. 026139.

[25] Chun-Hsiung Hsia, Chang-Yeol Jung, Bongsuk Kwon, and Sunghwan Moon. “Synchronization of Kuramoto oscillators with the distributed time-delays and inertia effect”. In: *Applicable Analysis* (2022), pp. 1–20.

[26] Ioannis G Kevrekidis, C. William Gear, and Gerhard Hummer. “Equation-free: The computer-aided analysis of complex multiscale systems”. In: *AIChE Journal* 50.7 (2004), pp. 1346–1355.

[27] Uhnoh Kim, Thierry Bal, and David A. McCormick. “Spindle Waves Are Propagating Synchronized Oscillations in the Ferret LGNd In Vitro”. In: *Journal of Neurophysiology* 74.3 (1995), pp. 1301–1323.

[28] N. Kopell and GB Ermentrout. “Phase Transitions and Other Phenomena in Chains of Coupled Oscillators”. In: *SIAM Journal on Applied Mathematics* 50.4 (1990), pp. 1014–1052.

[29] Gregory Kozyreff, AG Vladimirov, and Paul Mandel. “Global coupling with time delay in an array of semiconductor lasers”. In: *Physical Review Letters* 85.18 (2000), p. 3809.

[30] Yoshiki Kuramoto. “Chemical turbulence”. In: *Chemical oscillations, waves, and turbulence*. Springer, 1984, pp. 111–140.

[31] Yoshiki Kuramoto. “Self-entrainment of a Population of Coupled Non-linear Oscillators”. In: *International Symposium on Mathematical Problems in Theoretical Physics*. Springer, 1975, pp. 420–422.

[32] Carlo Laing. “Numerical Bifurcation Theory for High-Dimensional Neural Models”. In: *The Journal of Mathematical Neuroscience* 4.1 (2014), p. 13.

[33] Carlo Laing. “The Dynamics of Chimera States in Heterogeneous Kuramoto Networks”. In: *Physica D: Nonlinear Phenomena* 238.16 (2009), pp. 1569–1588.

[34] Carlo Laing. “Travelling waves in arrays of delay-coupled phase oscillators”. In: *Chaos: An Interdisciplinary Journal of Nonlinear Science* 26.9 (2016), p. 094802.

[35] Carlo Laing and Ioannis G Kevrekidis. “Periodically forced finite networks of heterogeneous globally-coupled oscillators: A low-dimensional approach”. In: *Physica D: Nonlinear Phenomena* 237.2 (2008), pp. 207–215.

[36] Deok-Sun Lee. “Synchronization transition in scale-free networks: Clusters of synchrony”. In: *Physical Review E* 72.2 (2005), p. 026208.

[37] Mi Jin Lee, Su Do Yi, and Beom Jun Kim. “Finite-time and finite-size scaling of the Kuramoto oscillators”. In: *Physical Review Letters* 112.7 (2014), p. 074102.

[38] Yu Maistrenko, Oleksandr Popovych, Oleksandr Burylko, and Peter A Tass. “Mechanism of desynchronization in the finite-dimensional Kuramoto model”. In: *Physical Review Letters* 93.8 (2004), p. 084102.

[39] Renato E Mirollo and Steven H Strogatz. “The spectrum of the locked state for the Kuramoto model of coupled oscillators”. In: *Physica D: Nonlinear Phenomena* 205.1-4 (2005), pp. 249–266.

[40] Sung Joon Moon, R. Ghanem, and Ioannis G. Kevrekidis. “Coarse Graining the Dynamics of Coupled Oscillators”. In: *Physical Review Letters* 96.14 (2006), p. 144101.

[41] Sung Joon Moon, B. Nabet, Naomi E. Leonard, Simon A. Levin, and Ioannis G. Kevrekidis. “Heterogeneous animal group models and their group-level alignment dynamics: An equation-free approach”. In: *Journal of Theoretical Biology* 246.1 (2007), pp. 100–112.

[42] Fumito Mori and Takashi Odagaki. “Synchronization of coupled oscillators on small-world networks”. In: *Physica D Nonlinear Phenomena* 238.14 (2009), pp. 1180–1185.

[43] Ali H Nayfeh. *Introduction to perturbation techniques*. John Wiley & Sons, 2011.

[44] Oleh E. Omel’chenko, Matthias Wolfrum, and Carlo Laing. “Partially Coherent Twisted States in Arrays of Coupled Phase Oscillators”. In: *Chaos: An Interdisciplinary Journal of Nonlinear Science* 24.2 (2014), p. 023102.

[45] Edward Ott and Thomas M Antonsen. “Long time evolution of phase oscillator systems”. In: *Chaos: An interdisciplinary journal of nonlinear science* 19.2 (2009), p. 023117.

[46] Edward Ott and Thomas M. Antonsen. “Low Dimensional Behavior of Large Systems of Globally Coupled Oscillators”. In: *Chaos: An Interdisciplinary Journal of Nonlinear Science* 18.3 (2008), p. 037113.

[47] Mark J. Panaggio and Daniel M. Abrams. “Chimera States: Coexistence of Coherence and Incoherence in Networks of Coupled Oscillators”. In: *Nonlinearity* 28.3 (2015), R67.

[48] Diego Pazó. “Thermodynamic limit of the first-order phase transition in the Kuramoto model”. In: *Physical Review E* 72.4 (2005), p. 046211.

[49] A. Pikovsky, M. Rosenblum, J. Kurths, and Steven H. Strogatz. “Synchronization: A Universal Concept in Nonlinear Sciences”. In: *Physics Today* 56.1 (2003), p. 47.

[50] David J. Pinto and G. Bard Ermentrout. “Spatially Structured Activity in Synaptically Coupled Neuronal Networks: I. Traveling Fronts and Pulses”. In: *SIAM Journal on Applied Mathematics* 62.1 (2001), pp. 206–225.

[51] David J. Pinto, Saundra L. Patrick, Wendy C. Huang, and Barry W. Connors. “Initiation, Propagation, and Termination of Epileptiform Activity in Rodent Neocortex In Vitro Involve Distinct Mechanisms”. In: *Journal of Neuroscience* 25.36 (2005), pp. 8131–8140.

[52] Karthikeyan Rajendran and Ioannis G. Kevrekidis. “Coarse graining the dynamics of heterogeneous oscillators in networks with spectral gaps”. In: *Physical Review E* 84.3 (2011), p. 036708.

[53] Juan G Restrepo, Edward Ott, and Brian R Hunt. “Synchronization in large directed networks of coupled phase oscillators”. In: *Chaos: An Interdisciplinary Journal of Nonlinear Science* 16.1 (2006), p. 015107.

[54] Samuel Rudy, Alessandro Alla, Steven L Brunton, and J. Nathan Kutz. “Data-driven identification of parametric partial differential equations”. In: *SIAM Journal on Applied Dynamical Systems* 18.2 (2019), pp. 643–660.

[55] Jordan Andrew Snyder. “Collective Behavior in Dynamics on Networks”. PhD thesis. University of California, Davis, 2019.

[56] Steven H. Strogatz. “From Kuramoto to Crawford: Exploring the Onset of Synchronization in Populations of Coupled Oscillators”. In: *Physica D: Nonlinear Phenomena* 143.1-4 (2000), pp. 1–20.

[57] Valentina Tozzini. “Coarse-grained models for proteins”. In: *Current Opinion in Structural Biology* 15.2 (2005), pp. 144–150.

[58] Kris Vasudevan, Michael Cavers, and Antony Ware. “Earthquake sequencing: Chimera states with Kuramoto model dynamics on directed graphs”. In: *Nonlinear Processes in Geophysics* 22.5 (2015), pp. 499–512.

[59] Shinya Watanabe and Steven H. Strogatz. “Integrability of a Globally Coupled Oscillator Array”. In: *Physical Review Letters* 70.16 (1993), p. 2391.

[60] Duncan J Watts. *Small worlds: The dynamics of networks between order and randomness*. Princeton University Press Princeton, 2000.

[61] Daniel A. Wiley, Steven H. Strogatz, and Michelle Girvan. “The Size of the Sync Basin”. In: *Chaos: An Interdisciplinary Journal of Nonlinear Science* 16.1 (2006), p. 015103.

[62] Arthur T. Winfree. “Biological Rhythms and the Behavior of Populations of Coupled Oscillators”. In: *Journal of Theoretical Biology* 16.1 (1967), pp. 15–42.

[63] Yuan Xie, Shuangjian Guo, Lan Zhang, Qionglin Dai, and Junzhong Yang. “Twisted States in Nonlocally Coupled Phase Oscillators with Bimodal Frequency Distribution”. In: *Communications in Nonlinear Science and Numerical Simulation* 68 (2019), pp. 139–146.

[64] Dongbin Xiu and George Em Karniadakis. “The Wiener-Askey Polynomial Chaos for Stochastic Differential Equations”. In: *SIAM Journal on Scientific Computing* 24 (2002), pp. 619–644.